

Imaging the Recalescence Behavior of Undercooled Nickel

by

Douglas Marcus Matson

B.S., Chemical Engineering, Cornell University, 1979

B.S., Mechanical Engineering, California State University, Sacramento, 1988

M.S., Material Science and Engineering, University of California, Davis, 1992

Submitted to the Department of
Materials Science and Engineering
in Partial Fulfillment of the Requirements for the Degree of

DOCTOR OF PHILOSOPHY

at the

MASSACHUSETTS INSTITUTE OF TECHNOLOGY

September 1996

© Massachusetts Institute of Technology 1996
All rights reserved

Signature of author _____
Department of Materials Science and Engineering
August 9, 1996

Certified by _____
Merton C. Flemings
Thesis Supervisor, Toyota Professor of Materials Processing

Accepted by _____
Linn Hobbs
John F. Elliot Professor of Materials
Chair, Departmental Committee on Graduate Students

MASSACHUSETTS INSTITUTE
OF TECHNOLOGY

SEP 27 1996

Science

LIBRARIES

Imaging the Recalescence Behavior of Undercooled Nickel

by

Douglas Marcus Matson

Submitted to the Department of Materials Science and Engineering on
August 9, 1996 in Partial Fulfillment of the Requirements for the Degree of
Doctor of Philosophy in Materials Engineering

ABSTRACT

The thermal front accompanying recalescence of undercooled pure nickel melts was characterized using a high speed digital imaging technique. Nucleation was either spontaneous or was stimulated using a physical trigger to induce heterogeneous nucleation at a known site at the desired undercooling. Undercoolings ranged from 30 to 300 °C, with measured velocities between 0.3 and 50 m/sec using a computer data analysis routine to predict the nucleation position and time. Results were compared with those of other workers and with the LKT solidification model assuming a kinetic parameter of 1.0. For levitation processed samples, positive deviation of the propagation velocity with respect to LKT was observed below undercoolings of 80 °C while above a critical undercooling of $\Delta T^* = 170$ °C, the observed propagation velocity showed negative deviation. Glass-encased samples showed no deviation at low undercoolings but the deviation was more pronounced at higher undercoolings than observed using containerless processing. At these high velocities, the front morphology was smooth and a model assuming isotropic spherical expansion provided the best prediction of growth behavior. At low undercoolings, the angular front was observed to result from complex interaction between the shape of the growing prismatic dendritic array and its orientation relative to the surface. Bifurcation of the vertices behind the apex of the pyramid was commonly observed. Similarity in crystallographic orientation between competing arrays within the same sample indicates subsurface connection; the occurrence of multiple nucleation was never observed.

Thesis Supervisor : Professor Merton C. Flemings
Title : Toyota Professor of Materials Processing

Table of Contents

Abstract	2
Table of Contents	3
List of Tables	5
List of Figures	6
Acknowledgments	9
Chapter 1 : Introduction	10
Chapter 2 : Background	13
Sample containment	14
Solidification velocity	15
Melt convection	23
Front morphology	29
Chapter 3 : Experimental Procedures and Data Processing	37
Processing facility	37
Image capture technique	39
Image analysis techniques	41
Radiance profile	42
Velocity calculation	43

Chapter 4 : Glass-encased Processing	51
Data analysis technique	51
Comparison of technique performance	60
Growth theory	63
Chapter 5 : Containerless Processing	73
Image analysis	74
Recalescence velocity measurement	83
Pure nickel samples	83
Solute addition	85
Chapter 6 : Interface Morphology	97
Tip splitting behavior	97
Apex structure	100
Conclusions	110
Suggestions for future work	112
Bibliography	114

List of Tables

		<u>page</u>
<u>Table 2.1</u>	Physical properties for pure nickel and for solute addition	32
<u>Table 3.1</u>	Material certification for nickel stock	48
<u>Table 4.1</u>	Propagation velocity as calculated using different analysis protocols Glass-encased samples processed in argon	65
<u>Table 4.2</u>	Velocity standard deviation for different calculation protocols Glass-encased samples processed in argon	65
<u>Table 4.3</u>	Velocity for helium (4%H ₂) test samples	66
<u>Table 5.1</u>	Velocity for helium (4%H ₂) environment Containerless 5-mm diameter levitated samples	87
<u>Table 5.2</u>	Velocity for helium (4%H ₂) environment Containerless 6-mm diameter levitated samples	87
<u>Table 5.3</u>	Velocity for helium (4%H ₂) environment Containerless 7-mm diameter levitated samples	87
<u>Table 5.4</u>	Velocity for helium (4%H ₂) environment Glass-encased 8-gram samples ^[32]	88
<u>Table 5.5</u>	Velocity for Levitated Ni[1.0% tin] samples	88
<u>Table 5.6</u>	Velocity for Levitated Ni[0.6% carbon] samples	89

List of Figures

	<u>page</u>	
<u>Figure 1.1</u> :	Recalescence during a solidification thermal cycle	12
<u>Figure 1.2</u> :	Levitation facility schematic	12
<u>Figure 2.1</u> :	Schematic representation of the undercooling constituents used to describe growth of a dendrite tip during recalescence [10]	33
<u>Figure 2.2</u> :	Historical results from nickel solidification velocity measurement experiments	34
<u>Figure 2.3</u> :	Nucleation stimulation technique using a physical trigger showing a definition of rise time and solidification velocity	35
<u>Figure 2.4</u> :	Schematic representation of the structure of a dendritic array composed of multiple growing individual dendrites ^[37]	36
<u>Figure 2.5</u> :	Growth morphology during solidification (a) Low undercooling $\Delta T < 170\text{ }^{\circ}\text{C}$ (b) High undercooling $\Delta T > 180\text{ }^{\circ}\text{C}$	36
<u>Figure 3.1</u> :	Schematic of a typical glass-encased sample	49
<u>Figure 3.2</u> :	Pyrometer calibration thermal cycle	49
<u>Figure 3.3</u> :	Iterative technique to define the timing of the nucleation event	50

	<u>page</u>
<u>Figure 4.1 :</u> Mosaic of images obtained for glass-encased nickel processed in argon with $\Delta T=74^\circ$	67
<u>Figure 4.2 :</u> Linear-position and end-point velocity calculation methods	68
<u>Figure 4.3 :</u> Interface identification from video record	68
<u>Figure 4.4 :</u> Apparent velocity as a function of dendrite misalignment with the melt surface	69
<u>Figure 4.5 :</u> Comparison of the results obtained using the linear position and end-point analysis protocols	70
<u>Figure 4.6 :</u> Comparison of the results obtained using the interface tracking and end-point analysis protocols	70
<u>Figure 4.7 :</u> Effect of interface shape assumption for undercoolings below the critical value	71
<u>Figure 4.8 :</u> Comparison of the results obtained using the interface and tip data selection techniques	71
<u>Figure 4.9 :</u> Normalized standard deviation for each protocol	72
<u>Figure 4.10 :</u> Insensitivity to gas environment	72
<u>Figure 5.1 :</u> Spatial relationship between reference frames for levitated droplets	90
<u>Figure 5.2 :</u> Surface velocity during apex contact with the droplet sides at a highly skewed angle from the vertical	90
<u>Figure 5.3 :</u> Analysis of bulk and surface propagation velocities (a) Image sequence for surface motion (b) Droplet cross-section to show how pattern evolved	91
<u>Figure 5.4 :</u> Measured propagation velocity as a function of sample size and undercooling	92
<u>Figure 5.5 :</u> Recirculation flow within droplet interior due to interaction with the levitation field	92
<u>Figure 5.6 :</u> Comparison between glass-encased and containerless processing technique for pure nickel samples	93

	<u>page</u>
<u>Figure 5.7 :</u> Comparison between glass-encased and containerless processing technique for pure nickel samples	93
<u>Figure 5.8 :</u> Effect of solute addition on the predicted dendrite tip radius from LKT theory	94
<u>Figure 5.9 :</u> Effect of solute addition on the predicted propagation velocity from LKT theory	94
<u>Figure 5.10 :</u> Nickel with 1.0 atomic percent tin solute	95
<u>Figure 5.11 :</u> Nickel with 0.6 atomic percent carbon	95
<u>Figure 5.12 :</u> Comparison between video technique results and historical data	96
<u>Figure 6.1 :</u> Interaction between surface discontinuity and array tip	103
<u>Figure 6.2 :</u> Angle between adjacent dendritic array tips	103
<u>Figure 6.3 :</u> Bifurcated vertices in glass-encased sample	104
<u>Figure 6.4 :</u> Onset of tip-splitting behavior for glass-encased sample	105
<u>Figure 6.5 :</u> Onset of isotropic behavior in glass-encased sample	105
<u>Figure 6.6 :</u> Propagation morphology above the critical undercooling	106
<u>Figure 6.7 :</u> Propagation morphology summary	106
<u>Figure 6.8 :</u> Interaction between growing isosceles pyramid and the surface	107
<u>Figure 6.9 :</u> Schematic of the intersection between a pyramidal array and the surface to obtain the observed interaction pattern	107
<u>Figure 6.10 :</u> Apex internal angle as a function of undercooling	108
<u>Figure 6.11 :</u> Bifurcated vertices in containerless processing of pure nickel	108
<u>Figure 6.12 :</u> Bifurcated vertices in nickel [0.6 at% carbon]	109

Acknowledgments

I dedicate this work to my family, Christina, Caitlin, Malia and Ross, who willingly sacrificed many opportunities in support of my decision to attend MIT and pursue the dream of a doctoral degree.

I gratefully acknowledge the contributions of my committee, Professor Ken Russell and Professor Chris Scott for their advise and direction during the critical phase of organizing the significant results into a cohesive whole. I would also like to thank Professor Andreas Mortensen and his research group for allowing me to become a part of their work.

There are many people at MIT who have helped me through out the course of my program, and I would like to recognize the assistance given by members of the solidification group under Professor Merton Flemings : Arvind Sundarrajan, Toshi Koseki, Matthieu Rolland, Hua Shen, Ali Farah and undergraduates Elissa Lee and Rob Chan. A special thanks to John Lum who shared the vision and was instrumental in bringing the concept to realization. I would also like to thank my fellow graduate students, Chris San Marchi, Jeff Nystrom, Harold Ackler and Jim Foresi for the many evenings spent in productive discourse on topics of concern to the future of the American postgraduate education system.

During my work, I became close to Professor Julian Szekely and I remember him with gratitude for his enthusiastic support. I would also like to thank his group members, Bob Hyers, Adam Powell, and Gerardo Trapaga for their close association and many hours of discussion. I would like to thank my colleagues Dieter Herlach, Matthias Barth, Klaus Eckler, Ivan Egry, Bill Hofmeister, Bob Bayuzick, Bill Johnson, David Lee, Mike Robinson and Jan Rogers, who teamed together to make TEMPUS a success.

Finally, I would like to thank my advisor, Professor Merton C. Flemings for the opportunity and freedom to direct the activities of the NASA flight program which provided funding for my work under contract NAG8-971 and NAG8-1230.

Douglas M. Matson
Cambridge, Massachusetts
August 1996

Chapter 1 : Introduction

Undercooling is a process in which molten metal is cooled to below its equilibrium melting point while still in the liquid phase. Soon after a solid phase nucleates, a negative thermal gradient develops due to absorption of a portion of the heat of fusion by the melt. This gradient destabilizes the interface and typically propagation of the front proceeds in a morphology characterized by free dendritic growth of an array of dendrites into the metastable liquid phase. The release of heat from the solid to the liquid is known as recalescence, as shown in Figure 1.1, where growth of the liquid / solid interface is indicated by a difference in radiance between the undercooled liquid and a semi-solid mixture of liquid and solid at or near its melting point; the deeper the undercooling, the higher the fraction solid which forms during recalescence. Following recalescence, equilibrium solidification proceeds at a slower rate dependent upon the heat rejection rate to the droplet environment. During this slower growth phase, much of the original structure is modified due to rapid coarsening of the fine proto-structure which evolved during recalescence.

In an effort to observe solidification behavior immediately following nucleation, a new technique was developed to image local differences in radiation from a sample surface. This difference results primarily from a variation in observed local surface temperature combined with changes in emissivity due to phase transformations; both of these processes are important during recalescence and subsequent semi-solid structural evolution.

The objectives of the current study were to :

- (1) Image the propagation of the thermal front accompanying recalescence,
- (2) Develop an image analysis technique to track interface motion across the surface,
- (3) Evaluate melt convection effects on recalescence phenomenon, and
- (4) Investigate the effects of undercooling on the structure of the recalescence interface.

The approach selected was to optically image the surface of undercooled metallic alloy melts as solidification proceeds under conditions of spontaneous and stimulated nucleation using a high speed digital video system. Figure 1.2 shows a schematic of the major system components in the electromagnetic levitation facility used to process undercooled glass-encased and containerless samples. Image processing techniques were then applied to the series of digital images to calculate the location of specific surface elements and thus track the interface position as solidification progressed across the molten metal surface.

Pure nickel was selected as a baseline material for use in evaluating the analysis technique developed during this work. This choice was based on a lack of agreement on recalescence behavior between many researchers using a broad range of evaluation techniques and a desire to understand the variability inherent in velocity measurement techniques which leads to this disagreement even for a simple pure metal system. The effects of gas environment and dilute solute addition were also evaluated.

The role of melt convection is discussed as a possible explanation for deviation from theory; velocity imaging results are used to anchor model predictions of the physical environment within the melt under different test conditions. The morphology of the dendritic array was subsequently analyzed to understand processes occurring within the recalescence zone as the microstructural evolution proceeds through interdendritic fracture and coarsening. This work has application to understanding the phenomena accompanying recalescence for industrial rapid solidification processing of molten metals.

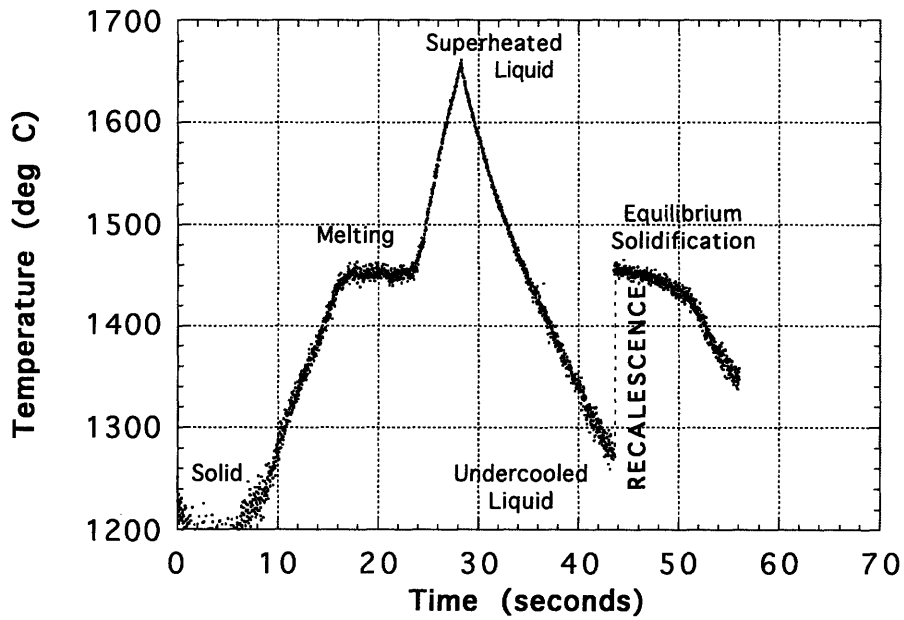


Figure 1.1 : Recalescence during a solidification thermal cycle

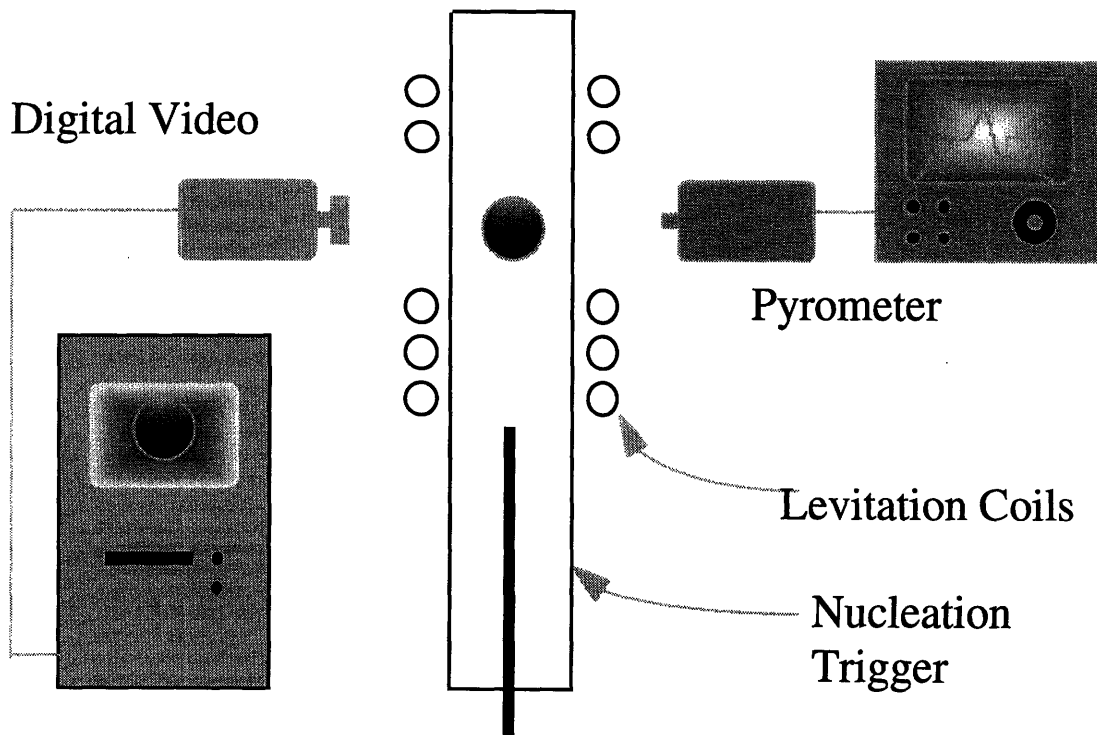


Figure 1.2 : Levitation facility schematic

Chapter 2 : Background

Research on the solidification of metals and alloys from undercooled melts has historically employed one of two basic sample containment approaches. In the first, a container is used to hold the molten alloy during melting and subsequent recalescence. Bulk samples can be viewed from above and the propagation of the thermal front accompanying recalescence may be investigated using a variety of pyrometric and optical sensing techniques. A sub-set of this approach involves using an optically clear container to allow sensor access to the entirety of the sample surface; this method is known as glass encapsulation.^[1]

The second approach involves utilizing containerless processing techniques to investigate recalescence phenomena and morphological evolution with sensor access across the exposed free surface of the sample. Examples of this type of approach are drop-towers/tubes, aerodynamic levitation apparatus, electrostatic levitators, and electrodynamic levitation facilities.^[2]

This chapter discusses the relative merits of the two approaches and then provides a summary of the modeling of growth during solidification and a description of the methods historically used to measure the propagation velocity during recalescence. Since the fluid flow regimes under which solidification progresses are vastly different using each of these techniques - natural convection dominates in encapsulated samples and forced convection dominates in levitated samples - a brief description of fluid flow modeling is then presented. Finally, the morphology of the front is discussed in terms of how the front appears macroscopically and what processes are occurring both within the recalescence zone and in the adjacent region as the proto-structure undergoes rapid microstructural evolution.

Sample containment

Levitation of the sample using electrodynamic Lorenz forces involves overcoming the sample weight through the interaction of the induced magnetic field with the externally applied field. The sample is inductively melted and the temperature is controlled by varying the sample environment - typically using flowing gas. Fully glass encapsulated samples may be levitation processed, but frequently an open-ended container is used to support and position the specimen within the field - here after referred to as a glass-encased sample.

Glass-encased samples can also be processed using induction heating and the relative advantages in selecting between these two sample configurations relates mainly to the sensitivity of the material to be processed to the presence of container wall materials. The presence of the wall modifies fluid flow and may provide numerous heterogeneous nucleation sites. Contamination of the melt is also a potential problem through leaching of wall materials, such as dissolution of free silicon or boron from the glass, or reactions between the container and melt constituents, for example chromium from molten steel. Advantages for using an encapsulation technique include selecting the wall material such that the container provides an active flux to remove oxides from the melt^[3] and having the ability to turn off the induction field to initiate cooling, thus reducing melt convection through viscous damping.

Without the presence of a container, the weight of the sample must be overcome by interaction between the applied field and the resultant internal fields. Cooling of the sample is accomplished by introducing gas flow across the free surface of the melt. The interaction of the sample with both the induction field and the gas drives internal fluid flow and forced convection produces turbulent conditions within the melt.^[4] Under equilibrium conditions, the free surface assumes a tear drop shape^[5] but surface oscillations commonly deform the droplet significantly. Thus, levitated samples are not prone to melt/wall interaction but may suffer from increased melt turbulence.

Solidification velocity

Modeling of the growth during recalescence has concentrated on processes occurring at or near the tip during solidification. An isolated isothermal and isoconcentrate dendrite with a constant tip radius, R , and tip temperature, T_t , is assumed to grow with a tip velocity, V , into undercooled liquid of constant temperature, T_∞ . As growth occurs, the shape of the tip is assumed to grow in the form of a paraboloid of revolution with heat (and mass) transport controlled by diffusion - thus neglecting convection near the tip.

Based on a definition of the thermal and solutal Péclet numbers as :

$$P_t = \frac{VR}{2\alpha} \quad (2.1)$$

$$P_c = \frac{VR}{2D} \quad (2.2)$$

for α and D the thermal diffusivity and the solute interdiffusion coefficient, respectively, Ivantsov^[6] proposed a solution to the heat transfer from a parabolic dendrite tip assuming equilibrium interface kinetics and anisotropic surface energy :

$$\Delta T_t = T_t - T_\infty = (\Delta H/C_p) Iv(P_t) \quad (2.3)$$

$$Iv(P) = P * \exp(P) * E_1(P) \quad (2.4)$$

$$E_1(P) = \int_P^\infty \frac{\exp(-z)}{z} dz \quad (2.5)$$

ΔH is the latent heat of fusion, C_p is the specific heat, and $E_1(P)$ is the exponential integral function, with P either the thermal or solutal Péclet number.

This treatment is extended to include contributions to undercooling from curvature of the dendrite tip, using the Gibbs-Thompson relationship for depression of the melting point, T_m :

$$\Delta T_r = \frac{2 \gamma}{R \Delta S} \quad (2.6)$$

where γ is the solid-liquid interfacial energy and ΔS is the entropy of fusion.

Deviation from local chemical equilibrium will occur during rapid solidification due to propagation of the front at the tip velocity. Aziz^[7] described the velocity dependent partitioning coefficient, k_V , as :

$$k_V = \frac{(k_E + \beta)}{(1 + \beta)} \quad (2.7)$$

$$\beta = a_0 V / D_i = V / V_d \quad (2.8)$$

for k_E the equilibrium partitioning ratio, a_0 the interatomic jump distance, D_i interface diffusivity, and V_d the atomic diffusive speed. The interface diffusivity is estimated using the Einstein-Stokes relation^[3] :

$$D_i = \frac{k_B T_\infty}{(6 \Pi \eta a_0)} \quad (2.9)$$

where k_B is the Boltzmann constant, and η is the viscosity of the undercooled liquid.

Boettinger *et al*^[8] combined the velocity dependence of the partition coefficient, the slope of the liquidus, m_L , and the interface undercooling on velocity to obtain an expression for constitutional undercooling, ΔT_c :

$$\Delta T_c = m_L C_0 \left[\frac{m^*/m_L}{\{1 - (1 - k_V) I_V(P_c)\}} - 1 \right] \quad (2.10)$$

for C_0 the initial composition of the alloy and

$$m^*/m_L = 1 + \left[\frac{k_E - k_V (1 - \ln[k_V/k_E])}{(1 - k_E)} \right] \quad (2.11)$$

Typically a kinetic term is also included in the definition of the total undercooling at the tip and it is used to represent the deviation from the ideal behavior assumed for solution of the tip heat and mass transfer equations. Turnbull^[9] suggested an equation based on a recognition that attachment kinetics may be controlled by atomic impingement at the interface instead of diffusive interactions and thus the speed of sound, V_s , is a more appropriate measure of collision-limited growth :

$$\Delta T_k = V / \mu = (k_B T_m T / \Delta H) \ln \left[\frac{(V - V_s)}{V} \right] \quad (2.12)$$

where μ is the linear interface kinetic coefficient. The series expansion of the logarithmic term may be truncated after the first term at low undercoolings yielding a simplified expression for the kinetic coefficient :

$$\mu = \Delta H V_s / (k_B T_m^2) \quad (2.13)$$

In summary, the total undercooling is taken as the sum of the thermal undercooling, undercooling due to curvature, undercooling due to solute diffusion, and kinetic undercooling :

$$\Delta T = \Delta T_t + \Delta T_r + \Delta T_c + \Delta T_k \quad (2.14)$$

A schematic of the various components which make up the tip undercooling is shown in Figure 2.1^[10] for both a pure material and an alloy. The treatment presented above yields solutions which depend on the product of the tip radius and velocity and a second relationship is required to obtain a unique solution. By assuming equal thermophysical properties for liquid and solid phases, the Mullins-Sekerka analysis^[11] could be extended to high Péclet numbers and an independent set of equations obtained. Morphological stability theory^[12] is used to specify the tip radius as the shortest wavelength which can form under conditions which describe the local tip environment. Crystalline anisotropy is also neglected. This treatment^[13] was developed by Lipton, Kurz and Trivedi and is hereafter known as LKT theory :

$$R = \frac{\gamma / \Delta S \sigma^*}{\left[P_t \frac{\Delta H}{C_p} \right] (1 - n) + 2 m_L P_c C_o \frac{(k - 1) (1 + g)}{[1 - (1 - k) I_v(P_c)]}} \quad (2.15)$$

The parameters n and g are defined as :

$$n = \frac{1}{\sqrt{\left\{ 1 + \frac{1}{\sigma^* P_t^2} \right\}}} \quad (2.16)$$

$$g = \frac{2 k}{\left(1 - 2 k - \sqrt{\left\{ 1 + \frac{1}{\sigma^* P_c^2} \right\}} \right)} \quad (2.17)$$

For small Péclet numbers, this treatment reduces to the Lipton, Glicksman, and Kurz (LGK) model^[14] since n and g each approach zero. The Boettinger, Coriell and Trivedi (BCT) model^[15] is obtained when n is neglected, but g is important.

In all cases, the stability constant is model dependent and, for the parabolic dendrite tip presented here, it is taken to be^[16] :

$$\sigma^* = \frac{2 d_0 \alpha}{R^2 V} = \frac{1}{4 \Pi^2} \quad (2.18)$$

$$d_0 = \frac{\sigma T_m C_p}{\Delta H^2} \quad (2.19)$$

for d_0 the capillary length. Typical values for the thermophysical properties of nickel are shown in Table 2.1.^[17-20]

Iterative numerical solution of this set of equations is complex, but as pointed out by Eckler *et al.*^[21], a graphical solution is readily obtained by assuming a value for the velocity and iteratively solving for the radius, the Péclet numbers, and the component undercooling values to obtain a total undercooling. These values then may be individually investigated to obtain closure about the parameter of interest. An empirical fit of experimentally obtained solidification velocity data may be accomplished by assuming that μ is an adjustable parameter representing deviation induced by local non-equilibrium.

Measurements performed by Walker^[22] using widely separated photodiodes on the surface of 150 - 400 gram columnar samples of undercooled nickel showed the velocity correlated linearly with the square of the undercooling at low values and he identified a regime at a critical undercooling of about 170 degrees above which the correlation changes. This critical undercooling, ΔT^* , was also associated with a shift from a columnar grain structure to a refined, equiaxed microstructure.^[23] A mechanical disturbance was identified by measuring the amplitude of an audible signal, with a maximum intensity centered at this critical undercooling, and Walker theorized that this effect was due to a rapid volume change during freezing.

Figure 2.2 shows a selection of the published measurements of the propagation velocity of pure nickel solidifying into an undercooled melt. The general historical trend has followed the original numbers obtained by Walker; below ΔT^* the data can be fit to LKT theory using a kinetic parameter of $\mu = 1.0$, while above the critical undercooling much data scatter is observed.

Early velocity measurement techniques rely on sensing the passage of the thermal front across an assumed path along the surface of the melt. As seen in Figure 2.3, when the front enters the field of view of the sensing element, a rise in intensity is observed; when the front leaves, the signal becomes flat, indicating that no local changes in temperature or emissivity are occurring within the field of view. The velocity is obtained by dividing the rise time by the sensor target diameter. This technique was used by Walker^[22] using photodiodes and Piccone *et al.*^[24] using the target from a two-color pyrometer. Schleip *et al.*^[25] measured the velocity using a series of two photodiodes aligned vertically along the surface; the geometry of the interface and detector were controlled by physically stimulating nucleation at the base of the electromagnetically levitated specimen using an Al_2O_3 trigger. In order to assure that triggering was accomplished on the base of the sample, a flat disk could be used to stimulate nucleation.

Bassler *et al.*^[26] developed a linear array of 38 photodiodes with a recording time resolution capability of 10 nanoseconds. By pre-selecting an intensity level above which the element will be triggered, the passage of the front may be tracked across the surface as recalescence proceeds. A computer is then used to interpret the data based on assumptions on the position of the nucleation site in space and time. Multiple nucleation events were theorized to account for non-sequential element triggering and a limit was identified, above which the propagation velocity was constant at 20 m/sec. The authors suggest that above an undercooling of 173 K, the velocity could be limited by attachment kinetics. Without a secondary confirmation on the activity of multiple nucleation sites or on interface shape,

assumptions on the relationship between the sensing array and the growing front are required.

Nucleation triggering is an important requirement for accurate velocity measurement in that the geometrical relationship between the sample and the sensor are defined, and the point from which growth progresses is known. This effect is shown in Figure 2.3, where recalescence in a levitated sample is initiated using a stimulation needle. At the point of contact, growth proceeds as a series of increasing diameter spheres with the radial rate of growth, V_{abs} , assumed constant based on a simple model which assumes isotropic growth from a single nucleation site. Note that for a planar front intersecting a flat surface, the apparent surface velocity, V_{app} , increases as a function of the cosine of the angle, α , between the surface and the interface normal (propagation direction) :

$$V_{app} = V_{abs} / \cos(\alpha) \quad (2.20)$$

Hence, at the end of the recalescence event near the top of the droplet, and thus at higher intersection angles, the apparent velocity increases asymptotically to an infinite rate. It is therefore imperative that the relationship between the sensor and the nucleation site is known such that the absolute bulk velocity may be defined from the measured apparent surface velocity.

In the most accurate technique to date, Eckler *et al.*^[27] proposed utilizing a dual sensor technique to set the timing of both the start and end of the nucleation event. A sensor measures the change in capacitance of the trigger during contact with the molten sample and assures that the timing of the initiation of solidification is known. The timing of the end of recalescence is simultaneously measured using a vertically mounted pyrometer with the target directed axially down onto the top of the levitated sample. By assuming a droplet shape and propagation path, the travel distance is obtained and an average bulk velocity calculated.

Since the shape of a levitated droplet is known to be highly variable due to rapid surface oscillations, a recognized need to address the extent of the deformation of the surface during recalescence has led to development of several high speed imaging techniques. In pioneering work at Vanderbilt University, a video recording technique was employed by Bassler *et al.*[28] to investigate the propagation of titanium-aluminum alloys at rates of up to 12,000 frames per second. The digitized 64 by 64 pixel image could be used to track the solidification of primary phase from the melt and collect images of the solid-state transformation from beta to alpha. In an effort to combine both high spatial and temporal resolution, Hofmeister developed a 10 by 10 pixel digital photodiode array capable of capturing up to 8192 images at an acquisition rate of up to 1 million frames per second.[29] Spatial resolution is obtained by expanding the image in a complex image manipulation technique which relies on comparing the intensity of adjacent pixels to obtain an average intermediate value. The expanded information is not used in velocity calculations but is used to provide a guideline on the morphology of the interface given an assumption that the interface is always convex.

Due to the limitations imposed by data storage requirements, a trade-off currently exists between temporal resolution, event duration recording capability (total number of frames saved), and spatial resolution. In order to observe non-steady state behavior and understand the underlying sources of variability in phenomena occurring during recalescence, an imaging technique is indicated. Tracking the motion of surface elements under conditions of translation, oscillation, and rotation in relation to a nucleation event which is uniquely located in space and time may be accomplished only in this manner based on a detailed knowledge of the relationship between the recording element and the sample through analysis of a long chronological series of sequential images. With the appropriate selection of the spatial resolution, sample shape at the time of recalescence may be accurately defined and the existence of simultaneous multiple nucleation events may be confirmed or disproved. Using a video technique also provides the possibility of tracking

microstructural evolution with time in the event that multiple phases form either during or immediately following primary recalescence.^[30] The effects of non-isotropic behavior and complex interface morphology can also be investigated.

Melt convection

When using a glass-encapsulation technique the power may be deactivated to allow cooling and thus natural convection dominates the evolution of steady-state flow regimes. Ignoring solutal and Marangoni surface tension driven components, the general statement for natural convection is^[31] based on the differential equations expressing continuity, momentum transfer and energy transfer :

$$\nabla \cdot \mathbf{u} = 0 \quad (2.21)$$

$$\rho \frac{D\mathbf{u}}{Dt} + \rho \mathbf{g} \beta (T - T_\infty) = -\nabla p + \mu \nabla^2 \mathbf{u} \quad (2.22)$$

$$\frac{DT}{Dt} = \alpha \nabla^2 T \quad (2.23)$$

where the vector quantities \mathbf{u} and \mathbf{g} are the velocity and acceleration due to gravity, respectively, and t is time, β the expansion coefficient, μ the viscosity, and α the thermal diffusivity. The substantial time derivative is defined as :

$$\frac{D(\)}{Dt} = \frac{\partial(\)}{\partial t} + V_x \frac{\partial(\)}{\partial x} + V_y \frac{\partial(\)}{\partial y} + V_z \frac{\partial(\)}{\partial z} \quad (2.24)$$

Solution of these equations must be performed numerically as the temperature and velocity fields are mutually coupled but a simple two dimensional solution for flow past a vertical plate is based on utilizing the dimensionless Prandtl, and Grashof numbers; the Reynolds number can then be investigated to determine the flow regime :

$$\text{Pr} = \frac{C_p \mu}{k} \quad (2.25)$$

$$\text{Gr} = \frac{g x^3 \beta (T_w - T_\infty)}{\nu} \quad (2.26)$$

$$\text{Re} = \frac{U L}{\nu} \quad (2.27)$$

for U the velocity, L the characteristic length, $\nu = \mu / \rho$ the kinematic viscosity, C_p the specific heat, k the thermal conductivity, x the vertical distance along the wall, T_w the wall temperature and, T_∞ the bulk fluid temperature. For induction melting of typical glass encased samples^[32] graphical analysis of the maximum velocity depends on bounding the solution for reasonable driving forces over the sample dimensions. This is accomplished by setting the limits on the Grashof number and then evaluating both the maximum velocity obtained and the anticipated shape of the velocity profile. Due to drag along the fixed wall, the velocity linearly increases to a maximum and then decreases toward the droplet center. Since the calculated^[31] maximum velocity is negligible, for this sample geometry we can assume stagnant conditions throughout the melt.

Within the recalescence zone, density driven flow may still be present as the change in atomic volume during fusion is on the order of 6% for nickel. This phenomenon has been modelled by McFadden and Coriell^[33] and the effect is small.

For levitated samples, forced convection dominates and thermal and velocity fields are no longer coupled. In practice, oscillatory fluid motion exists due to surface vibrations induced by transitory flows and due to sample rotation and translation induced by asymmetry in the field coupling. These effects are caused by gross sample motion away from the equilibrium position and modeling of steady state processes must concentrate on time averaged behavior. This treatment ignores the Marangoni surface tension driven flow which dominates in microgravity, and density driven flows due to shrinkage on solidification.

Zong *et al.*^[34, 35] developed a method to evaluate melt convection in levitated molten metallic samples. By measuring the source current, coil dimensions, droplet shape and equilibrium sample position in the field, a matrix solution is obtained for the induced electromagnetic forces on individual volume elements within the liquid.

$$F = \int (1/2) \operatorname{Re}\{J \times B^*\} dV \quad (2.28)$$

with the notation describing the evaluation of the real part of the cross product between the current vector, J , and the complex conjugate of the magnetic flux density, B^* . The integrated force is equated to the sample weight to obtain the induced current and force vector for all fluid elements from knowledge of the applied field using the method of neutral inductances. The force vector obtained is thus a function of sample and coil geometry, only. The field is strongest on the surface and does not penetrate the droplet interior due to the shielding provided by surface elements. This skin depth results from the induced currents which create a magnetic field concentrated near the surface to oppose the applied field. The skin depth, δ , is defined as :

$$\delta = \sqrt{\frac{2}{\mu_0 \sigma_{el} \omega}} \quad (2.29)$$

for μ_0 the magnetic permeability, σ_{el} the electrical conductivity and ω the excitation frequency. Thus, an exponential grid is generated to allow calculation of the current flow in the discrete annular elemental circuits.^[4] The results of the electromagnetic force model calculations can then be applied to the Navier-Stokes equation (Equation 2.22) to solve for internal fluid flow. The effective viscosity, μ_{eff} , is used in this treatment to account for the effects of turbulent flow induced momentum transfer. For this work, the K- ϵ model for estimating the turbulent viscosity was used.

$$\mu_{\text{eff}} = \mu + \mu_t \quad (2.30)$$

$$\mu_t = \frac{C_\mu \rho K^2}{\epsilon} \quad (2.31)$$

for μ the viscosity, μ_t the turbulent component to viscosity, C_μ an empirical material constant, K the turbulent kinetic energy, and ϵ the energy dissipation rate. A computational fluid dynamics package, FIDAP, property of Fluid Dynamics International Inc., was used to iteratively solve for the steady state solution to the differential equation. FIDAP uses a nondimensionalized approach using linear algebraic equations to converge on a solution which satisfies the continuity equation for cylindrical symmetry :

$$\frac{1}{r} \frac{d[\rho r u_r]}{dr} + \frac{d[\rho u_z]}{dz} = 0 \quad (2.32)$$

The non-dimensional form of the Navier-Stokes equation is :

$$du^*/dt^* + u^* \nabla^* u^* = -\nabla P + 1/N_{\text{Re}} \nabla^{2*} u^* + 1/N_{\text{Fr}} + (1/\rho u^2) F \quad (2.33)$$

where N_{Fr} is the Froude number and, in this case, the Reynolds number, (Equation 2.27) is modified to include the contribution from turbulent flow to momentum transfer by utilizing the effective viscosity,

$$N_{\text{Re}} = \frac{\rho R u}{\mu_{\text{eff}}} \quad (2.34)$$

$$N_{\text{Fr}} = \frac{u^2}{g R} \quad (2.35)$$

for u a reference velocity and u^* the dimensionless velocity.

Boundary conditions are :

- (1) symmetry along the centerline,
- (2) zero shear and zero normal velocities along the free surfaces,
- (3) zero kinetic energy of the surface,
- (4) zero flux of kinetic energy dissipation except at the poles where the dissipation is set to zero.

The model predictions were anchored by iteratively solving for the external droplet shape given position within the coils with known geometry. By comparing the free surface shape obtained by fluid modeling to that experimentally observed, Schwartz^[5] demonstrated the validity of this approach. Two counter-current recirculation loops were predicted to form with the maximum flow directed axially upward along the center of the sample. The predicted maximum velocity was along the outer surface of the droplet and of a magnitude of about 0.3 m/sec under nominal operating conditions. Experimental verification of the absolute values for local flow are difficult and the results are best used to compare the relative magnitude of the recirculation pattern because of non-equilibrium experimental conditions such as melt surface oscillations or gross droplet motion, power supply fluctuation and gas flow along the free surface of the sample.

The effects of forced convection on dendritic growth during recalescence was evaluated by Ananth and Gill.^[36, 37] Using a moving boundary approach with an imposed fluid flow, U_{∞} , and assuming the flow field is described by Oseen's viscous flow approximation at low Reynolds numbers ($N_{Re} < 1.0$) :

$$Nu = P / St = \left[\int_1^{\infty} \exp \left\{ - \int_1^y f(z) dz \right\} dy \right]^{-1} \quad (2.36)$$

$$f(z) = P_e z \left[1 + \frac{P}{P_e} + \frac{1}{P_e z^2} - \frac{E_1(\text{Re } z^2 / 2)}{E_1(\text{Re} / 2)} - \frac{2}{z^2 \text{Re}} \frac{e^{-\text{Re}/2} - e^{-\text{Re } z^2 / 2}}{E_1(\text{Re} / 2)} \right] \quad (2.37)$$

The Nusselt number is $Nu = h R / k$ for h the local heat transfer coefficient, the Stefan number is $St = \Delta T / (\Delta H / C_p)$ and $P = V R / \alpha$ is the Péclet number for the crystal. For $P_e = U_\infty R / \alpha$ defined as the Péclet number for the fluid, E_1 the first exponential integral function (Equation 2.5), and the tip Reynolds number, $Re = (U_\infty + V)R / \nu$.

Experiments on imaging the growth of ice crystals by Koo *et al.*^[38] and succinonitrile by Glicksman *et al.*^[39] have shown the predictive validity of the model. In a series of elegant microgravity experiments, Glicksman demonstrated the ability to determine the numerical value of the stability constant, σ^* , in the microgravity environment aboard the space shuttle, where gravity driven flow is precluded. Clear metallic-analog systems are readily imaged to allow measurement of R and V simultaneously.

Unfortunately this is not possible for molten metallic alloy systems, but measurements on nickel and nickel-carbon by Eckler *et al.*^[40] show a positive deviation in the observed propagation velocity at low undercoolings due to melt convection for levitated samples. The physical interpretation for this effect is that an increase in convection near the tip results in a steepening of the thermal gradient as the boundary layer is affected by turbulent eddies which provides an alternate mechanism for removal of the heat of fusion at the tip. An alternate form of Equation 2.15 is :

$$R^2 = \frac{\Gamma / \sigma^2}{m G_c - G_t} \quad (2.38)$$

for Γ the Gibbs-Thompson coefficient, and G_c and G_t the solutal and thermal gradient. Thus with an increase in the thermal gradient, which is negative ahead of the tip, the tip radius will sharpen and from the morphological marginal stability criteria (equation 2.18) the velocity must thus increase.

Front morphology

The shape of the growing interface has been successfully imaged using high speed photographic techniques. This technique relies on the contrast obtained between the darker undercooled liquid and the brighter hot semi-solid which results after recalescence. Subsequent equilibrium solidification to a fully solid sample can not be imaged using this technique as the difference in radiance between the phases is low. Imaging is thus based on both the temperature of the phases which are present and on the emissivity of the component phases.^[28, 30] During recalescence, the solidification front appears sharp; assuming a perfectly flat step interface moving into an undercooled liquid, an estimate of the width of the thermal boundary layer is obtained by comparing the ratio of the thermal diffusivity to the propagation velocity.^[28] Using values for nickel taken from Table 2.1 this returns a thermal interface or boundary layer width of 10, 1.2, and 0.3 microns at velocities of 1, 8 and 40 m/sec. Objects on this scale are not resolvable using current high speed imaging technology.

Colligan and Bayles^[41] obtained photographic images of nickel solidification using film speeds of up to 7,500 frames per second; the interface morphology at low undercoolings appeared angular and dendritic while at higher undercoolings it appeared spherical and continuous. Wu *et al.*^[42] utilized high-speed photography to image the solidification of undercooled nickel-tin alloys encased in silica flux. Propagation velocities were measured at low undercoolings by discerning the position of the recalescence interface as an increase in radiance between undercooled liquid and high temperature solid. The velocity obtained by tracing the position of the interface with time could be compared to that calculated from the rise-time of the optical pyrometer. The interface shape was angular at low undercoolings and both concave and convex regions could be identified even when solidification was observed to initiate from a single point. Comparison of the length scale of the angular sections of the front showed that features were several orders of magnitude

greater than predicted by LKT theory^[13]; the theoretical tip radius is predicted to be on the order of 0.8 microns but the features in the pictures were of millimeter scale. Figure 2.4 shows how an array of dendrites could grow to form the observed angular macroscopic interface shape. Due to the limitations imposed by the camera frame rate, the velocity analyses were restricted to low undercoolings.

High speed digital video imaging has been used to resolve surface velocities in excess of 50 m/sec.^[32] A typical video image is presented in Figure 2.5 showing the angular morphology at low undercooling and the spherical morphology at high undercooling as identified by Colligan and Bayles.^[41] These images were taken at 40500 frames per second by a Kodak Ektapro HS Motion Analyzer Model 4540 video system at MIT on levitated nickel samples which were triggered on the bottom surface using a nickel wire needle.

Multiple nucleation is not apparent in these images. Lum^[32] showed that in instances where nickel-tin dendrites appeared simultaneously on the video record, the individual dendritic arrays appeared aligned and the common orientation indicated that subsurface connection must exist. Presumed multiple nucleation events could be explained as an angular front intersecting the exposed surface of the glass container at a high incident angle. Restrictions on the resolution capability of existing video equipment could not rule out nucleation ahead of the front on a scale smaller than the current 200 micron pixel size.

The preceding discussion highlights the need to develop new methods to evaluate the processes occurring within the recalescence zone in order to understand deviation from current dendrite growth theory. Velocity measurement involves accurately defining the position of the interface as the front propagates across the surface and tracking the movement of specific surface elements to remove the effects of rotation and translation. To combine micron-level spatial resolution with temporal resolution on the order of microseconds, a high speed video technique is indicated. To understand the behavior within the semisolid region during recalescence, a spot size on the order of several millimeters used in current pyrometry-based systems is inadequate.

Table 2.1 : Physical properties for pure nickel and for solute addition

Symbol	Property	Value	Units	Reference
ΔH	latent heat of fusion	17150	J / mol	[17]
C_p	heat capacity	38.48	J / mol K	[17]
μ	viscosity	5.0	kg / m ² s	[17]
α	thermal diffusivity	10×10^{-5}	m ² / s	[18]
ρ	density of liquid	7900	kg / m ³	[17]
γ	surface tension	1778	mN / m ²	[17]
U_s	velocity of sound	4036	m / sec	[17]
β	thermal expansion coefficient	1.51×10^{-4}	K ⁻¹	[17]
Ω	atomic volume	7.43×10^6	m ³ / gatom	[17]
D_{Sn}	diffusivity of tin	5×10^{-5}	m ² / sec	[19]
D_C	diffusivity of carbon	5×10^{-5}	m ² / sec	[20]

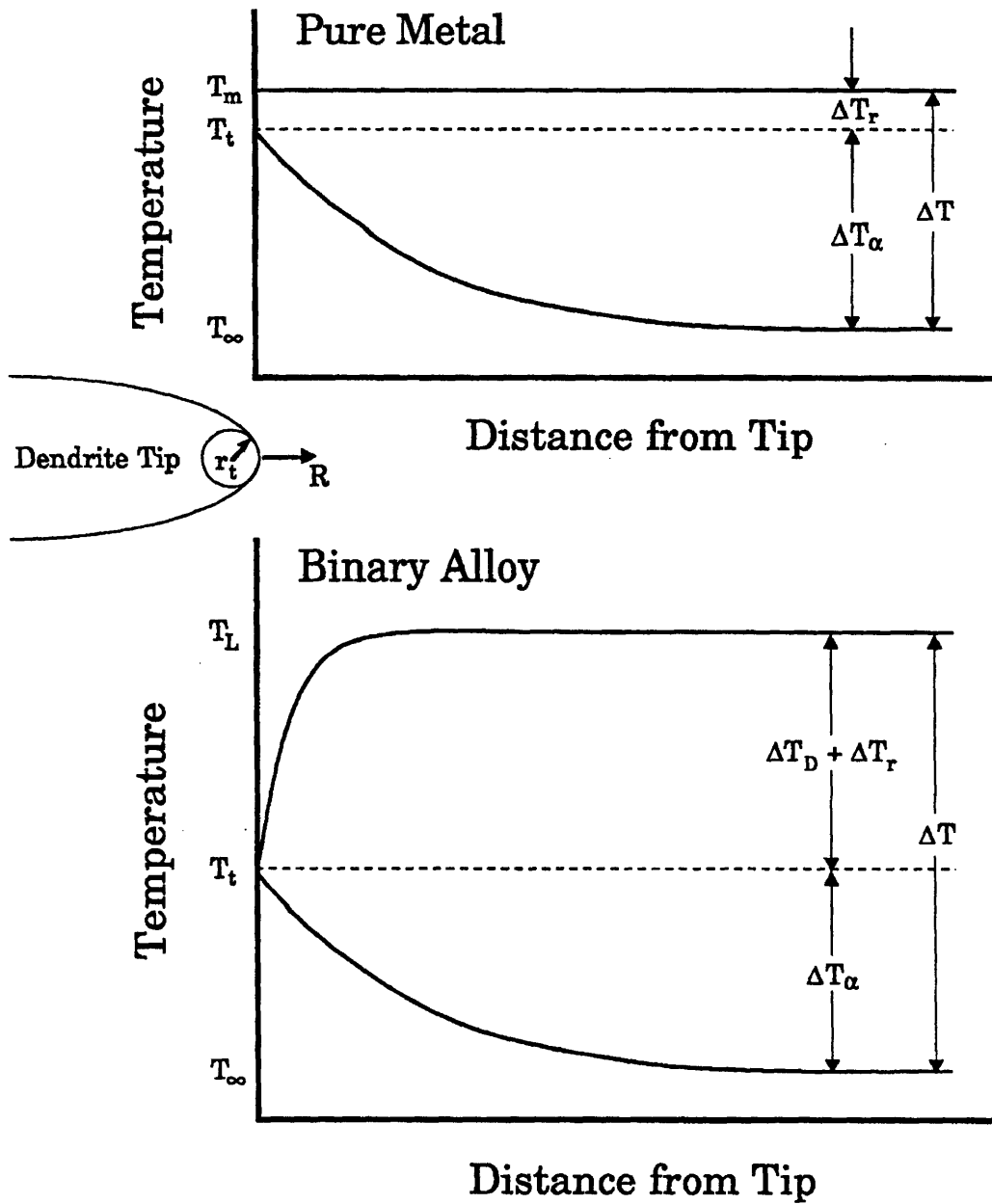


Figure 2.1 : Schematic representation of the undercooling constituents used to describe growth of a dendrite tip during recalescence ^[10]

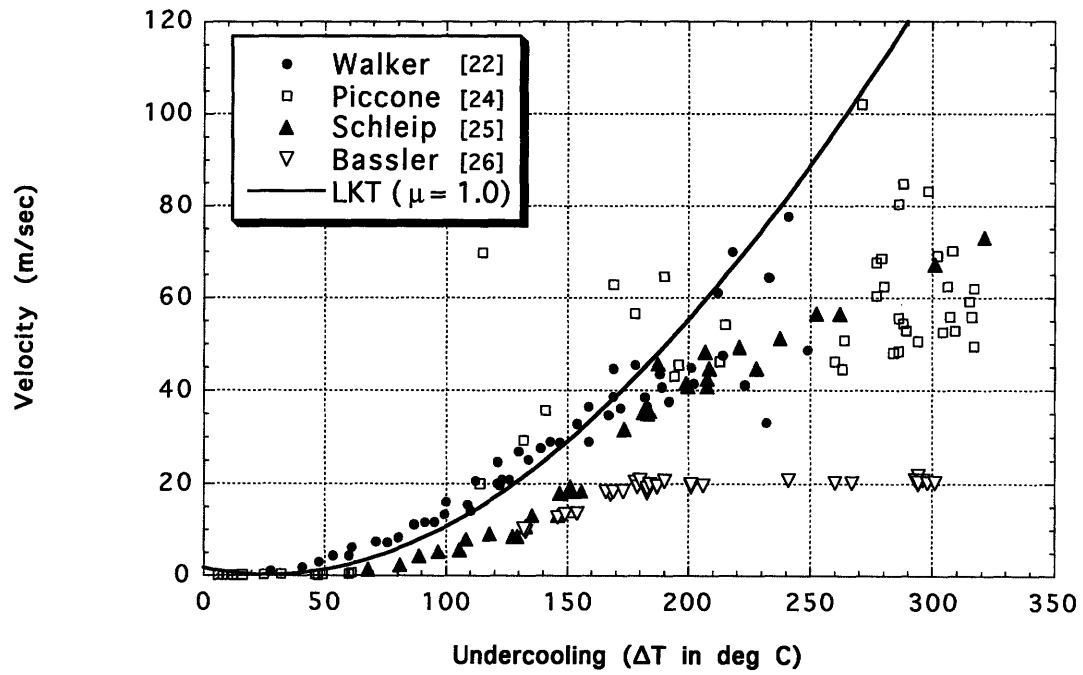


Figure 2.2 : Historical results from nickel solidification velocity measurement experiments

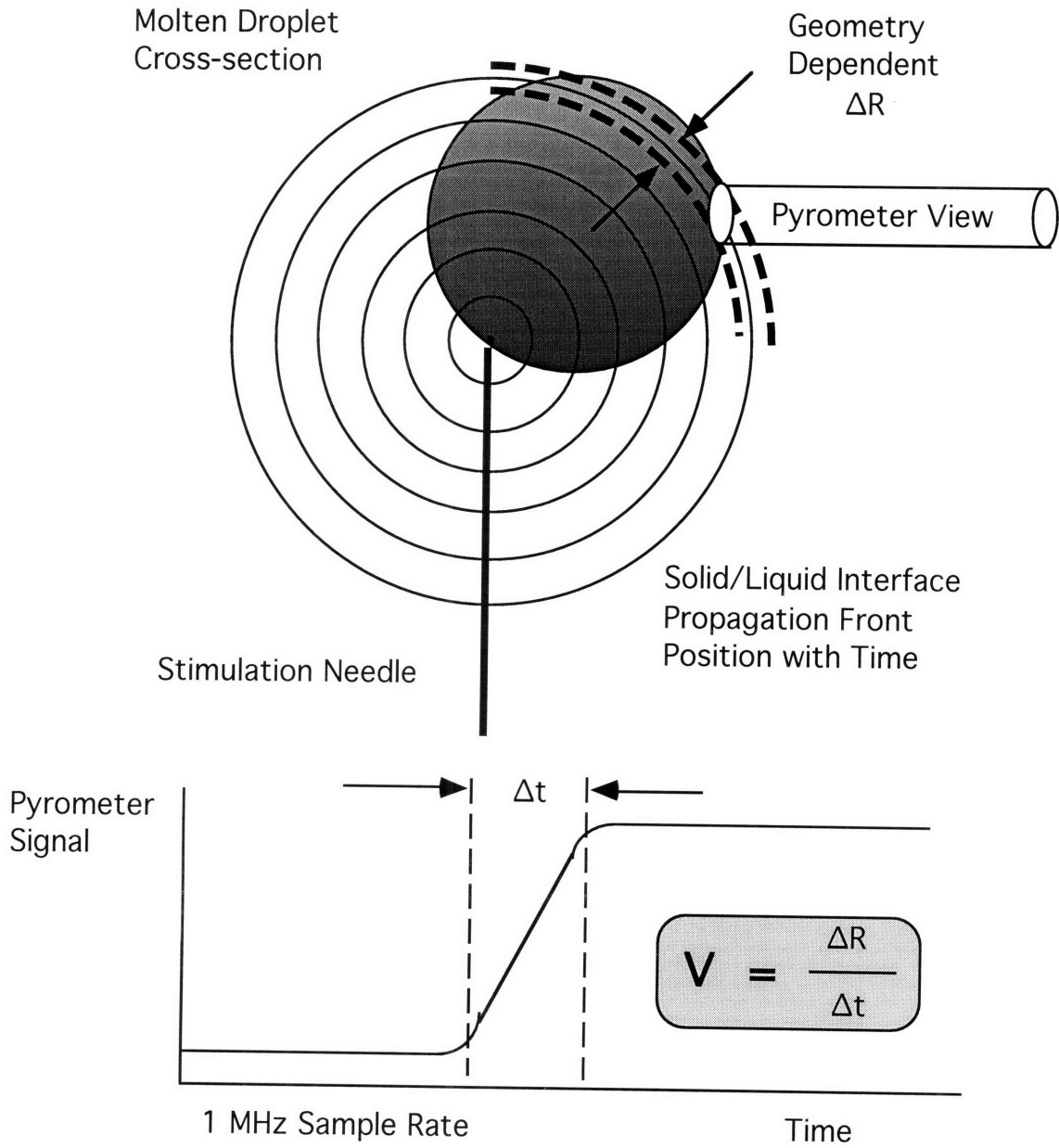


Figure 2.3 : Nucleation stimulation technique using a physical trigger showing a definition of rise time and solidification velocity

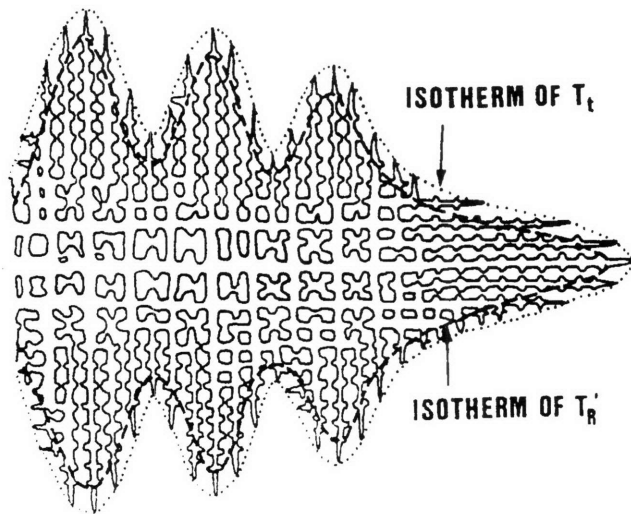
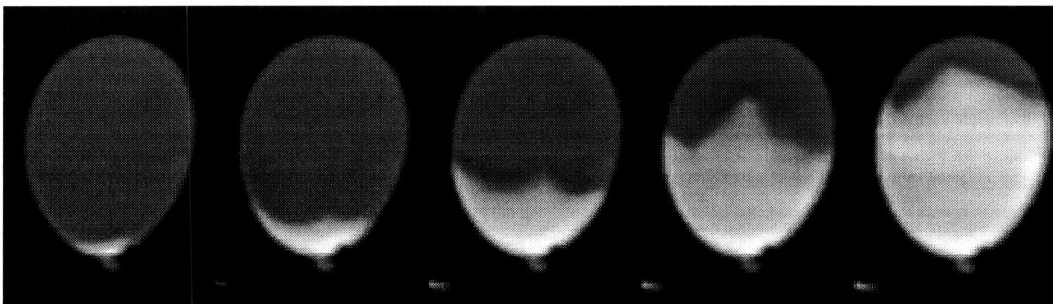
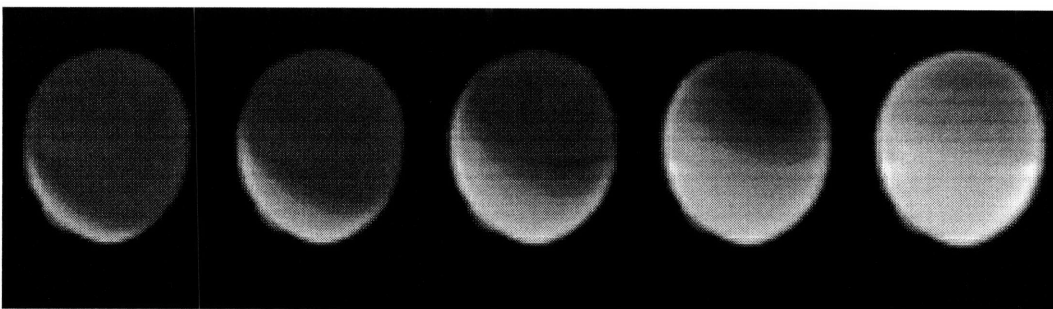


Figure 2.4 : Schematic representation of the structure of a dendritic array composed of multiple growing individual dendrites^[19]



(a) $\Delta T = 124^\circ$

125 $\mu\text{sec/frame}$



(b) $\Delta T = 194^\circ$

25 $\mu\text{sec/frame}$

Figure 2.5 : Growth morphology during solidification

- | | | |
|-----|-------------------|--------------------------------|
| (a) | Low undercooling | $\Delta T < 170^\circ\text{C}$ |
| (b) | High undercooling | $\Delta T > 180^\circ\text{C}$ |

Chapter 3 : Experimental Procedures and Data Processing

Processing facility

Glass-encased samples, as seen in Figure 3.1^[32], were fabricated by placing sample material inside an open-ended quartz tube of either rectangular or circular cross-section. This tube is mounted inside a second closed-end tube which is evacuated and refilled with argon to exclude air. The sample is in intimate contact both with the inner tube surface and the glass frit used as a base support medium. This glass softens as the metal melts and any oxide contaminants are fluxed from the surface.^[19]

Raw material was purchased from Electronic Space Products International to fabricate the glass encased samples. 5N pure 0.635 cm diameter rod, lot number E2648, was cut into approximately 5 cm lengths to fit within the inner tube. For levitation testing, pure nickel wire (99.99 wt%) was purchased from Materials Research Corporation, lot number I46-0036, with a composition shown in Table 3.1; sample preforms were prepared by cutting the appropriate length of 0.01-cm diameter wire corresponding to the desired final sample weight and winding into a tight cylinder sufficient to fit within the glass tube. Preforms were cleaned in 50% nitric acid in water and subsequently air dried after dipping in nital immediately prior to processing in the levitation facility.

Experiments were conducted using an electromagnetic levitation system for positioning and inductively melting samples for subsequent processing. Power for heating and levitating the sample was provided by a LEPEL (a trademark of Lepel Corporation, Edgewood, NY) model T-10-3 High Frequency Induction Heating Unit which is rated at 10 kW at a nominal operating frequency of 450 kHz. Induction coils were fabricated from 1/8-inch copper tubing covered with fiberglass tape and patterned from a split induction coil design. The encased sample coil employed five single-wound primary heating coils with

five upper reverse-wound turns, all of an inner diameter of 20-millimeters. The levitation coil design employed four lower primary heating coils in a double-loop 13-millimeter inner diameter pattern with two upper reverse-wound turns to increase stability. Video and pyrometry access was accommodated radially with a perpendicular view-factor in the horizontal plane between these sets of coils. Gas flow was introduced from the top of the coil assembly. Levitation specimen insertion and quenching could be accomplished from below.

Temperature measurement was accomplished using a silicon photodiode-based Capintec Ratioscope III two-color pyrometer operating at near infra-red wavelength bands centered at 0.81 and 0.95 microns. The pyrometer output was monitored in real-time on a 100 MHz pentium-based HiQ Triton P100 powerstation using a Labview version 3.1.1 virtual instrument program and a National Instruments NTDAQ version 4.8 software interface with a 100 kHz 8-channel AT-MIO-16E-10 board for a slow data acquisition rate of between 50 and 500 Hz. The program converted the raw signal to temperature by calculating the ratio of the two signals and, utilizing a calibration conversion function, displayed the thermal profile history throughout the course of the experiment to an accuracy of ± 5 K at high undercoolings. The pyrometer was calibrated using glass-encased samples into which a pyrex-shielded thermocouple was inserted. The temperature of the melt could thus be simultaneously measured to up to 200 degrees undercooling using both thermal measurement methods during subsequent multiple remelting and undercooling cycles. Thus, the confidence in measurement precision is high even for deep undercooling tests. A sample remelt cycle is shown as Figure 3.2 where a linear fit of the ratio data for the liquid intersects the curve fit for the solid at the melting point.

High speed acquisition was possible using a 4-channel National Instruments EISA-A2000 high speed analog input board for speeds up to 1 MHz by inputting the ratio directly to a buffer, configured in an overwrite loop. Camera triggering was accomplished manually by the operator or automatically using a Nicolet model 4094B digital oscilloscope

with two model 4562 plug-ins and an XF-44 twin disk drive recorder for backup data acquisition. As configured, the oscilloscope has 32 kilobytes of memory with data sampling rates of between 100 Hz (10 msec/point) and 2 MHz (500 nsec/point) with four channel data recording capability. When a recalescence event was detected by the slow channel, triggering of the higher acquisition rate channel was initiated; a parallel signal could also be sent to the video camera to retain the block of digitized images.

For levitation tests, the sample was raised into position within the argon-purged, quartz-shielded environment between the induction coils using a quartz holder. After power was activated to initiate levitation melting, the holder was withdrawn. Sample temperature was controlled by introducing a helium - 4% hydrogen gas purge to cool the sample to an undercooled state. The gas flow was set to provide a nominal heat extraction rate of 30 °C/sec based on a balance between radiative and convective losses to the environment and internal heat generation due to the magnetic field coupling.

Recalescence was thus monitored by both the pyrometer and camera with subsequent solidification in the levitated state. In most instances, recalescence was manually induced by inserting a nickel wire into the base of a levitated sample. Touching the surface instantly triggered nucleation and thus the desired undercooling could be selected. For glass-encased samples, trigger access was from above. In either case, an additional benefit was thus realized in that the nucleation site was known unconditionally from the video record.

Image capture technique

A KODAK (a registered trademark of Eastman Kodak Corporation, Rochester, NY) Ektapro HS Motion Analyzer Model 4540 was used as a high speed video recording instrument. The system has the capability of digitally storing a full frame 256 by 256 pixel image at up to 4500 frames per second, or a partial video image of 64 by 64 pixels at a

capture rate of up to 40,500 frames per second. In the camera model used in this study, 16384 frames, corresponding to 0.4 seconds total duration, may be stored at a data acquisition rate of 24.7 microseconds per frame.

The pixel intensity is recorded using a 16 element vertical array of charge coupled device photodiodes (CCD wavelength range between 550 - 950 nanometers) which scan the image plane in four sequential horizontal sweeps starting from the top left and proceeding to the bottom right side of the screen at the maximum image capture rate.

During each sampling interval, the following processes occur :

- (1) the CCD is activated and the sensor generates a charge proportional to the number of photons striking the device,
- (2) after the acquisition period, the voltage is sampled and stored in memory with each photodiode representing an individual pixel,
- (3) the detector is discharged prior to commencing acquisition,
- (4) the camera raster is used to position the CCD element onto the next pixel location,
- (5) return to step (1).

The processor operates at a rate of 24.948 MHz and thus the raster motion of the parallel detector array changes column positions at a rate of 0.04 microseconds per column. At the end of a 64 position row, the camera element must delay in order to reposition to initiate the scan of the next set of rows; this procedure takes a discrete time period known as column overhead. At the end of each frame, the camera must also delay to reset the raster to the top of the viewing area; this period is known as frame overhead. Thus, taking into account the acquisition time for each of the 64 x 64 pixels plus for row overhead periods, plus one frame overhead period, the total time from beginning of one frame to the beginning of the next is 1/40500 second, or about 24.7 microseconds, as shown in the following schedule :

$$\begin{aligned} f &= 24,948 \text{ MHz} / [(64 \text{ columns} + 80 \text{ overhead}) * 4 \text{ rows} + 40 \text{ frame overhead}] \\ &= 40,500 \text{ frames per second} \end{aligned}$$

The sensing element produces 8-bit digital images with 256 levels of gray which may be subsequently downloaded either to an image processing station using the digital download interface (DDI) software provided with the instrument or to conventional VCR tape for archiving in analog format. Individual frames were stored as tiff-files and animated through the use of the image-processing program IPLab to show the progression of the thermal front across the sample surface.

The size of each pixel is determined by the magnification factor due to lens selection and camera placement. Optical attachments included standard 50 mm and 200 mm Nikon lenses and a Questar QM-1 optical microscope. Using the 200 mm lens, typical operating distances of about 1.5 meters are required to attain proper focus and include the entirety of the sample within the field of view. This results in a pixel size of about 250 microns in diameter. At the closest approach with this lens, the pixel size may be increased to a limit of 150 microns. The lens is set to an f-stop of 11 to 16 to reduce the quantity of incident light coming from the molten surface. Using the QM-1 optical microscope, the pixel size may be reduced to 18 microns in diameter, but the sample radiance is reduced to the limits of detection by the photodiode array and this magnification currently represents a physical limit for system operation.

Image analysis technique

Image analysis was conducted on the digitized image sequence by converting the individual images from tiff format to a scripted sequence within IPLab (copyrighted by Signal Analytics Corporation, Vienna, Virginia) using a Macintosh (a registered trademark of Apple Computer, Inc., Cupertino, CA) Ilic computer. This image sequence could then be operated on by various image enhancement software scripts for display or for recovery of the original pixel values recorded in tiff format. Thus, the signal from a given pixel location could be tracked over several sequential images. Since the exact timing of the data

collection was known for each pixel in relation to all other pixels in each image, the relative location in space and time was uniquely determined for features which displayed a significant difference in observed radiance. Edge detection was easily accomplished to define droplet position - as was the interface between hot solid and undercooled liquid during recalescence.

Radiance profile

The value recorded for an individual pixel location was tracked with time to define an intensity profile. Alternately, by taking the ratio of the intensity within a given frame to the maximum steady-state value following recalescence, a radiance profile could be established. These profiles could be used to indicate the start and end of an event such as the passage of the thermal front within the limitations of the hardware response time. Since limited data scatter in intensity value occurs during equilibrium at constant known temperature (either for the undercooled liquid or semi-solid following recalescence), the relative signal noise can be defined. Note that at higher radiance, the effect of scatter is small as we are taking the ratio of large numbers and thus the radiance profile is appropriate to define the end of a recalescence event. At lower radiance, the effect of scatter is large and thus the intensity profile is appropriate to define the beginning of a recalescence event.

The signal rise time is analogous to that acquired using the optical pyrometer except for two major differences. Using standard two-color pyrometry, the ratio of the intensity of signals taken at two narrow wavelengths are used to calculate the temperature of a spot size on the order of 7 mm in diameter. Since individual pixels are tracked using the video-based system, the light frequency band is exceedingly wide and ratio pyrometry techniques are not appropriate to obtain an accurate measure of temperature. On the other hand, the spot size is significantly smaller and dependent on the lens used. The resolution measured

for the Kodak camera using the 200 mm lens was a nominal 160 microns and using the QM-1 optical microscope it was 18 microns.

In the case of the pyrometer, as the front passes across the screen the spatial resolution limits the ability to image features smaller than the spot size. The response of the pyrometer signal is seen to average the signal over the entire area and a limit in acquisition rate is reached when the ratio of the recalescence velocity and the spot size is reached. At 40 m/sec for a 7 mm spot size, a sharp interface would pass across the pyrometer target in 175 milliseconds. In order to resolve details of the recalescence event, a minimum acquisition rate of 5700 Hz is required.

In contrast, the video spatial resolution is far superior to that of the pyrometer in that the spot size can be reduced to the size of a pixel. We trade spatial resolution for bandwidth. If the video intensity signals from individual pixels within a single frame were integrated over the entire screen, a corresponding profile would be obtained which is similar in character to that obtained using the pyrometer signal. Thus, examining the timing of when widely spaced pixels are excited greatly expands the utility of the instrument.

Calibration of the response time for the signal rise on a single pixel shows that when imaging a step change in intensity, such as the sharp interface between two pieces of light and dark tape mounted on a rotating wheel, adjacent pixels appear defocused due to crosstalk. The camera electronics respond to a sudden signal rise by electronically lowering the threshold response of the array and thus dark regions appear darker near the interface and the bright edge is softened. Thus, contrast resolution for this equipment is limited to a calibrated 5 frame interval equivalent to 8100 Hz.

Velocity calculations

Glass-encased samples were held in a fixed position relative to the video camera by the container walls. Velocity calculations could be performed by tracking the progress of

the thermal front accompanying recalescence by three analysis protocols. The end-point method is based on picking the interface location on two widely spaced key frames and evaluating the average velocity over the period of interest. The linear position method involves identifying the position of the interface in each frame and plotting the location as a function of time. Both of these methods are based on evaluation of the apparent surface velocity for the motion of the tip of the dendritic array over flat sections of the sample surface. By contrast, the interface tracking method yields an average bulk velocity by accounting for sample curvature. In this method, information from across the entire sample is used to obtain an overall array velocity average.

Linear methods are not appropriate for the curved surfaces presented by levitated samples and an analogous three-dimensional interface tracking was developed for velocity calculation. The dendritic array growth is constrained by free surface interaction and utilizing an overall average velocity evaluation technique is desirable. Since sample motion could be identified from the extended videotape record, the effects of specimen rotation and translation on interface pixel position, (x, y) , could be removed by evaluating and tracking the location of specific surface elements, regardless of orientation changes with time, using a simple coordinate transformation algorithm.^[30] The image contains information about the position of surface elements in only two dimensions, and thus the third was calculated based on the assumption that the droplet cross-section was described by an ellipse. For an ellipsoidal body, the surface is described by the equation ;

$$\left(\frac{x'}{a}\right)^2 + \left(\frac{y'}{b}\right)^2 + \left(\frac{z'}{c}\right)^2 = 1 \quad (3.1)$$

where the primed reference frame is taken with the x' -axis along the major axis, a , and the y' -axis and z' -axis are along the minor axes, b and c , respectively. Since this information is available from analysis of the long duration video record, a unique determination is possible for each surface element through application of a matrix manipulation technique.

The dimension perpendicular to the image plane could thus be uniquely determined, for x and y taken from the image coordinates, by selecting the solution to the quadratic in z which was closest to the observer in that the other solution lies on the back surface of the sample. This defines the coordinates in the primed fixed frame of reference. The steps to perform the matrix manipulation are thus :

- (1) Define a key reference video frame and identify the location of the center of the droplet in order to perform the spatial manipulations with the center of rotation at the center of the droplet,
- (2) For each frame, identify the location of the interface from the two dimensional image to define coordinates in (x, y) format,
- (3) Remove the effects of droplet motion by performing matrix manipulations on the pixel values obtained to bring them into the corresponding positions in the key frame identified above,
 - (a) simple matrix subtraction to perform translation operations,
 - (b) using matrix rotation matrices, bring the axis of rotation to a known orientation (in this case the z -axis) and impose the angular displacement specific to the frame desired and then return the axis of rotation to the original position,
- (4) Transform the pixel record to the invariant primed coordinate system (x', y', z') using the spatial relationships identified from the video record,
- (5) Solve the quadratic to define two potential solutions for the location of each interface pixel in the primed system and rotate the solution back to the original key frame such that the effects of inter-frame motion can be applied to each solution,
- (6) Select the solution which is visible (closest to the observer in the image),
- (7) Perform all calculations using the appropriate coordinates selected in the invariant primed frame of reference.

Note that the order of application of the matrix manipulations is unique and when performing the operations necessary to return to the original reference frame, the order must be inverted to preserve the reciprocative spatial relationship.

The initiation of the solidification event could proceed spontaneously from a nucleation site either on the surface or from within the bulk undercooled liquid, or it could proceed from application of a physical nucleation trigger. Historical methods relied on knowing the geometric relationship between the trigger and the measurement point and utilizing the rise time to define an apparent surface velocity as seen in Figure 2.3. Using cinematography, the geometry of the trigger and the propagating front is known and a single plot is then generated to track the thermal boundary across the visible surface at successive time periods over the course of a recalescence event.

Velocity was defined as the chord distance, D , between the nucleation point and the interface pixel divided by the propagation time, t . This time is defined as the difference between when the nucleation event is assumed to occur, N_{frame} , and when the photodiode scanner acquired the specific pixel of interest, corrected for the raster motion, Δf_{raster} , of the camera sensing element.

$$V = D / t \quad (3.2)$$

$$D = \sqrt{(x_p - x_n)^2 + (y_p - y_n)^2 + (z_p - z_n)^2} * \left[\frac{\text{meters}}{\text{pixel}} \right] \quad (3.3)$$

$$t = \left\{ (N_{\text{frame}} - \Delta f_{\text{raster}}) - f_n \right\} * \left[\frac{\text{time}}{\text{frame}} \right] \quad (3.4)$$

The interface velocity was then calculated by varying the assumed position of the nucleation site within the droplet volume and iteratively minimizing the standard deviation between predicted frame velocities. The iteration proceeds over both space and time. A sample result obtained by varying the assumed time of nucleation, in units of fractions of frames,

is shown in Figure 3.3 showing a most probable value of $f_n = 0.6$ frames prior to when it was first imaged by the video.

The nucleation position was validated by comparison to the known initiation site observed during physical triggering experiments as compared to the calculated value. This treatment assumes that the velocity is constant over the period of interest and results in a calculated confidence limit of $\pm 5\%$ of the absolute magnitude of the velocity for samples in which the nucleation point was in the field of view of the high speed camera.

Table 3.1 : Material certification for nickel stock

Element	Composition	Detection Limit
<i>Glass-encased 5N purity rod</i>		
Mn	N.D.	< 1 ppm
Si	N.D.	< 1 ppm
Cr	N.D.	< 1 ppm
Cu	N.D.	< 1 ppm
Fe	N.D.	< 1 ppm
Co	N.D.	< 1 ppm
Ti	N.D.	< 1 ppm
Mg	N.D.	< 1 ppm
S	N.D.	< 1 ppm
<i>Containerless 4N purity wire</i>		
O	25 ppm	
Fe	5 ppm	
N	N.D.	< 5 ppm
Co	N.D.	< 5 ppm
Cr	N.D.	< 5 ppm
Cu	N.D.	< 5 ppm
Mg	N.D.	< 5 ppm
Mn	N.D.	< 5 ppm
Si	N.D.	< 5 ppm
Ti	N.D.	< 5 ppm
V	N.D.	< 5 ppm
Zr	N.D.	< 5 ppm

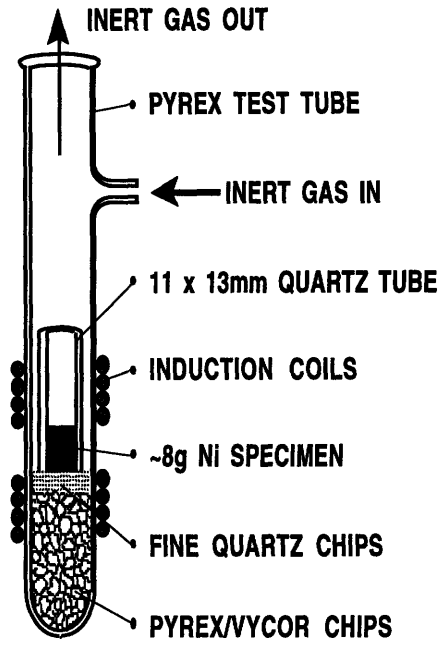


Figure 3.1 : Schematic of a typical glass-encased sample

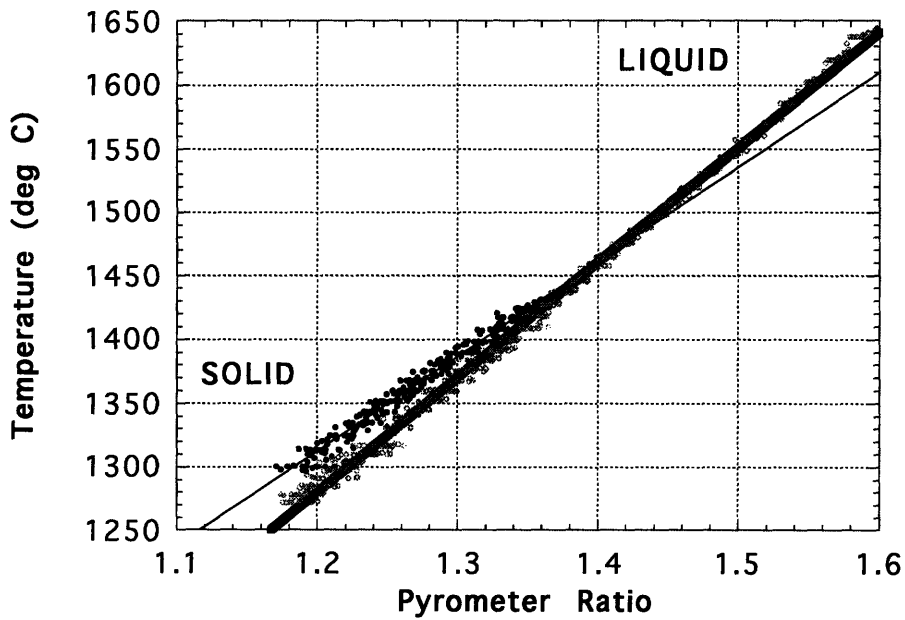


Figure 3.2 : Pyrometer calibration thermal cycle

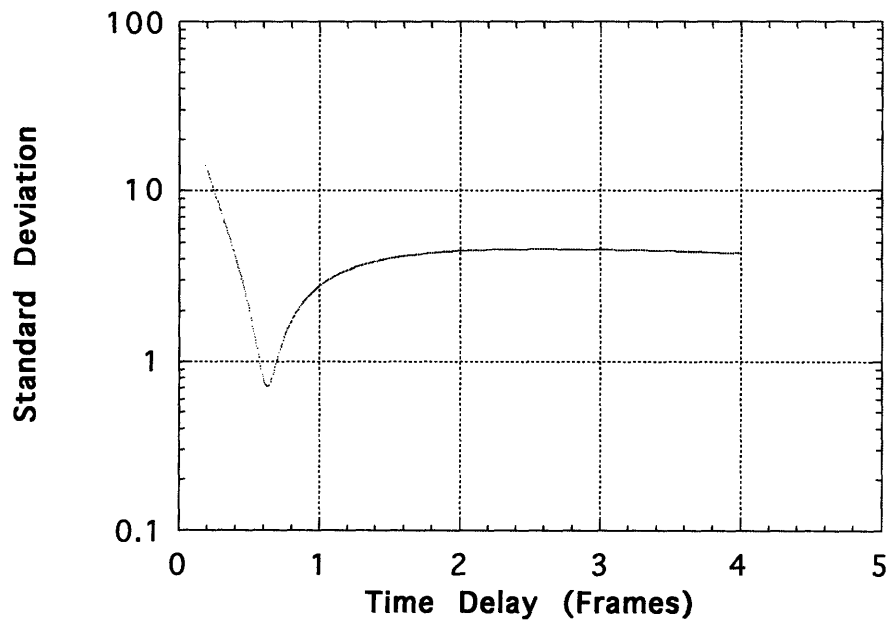


Figure 3.3 : Iterative technique to define the timing of the nucleation event

Chapter 4 : Glass-encased Processing

This chapter will describe each of the techniques used to estimate the propagation velocity during recalescence for glass-encased pure nickel samples. The relative advantages and underlying assumptions upon which the method is based can then be compared for optimal selection of the appropriate protocol based on information taken from the video record. The effects of gas environment are examined to illustrate the utility of these investigations.

In some instances one protocol is favored over another depending on the information which is desired from a specific test condition. When alignment is favorable, the end-point and linear position methods yield a best estimate of the velocity of a single dendritic array tip; propagation velocity was shown to be constant with time. The interface tracking technique is best used at high undercoolings, when isotropic growth appears valid, and when the bulk velocity is desired, based on a lack of information on local growth direction relative to the surface.

Data analysis technique

Digitized high-speed video images of glass-encased samples processed in a gas cooled environment were stored using a tiff format for importation to the image analysis program IPLab. The point where heterogeneous nucleation was initiated was selected by physical triggering using a 4N nickel wire (99.99 % pure) of the same composition as the raw material. In all cases this was the top end of the cylindrical sample at the point closest to the camera; the growth of the front thus proceeded vertically downward. A typical sequence of images is shown in Figure 4.1 for a sample undercooled 72 degrees. In this mosaic every 8th frame is shown from a digitized sequence recorded at 40,500 frames per second and thus the images are displayed at a constant interval of 200 microseconds apart.

The undercoolings achieved for glass-encased samples processed in argon are displayed in Table 4.1 along with the estimates on propagation velocity using each of the data analysis protocols described below. In Table 4.2, the corresponding standard deviation from the average velocity calculation is listed.

Three techniques were developed to analyze the video data. In the first, the position of the tip of the growing dendrite array was defined on a frame by visually picking the location of the intensity change between the dark undercooled liquid and the bright semi-solid region following recalescence. In a similar manner, the position of the interface was located on a subsequent frame. Using the screen magnification in microns/pixel from calibration tests and the time separating when the images were collected, a tip velocity was readily calculated. This technique is known as the end-point method for velocity calculation.

End-point Method for Velocity Calculation :

- (1) select initial frame for analysis,
- (2) identify interface position as a pronounced change in intensity,
- (3) select subsequent frame for analysis (this defines a time interval),
- (4) record the relative change in position over the two frames,
- (5) calculate a velocity based on the screen calibration (microns/pixel).

The disadvantage of using this method is a pronounced sensitivity to proper identification of frames over which the velocity is assumed to be constant and loss of information on the relative variability with time. Only flat sections of the sample may be processed using this method and the orientation of the propagation direction must be parallel to the surface of the melt. The obvious advantage is the ease of data evaluation and, although not necessary for a glass-encased specimen test series, the ability to remove the effects of sample translation if evident in the video record.

A second method relied on identifying the position of the front with time. The video intensity profile was surveyed to identify the critical pixel intensity corresponding to the value for the undercooled liquid prior to recalescence. The intensity is seen to rise suddenly at the interface and those pixels with an intensity greater than approximately a 20% increase over the average undercooled melt value were tracked. Using the IPLab software, the range in brightness corresponding to pixel intensities greater than this key value were selected in a process known as segmentation of the image. Segmented pixels corresponded to those locations where the recalescence front had passed.

By selecting a region of interest (ROI) corresponding to a rectangular section of the image with a width of one pixel, a linear pixel set could be computer analyzed to determine how many segmented pixels contained within the region had reached an intensity value high enough to indicate passage of the front. The analysis program counts the number of pixels above the critical value to track front position. Thus, the ROI was selected as a group of adjacent pixels oriented perpendicular to the front and parallel to growth direction. This selection was typically initiated at the point where nucleation was stimulated using the wire trigger and terminated at the point where the tip of the angular front came in contact with the image edge. As shown in Figure 4.1 this would be a vertical line tracing the downward passage of the angular array tip across the center of the sample.

A typical plot is shown in Figure 4.2 where three regions are apparent. In the first, the number of converted pixels is zero as nucleation has not been triggered until frame number -8484. At this time, the number of pixels which have an intensity which indicates passage of the front increases linearly with frame number until the entire ROI has undergone recalescence. After frame -8412 no additional increase is seen as the front continues to propagate outside the ROI. Surface position relative to the nucleation point can be obtained from the raw pixel data based on video calibration tests which define the conversion from pixel to microns. In a similar manner, the time may be obtained from knowledge of the frame rate. This method is known as the linear position method. For the

sample shown in Figure 4.1 and in Figure 4.2, the observed slope of the best fit line is 0.602 pixels/frame using the linear position method and the endpoint method returns a value of $V = 44 \text{ pixels} / 72 \text{ frames} = 0.611 \text{ pixels/frame}$. Multiplying by the screen calibration of 160.5 microns/pixel and a frame rate of 40,500 frames/second, the results in Table 4.1 for run 0508.6A are obtained.

Linear Position Method for Velocity Calculation :

- (1) select a time interval over which analysis is to be performed (start/stop frame numbers),
- (2) identify a critical pixel intensity, using a technique called segmentation of the image, which indicates position of the interface within a frame,
- (3) identify a ROI for analysis corresponding to a line of adjacent pixels oriented parallel to the direction of interface propagation,
- (4) analyze each frame to determine the interface position within the ROI,
- (5) plot linear position as a function of time to obtain the velocity.

The major advantage for using this method is that information on the variability with time is accessible and an estimation of the precision of the measurement can be obtained. From the linear curve fit, a standard deviation may be assigned.^[42] A secondary advantage for using this method is generation of a true position versus time map using information contained on all images, instead of utilizing only two key frames. Transient behavior and non-steady state propagation can be observed if they occur. Also, once the segmentation for the set of images has been selected, no operator judgement is involved in defining the position of the interface. The main disadvantage for using this method relates to the method used to select the ROI. Propagation in directions other than along either horizontal or vertical lines is cumbersome to evaluate as the program best handles adjacent pixels along these axis orientations. For skewed propagation, a series of smaller linear

ROI sections are pasted together, and a cosine function is applied to obtain the final velocity from the position/time plot since the true velocity is greater than the apparent velocity in each subregion. As before, sample curvature can not be accommodated.

The third method involves tracking of the front along the two-dimensional surface of the melt contact interface between sample and container.^[32] Here, we are tracking the average velocity of the entire dendritic array instead of focussing on a single array tip. In addition to the cylindrical shape of the sample, the contact surface is slightly distorted by the thickness of the glass container and thus the image must be corrected to obtain a true recalescence interface position especially in regions removed from the center-line axis. This was accomplished by calibrating the view using millimeter paper immersed in oil to simulate wetting of the container by the molten sample. The x and y pixel position from the image could thus be readily converted to x' , y' , and z' coordinates in video space.

After selecting the interval over which the interface motion crosses the video screen, the computation time to reach closure on the average velocity is reduced by limiting the analysis to selected frames. Typically the end-points and interval are selected to result in between seven and fifteen frames for analysis. A sequence was thus developed based on sequential display of the series of digital images and renumbered starting from zero. The key frame number when nucleation initiated, the trigger location (if visible on-screen), and the skip interval were recorded for archiving. Due to the limited number of frames at higher velocities, even if none were skipped, as few as five frames were available for segmentation.

IPLab processing of segmented images involved manual verification of the computer selection of the interface position to remove the potential for inclusion of random pixels corresponding to noise, glass surface inhomogeneities, and other false positive readings due to edge effects, optical artifacts and reflections. This was accomplished by displaying each segmented frame with the suggested interface shown in green and manually confirming the representative points in red overlay. The IPLab script then saved these pixel

locations in an x-y tiff format for each frame. These overlays were then summarized by assigning an intensity value to a file in text format for archiving. Starting from an initially blank matrix, the intensity at each point was incremented by a quantity equal to two raised to the power of the frame in which this location contained an interface pixel.

$$I(x, y) = \sum_{i=0}^N \begin{cases} 2^i & \text{(if an interface pixel is present)} \\ 0 & \text{(if no interface pixel is present)} \end{cases} \quad (4.1)$$

where I is the intensity for pixel location (x, y) and N is the frame number. These files could be subsequently deconvoluted to yield the original interface position map as a function of frame number. By saving the data in this compact format, if a single pixel position was highlighted in multiple frames, the program could recognize complex interface motion over time; this is particularly important if sample motion occurs. For example, if no interface pixels were observed for a particular x-y location, the value stored corresponding to this coordinate would be “0”; if the interface was located at this point in frame three, the value would be “8” and if it was located at this point at both frame zero and four, the value would be “17”. This information storage scheme was devised to handle both sedentary encased samples and motile levitated samples under the same protocol and thus preserves commonality in archiving to ease data manipulation.

The text file was exported to the MIT mainframe UNIX platform where a computer program coded in C was used to convert the two-dimensional position-time information to average velocity.^[32] Convergence was evaluated for a minimum in the standard deviation between frame velocities over many iterative steps in both position (in three-dimensions) and time for the occurrence of the heterogeneous nucleation event. An example of this iteration over time was displayed in Figure 3.3 for data taken from a levitated sample. Note that the minimum standard deviation based on frame velocities occurs for a nucleation event which occurred 60% of a frame before the first frame was analyzed. This is known as the frame delay time and represents the calculated time delay between when nucleation

initiated, either spontaneously or through triggering, and when the selected series of images began, as evaluated in fractions of a frame.

For the example shown : $f_n = 0.6 \text{ frames} / 40500 \text{ frames/sec} = 15 \text{ microseconds}$

A schematic representation of two frames to be processed using the interface identification protocol is shown in Figure 4.3 where the growing front is identified by the interface pixel segmentation program in the first two images and confirmed by the operator in the final image. The program calculates an average velocity for each frame based on individual pixels within that frame. This average position is shown with dashed lines. The program then iteratively compares solutions for different nucleation points and times until a “best fit” is achieved. Notice that in the example, the interface is angular and irregular in shape and thus the average interface position is a composite of the positions along the interface rather than a measure of the tip of a single dendritic array. The number of selected pixel is different for the two frames and thus if a standard deviation were taken based on individual pixel points, instead of calculated for each frame, then the position of the interface would be unfairly weighted toward the velocity obtained from the later image. Thus, to assure that each point is given equal weight, the calculation of a standard deviation is based on an interframe analysis instead of being based on pixel count. As desired, the standard deviation is a true measure of the variability between frame velocities and not a measure of the scatter within a frame.

As a comparison, the interface identification method was also run on data points selected only from the dendritic array tips. Thus, instead of tracking the progress of the entire front, only the array tip was highlighted. In these cases the computer program did not return unique solutions to the location of the nucleation time and position. This is caused by a lack of front curvature which is used to set the location of the trigger; increasing the vertical position and increasing the nucleation time simultaneously will result

in equivalent velocity average values. To this end, a limit was set on the y-coordinate such that it would agree with the position of the exposed top of the sample where triggering was initiated. The modified interface tracking method is based on additional assumptions on orientation of the surface relative to the propagation direction and is similar to the linear position method. This alternative analysis technique is known as the interface/tip method.

Interface Tracking Method for Velocity Calculation :

- (1) select a time interval over which analysis is to be performed (start/stop frame numbers),
- (2) reduce the number of frames to be processed by selecting a skip interval,
- (3) perform segmentation on the images to define interface position,
- (4) manually verify pixel selection is appropriate and representative,
- (5) save an interface progress map
- (6) export data file to analysis subroutine to generate an average velocity based on a recursive iteration on the nucleation initiation position in time and space.

This method assumes that velocity is constant and proceeds as an expanding isotropic spherical shell. Specimen curvature and motion are not ignored. The major advantage of this method is that interface data is used from across the entire frame to allow a better calculation of the average velocity under steady-state conditions. This is particularly true if the location and timing of the nucleation event are known as these values can be compared to the calculated values to anchor the computer program predictions. Favorable agreement is found.

The main disadvantage is that the method is complex and time consuming and the effect of anisotropy of the front morphology is ignored. As seen in Figure 2.5(b), at high undercoolings the growth front is spherical in shape and the assumptions on isotropic growth appear valid. At lower undercoolings, the angular shape of the front complicates

interpretation of velocity analysis results. The interaction between two effects, the geometry of the surface relative to growth direction and the complex morphology of the underlying dendrite array, can only be reconciled by selecting the best analytical technique based on knowledge obtained from the video record. As pointed out by Eckler and Herlach^[40], the uncertainty in path length results in considerable scatter in the reported velocities obtained using non-video based techniques.

The program combines the velocities obtained by tracking the intersection of the array with the surface to yield a bulk average. For instance, if a prismatic array were to intersect the surface at a slight angle, α , the surface velocity would appear excessively fast initially until the array tip intersected the surface. In two dimensions, this is due to the cosine function relationship between absolute and apparent velocity as seen in Figure 4.4 (based on the simpler three dimensional model presented in Figure 2.3 and Equation 2.20) ;

$$V_{app} = V_{abs} [1/\cos (\alpha) + \sin (\alpha) / \tan (\beta/2 - \alpha)] \quad (4.2)$$

the sharper the tip angle, β , the greater the effect.

After intersection with the surface, the back side of the array would now appear to continue growth at a much slower apparent surface rate. This is again due to the angle of approach of the dendritic array relative to the surface of the sample.

$$V_{app} = V_{abs} [1/\cos (\alpha) - \sin (\alpha) / \tan (\beta/2 + \alpha)] \quad (4.3)$$

Thus, front orientation relative to the surface and array shape affects both the surface and bulk average values observed. For example, with an intersection angle of 10 degrees and a typical array tip angle of 80 degrees, the velocity will initially appear 32% high and then, once the tip intersects the surface, appear 13% low.

This method attempts to average the effects of array shape while successfully accounting for orientation effects. None of the other methods can be used if surface misorientation is pronounced. Obviously, all video based methods are preferable to the historical pyrometry-based techniques as a decision on application of the appropriate method can be made based on a knowledge of the array geometry and the limitations of each of the techniques.

Comparison of technique performance

Table 4.1 shows the velocity as calculated by each of the three methods described above. The results from the linear position protocol and the end-point method are plotted in Figure 4.5 with a two-sigma error band shown. In all cases, the two methods return equivalent results. In Figure 4.6, the interface tracking protocol is compared to the end-point method and here a systematic error becomes apparent. Above about 70 degrees undercooling, the interface tracking method consistently predicts lower velocity results than the standard method with the error increasing until an undercooling of about 180 degrees. After this point, the error rapidly decreases and above 200 degrees undercooling, the methods return similar results.

By definition, the end-point and linear position methods are measurements of surface velocity while the interface tracking method represents a method to evaluate the bulk propagation as it intersects the surface. Two questions are pertinent :

- (1) Is velocity during recalescence a steady-state phenomenon ?
- (2) Are surface and bulk velocity the same ?

Here we define the surface velocity as the absolute array tip velocity as the front propagates parallel to the surface and bulk velocity as the absolute array tip velocity as the front passes across the sample center.

No initial transient was observed for the interface propagation velocity evaluated using the linear position method. As seen in Figure 4.2, the measured surface velocity was constant from the time recalescence was initiated using the nucleation trigger to the end of the acquisition period. If the apparent surface velocity is constant, the underlying bulk velocity must also be constant, within the sensitivity levels of these methods. If they were not the same, a transient should be apparent either at the beginning or end of recalescence; this was not observed. Thus, the assumption on constant velocity is appropriate when using both the end-point and interface tracking methods for calculating the average velocity.

It was anticipated that the interface tracking method should return results which are systematically lower than the other two methods at low undercooling due to the observed anisotropy in the region where ΔT is less than 170 degrees. This effect is seen in Figure 4.7 where an expanding equilateral trapezoid interface shape is used to compare the results from the second and third methods over eight frames. A dotted circle is used to represent the diameter of the circle which results when the average velocity is plotted to compare to the observed shape for the last frame. For the idealized geometry shown, the linear position method returns a value of 1 pixel/frame with a standard deviation of 0 while the interface tracking method returns a value of 0.966 pixels/frame with a standard deviation of 0.056 based on the geometry shown. These values are comparable but the intraframe and interframe scatter is greater for interface tracking.

For glass-encased samples, the difference observed between predicted velocity values is the most at moderate undercoolings and reaches 40% due to the errors inherent with assuming isotropic growth. For levitated samples, the difference in measured velocity due to shape effects is not as significant as anticipated in that the front morphology is not usually wholly trapezoidal in form but rather appears to approach a multifaceted ellipse due to frustration of preferred growth directions by intersection with the surface, as discussed in the next chapter. As the front shape approaches a circular shape, the differences between these two methods decrease further.

When the interface tracking protocol is modified by selecting points which define the tip of the dendritic array, the deviation from the surface velocity method becomes insignificant. In Figure 4.8 the interface, interface/tip and end-point methods are compared using a parabolic curve fit. No significant difference is observed between tip and endpoint methods.

The frame velocity variation can be obtained by comparing common samples using each of the velocity analysis protocols. For some samples, one technique will return a lower standard deviation as the assumptions which are used to develop the velocity analysis protocol may be more appropriate on a case-by-case basis. This effect is shown in Figure 4.9 where the normalized standard deviation is plotted as a function of undercooling. The standard deviation is calculated based on a non-dimensional treatment of the form :

$$\begin{aligned}
 \sigma_{ND} &= \sum (1 - V_i/V_{bar})^2 / (N-1) & (4.4) \\
 &= \sum (V_{bar} - V_i)^2 / \{ (N-1)V_{bar} \} \\
 &= \sigma / V_{bar}
 \end{aligned}$$

At higher undercoolings the average velocity is seen to increase and thus the standard deviation is adjusted to allow comparison of the variability between samples at different mean velocities. The results tabulated in Table 4.2 are not in dimensionless form, but correspond to the value of σ calculated using the conventional formula. Figure 4.9 shows that selection of the technique used can result in a better fit of the observed data based on factors which are easily identified in the video record. The overall average standard deviation for each technique appears the same; no consistent systematic difference in the behavior of the normalized standard deviation is observed as a function of method or undercooling. The frame-based deviation analysis procedure used in the interface identification method is as acceptable a measure of variability as the regressive fit used in the linear tracking technique when all samples are considered.

It is apparent that the historical photodiode sensor and the newer capacitance probe experimental methods return accurate results under selected circumstances. Specifically, samples must not have significant motion relative to the sensor, the surface shape must be well defined, and the geometry of the nucleation event must be accurately known relative to the sensing element. The interface tracking method, which returns a bulk average velocity, will show agreement with these techniques. To obtain the true local tip velocity, a modified interface/tip method is recommended for curved surfaces; this is also true for levitated samples as discussed later. If the presence of the glass container does not affect the growth velocity, then the most accurate results are obtained using an endpoint or linear tracking technique on selection of samples which show no surface misalignment to growth direction.

Growth Theory

To demonstrate the utility of these analysis techniques, the propagation velocity was evaluated for samples processed under two different gas environments. The outer containment vessel was evacuated and refilled with argon, as discussed above, or with helium / 4wt% hydrogen. An active purge blanket was maintained during the test to allow trigger access to the top of the glass-encased samples while excluding oxygen. The propagation velocity results are shown in Table 4.3 and displayed in Figure 4.10 using the end-point protocol. There is no apparent difference in the growth velocity for the two gas environments; one inert, the other reducing. Similarly, there was no difference in the observed velocity for samples tested at the beginning or the end of a series of tests using the same nickel specimen. Typical runs could last up to four hours and involve up to eight triggering tests on the same sample and thus the potential for oxygen contamination either from the container walls or from inadequate gas blanketing increases with time. Since no samples were intentionally charged with different levels of oxygen, the test series does not

disprove the theory that dissolved oxygen may enhance the propagation velocity at low undercoolings by destabilizing the tip.^[21]

Shown on Figure 4.10 are the LKT theory predictions using the physical parameters listed in Table 2.1 and using the published value of α ^[18] = 10^{-5} m²/sec for the thermal diffusivity. It is appropriate to note that the value of the diffusivity is currently under debate and different authors have used different values to fit experiment to theory. The diffusivity has been reported to be as low as α ^[43] = 0.65×10^{-5} m²/sec, and as high as α ^[32] = 1.6×10^{-5} m²/sec based on the observed experimental values. With the better accuracy of the technique developed as part of this work, the measured value reported in Table 2.1 appears appropriate. Using this diffusivity, the observed kinetic parameter of $\mu = 1.0$ is also used. This value lies between the extremes based on collision limited growth, $\mu = 2.7$, and interface attachment limited growth, $\mu = 0.001$.

In summary, the best approach to velocity measurement is to observe the morphology of the growth evident in each sample and then select the best technique using this information. Again, the advantage of a video technique is the ability to quantify the observed variability across the entire sample in addition to returning accurate bulk average and instantaneous surface velocity measurements, simultaneously.

Table 4.1 : Propagation velocity as calculated using different analysis protocols : Glass-encased samples processed in argon

Run Number	Undercooling (deg C)	Endpoint V (m/sec)	Linear V (m/sec)	Interface V (m/sec)	Int/Tip V (m/sec)
O507.1	43	1.54	1.44	1.07	1.27
O507.2	85	8.47	8.47	6.81	8.05
O508.1	190	35.29	34.04	33.51	
O508.2	133	16.92	16.97	15.36	
O508.3	224	36.83	38.24	35.59	
O508.4	110	14.25	13.24	10.03	13.35
O508.5	120	16.19	16.57	10.26	14.30
O508.6	72	3.98	3.91	3.21	3.74
O508.7	179	33.94	33.72	30.06	
O508.8	30	0.34	0.27	0.35	
O508.9	35	0.54	0.55	0.52	
O509.1	100	9.85	9.87	8.83	9.26
O509.2	109	11.21	13.31	9.03	10.14
O509.3	74	5.99	5.90	4.91	5.37
O509.4	93	10.55	8.66	8.36	9.72
O509.5	149	26.64	27.08	23.45	
O509.6	118	19.58	19.40	12.18	17.82

Table 4.2 : Velocity standard deviation for different calculation protocols Glass-encased samples processed in argon

Run Number	Linear SD (m/sec)	Interface SD (m/sec)	Int/Tip SD (m/sec)
O507.1	0.02	0.07	0.03
O507.2	0.07	0.06	0.09
O508.1	1.88	0.24	
O508.2	0.37	0.03	
O508.3	0.74	0.23	
O508.4	0.27	0.03	0.26
O508.5	0.41	0.07	0.17
O508.6	0.02	0.02	0.03
O508.7	0.48	0.49	
O508.8	0.01	0.01	
O508.9	0.01	0.01	
O509.1	0.06	0.04	0.10
O509.2	0.21	0.10	0.11
O509.3	0.04	0.06	0.13
O509.4	0.07	0.59	0.28
O509.5	0.47	0.12	
O509.6	0.18	0.18	0.13

Table 4.3 : Velocity for helium (4% H₂) test samples

Run Number	Undercooling (deg C)	End-point Velocity (m/sec)
0509.1	153	34
0509.2	192	36
0509.3	121	22
0509.4	87	9.1
0509.5	100	13
0509.6	51	2.5
0509.7	53	1.7
0509.8	60	2.8
0509.9	54	1.9
0510.1	86	5.5
0510.2	99	7.7

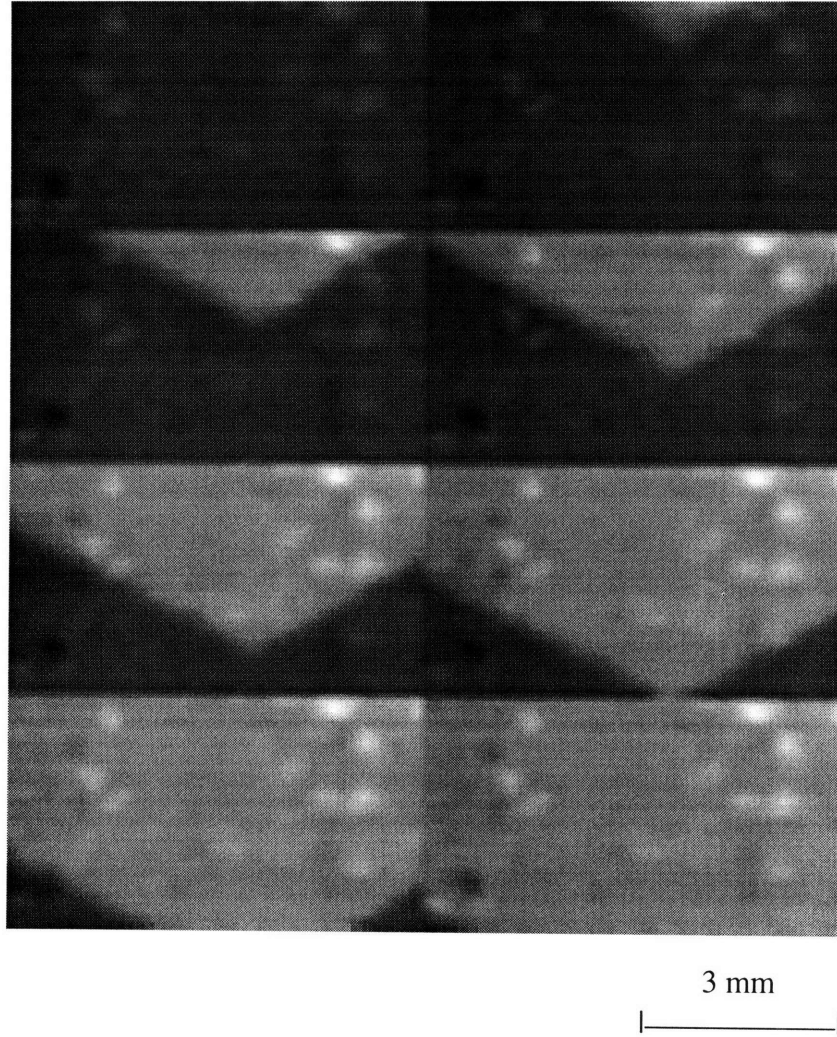


Figure 4.1 : Mosaic of images obtained for glass-encased nickel processed in argon with $\Delta T=74^\circ$ frame display rate of every 200 μsec

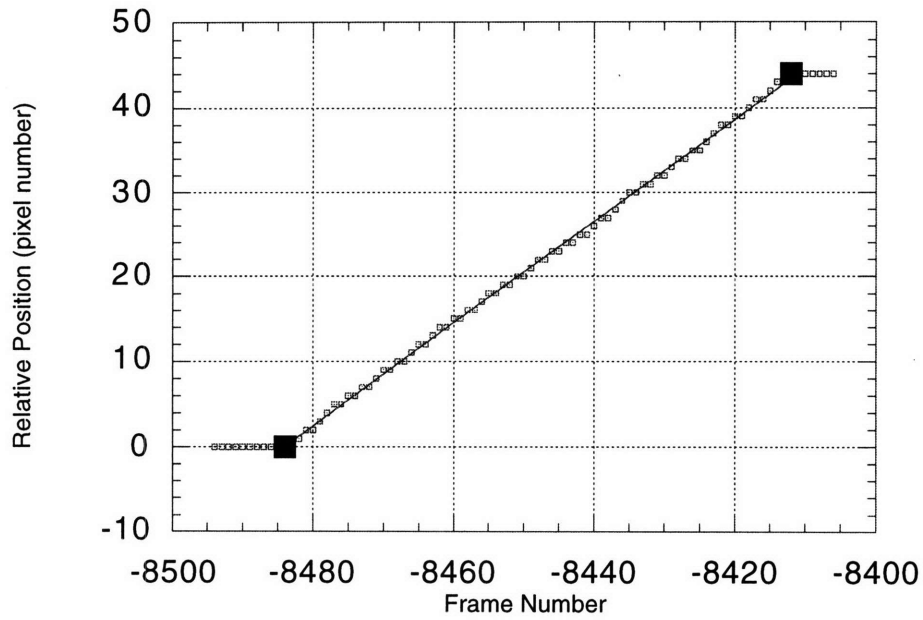


Figure 4.2 : Linear-position and end-point velocity calculation methods

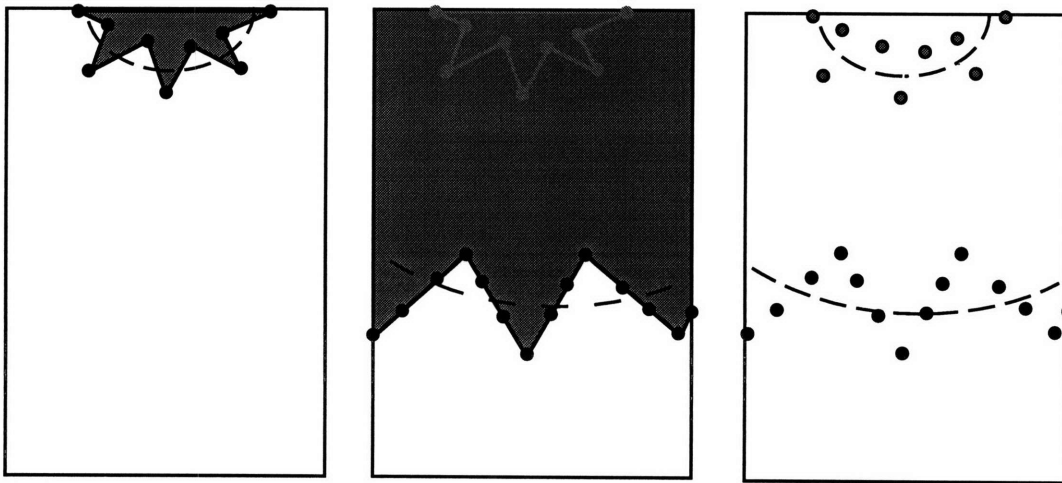


Figure 4.3 : Interface identification from video record

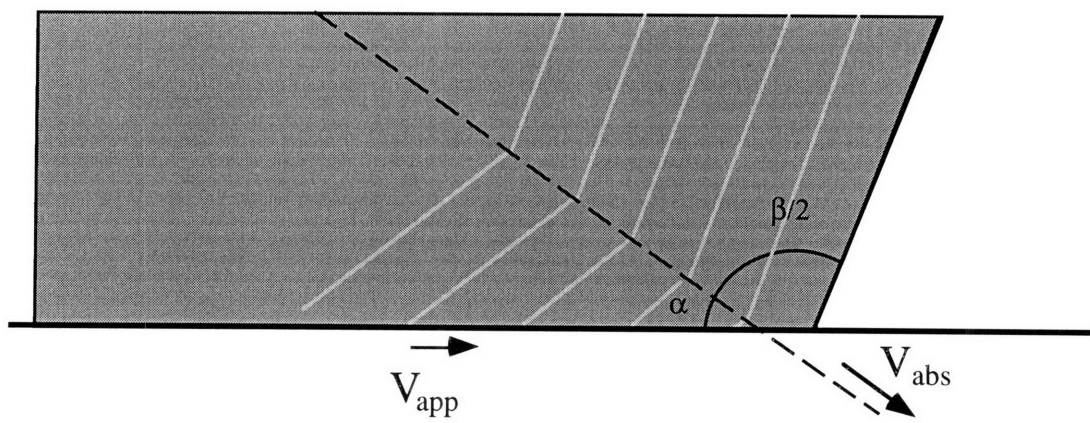
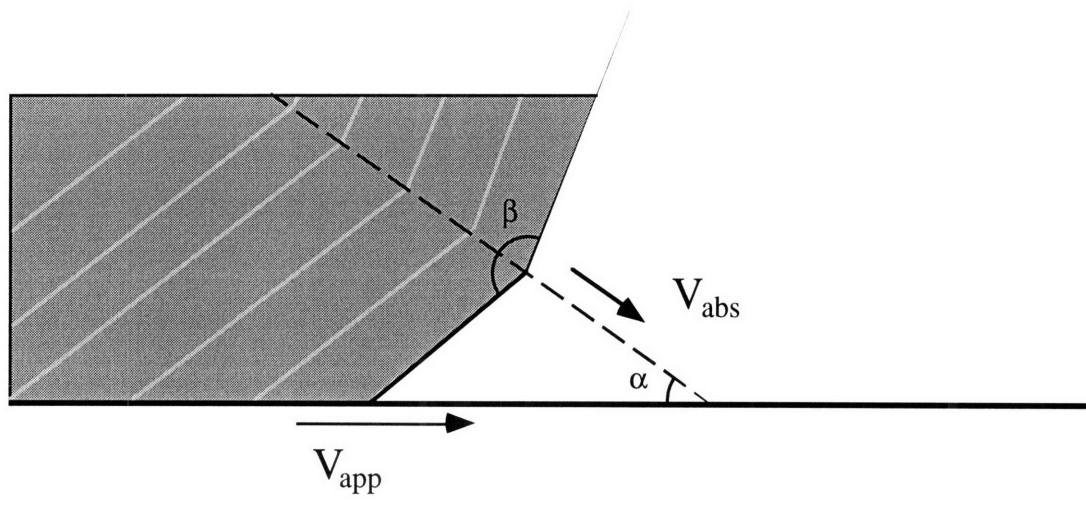


Figure 4.4 : Apparent velocity as a function of dendrite misalignment with the melt surface

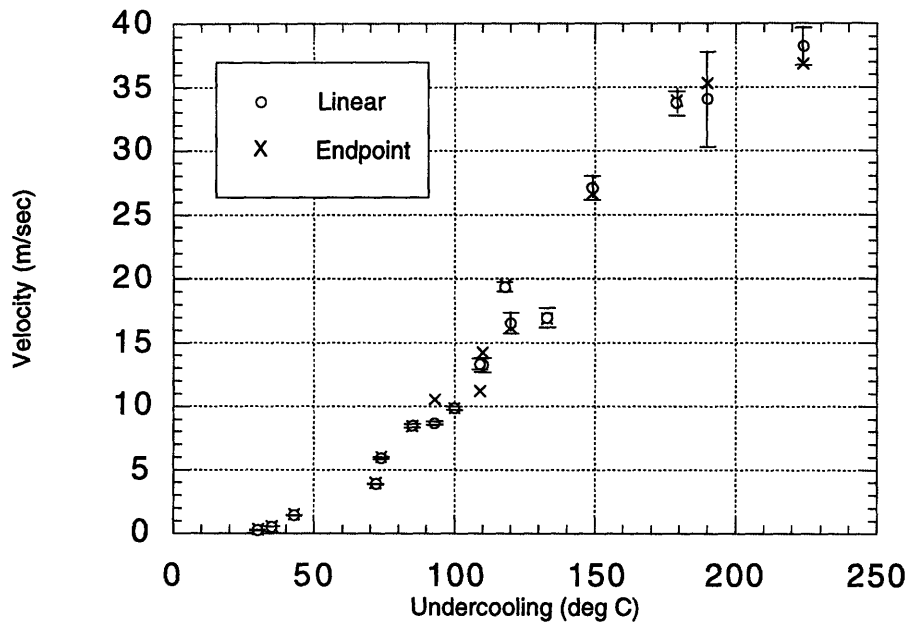


Figure 4.5 : Comparison of the results obtained using the linear position and end-point analysis protocols

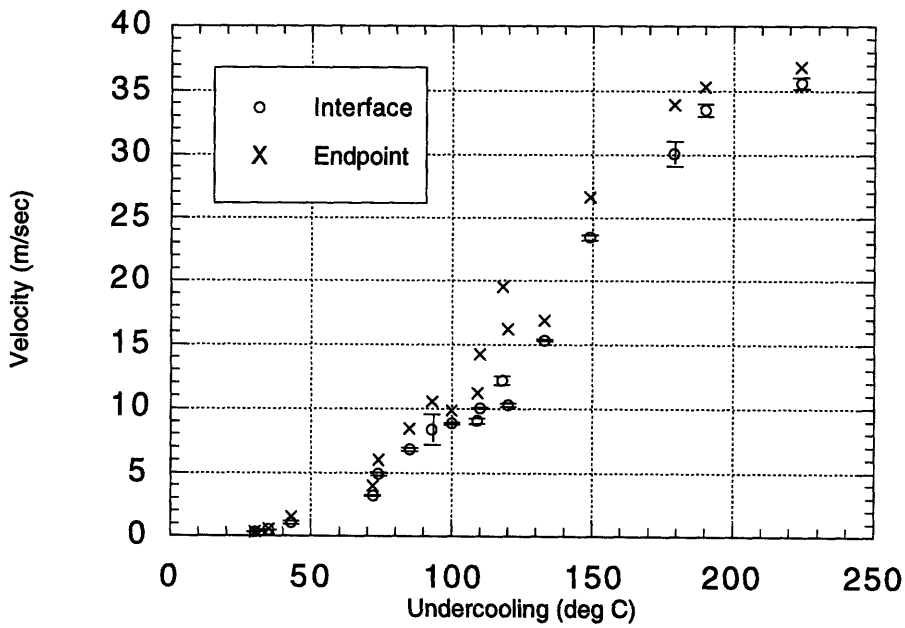


Figure 4.6 : Comparison of the results obtained using the interface tracking and end-point analysis protocols

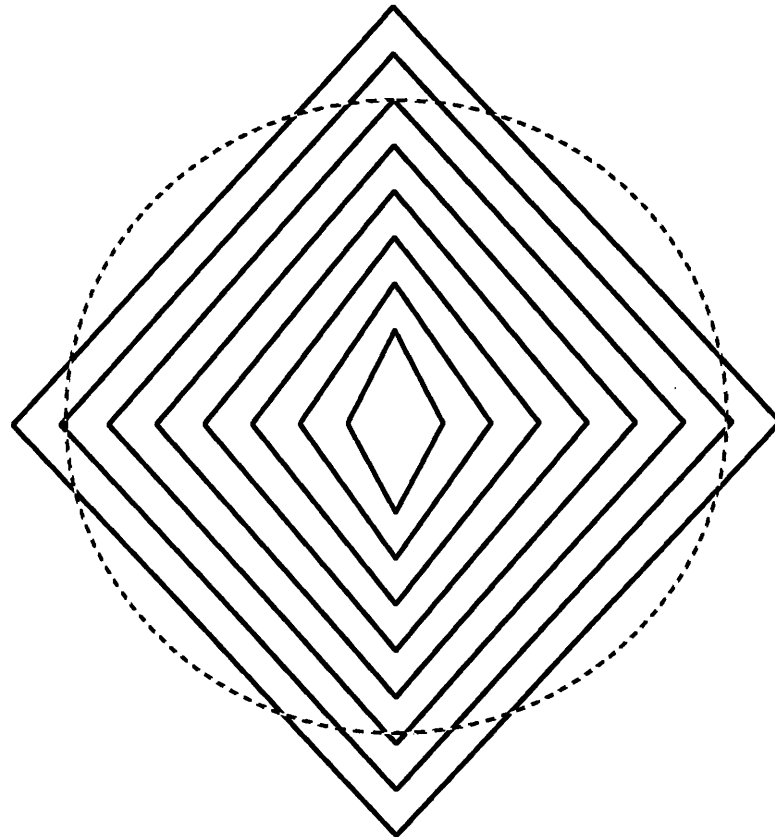


Figure 4.7 : Effect of interface shape assumption for undercoolings below the critical value

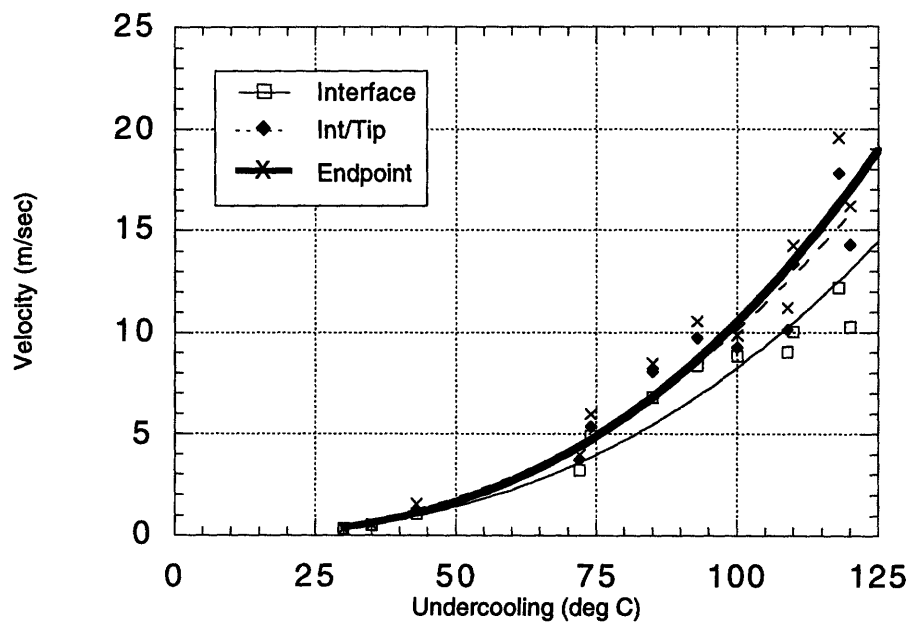


Figure 4.8 : Comparison of the results obtained using the interface and tip data selection techniques

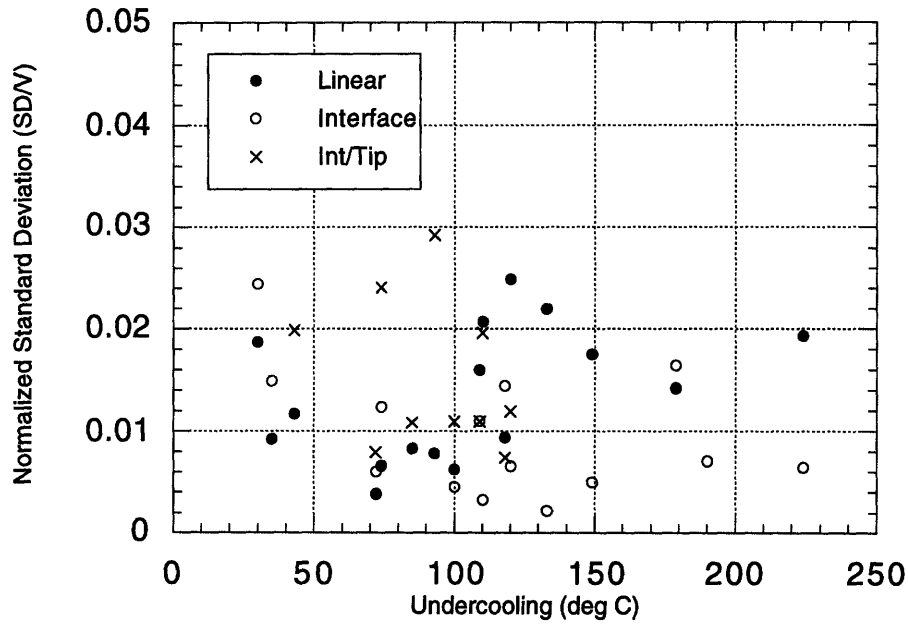


Figure 4.9 : Normalized standard deviation for each protocol

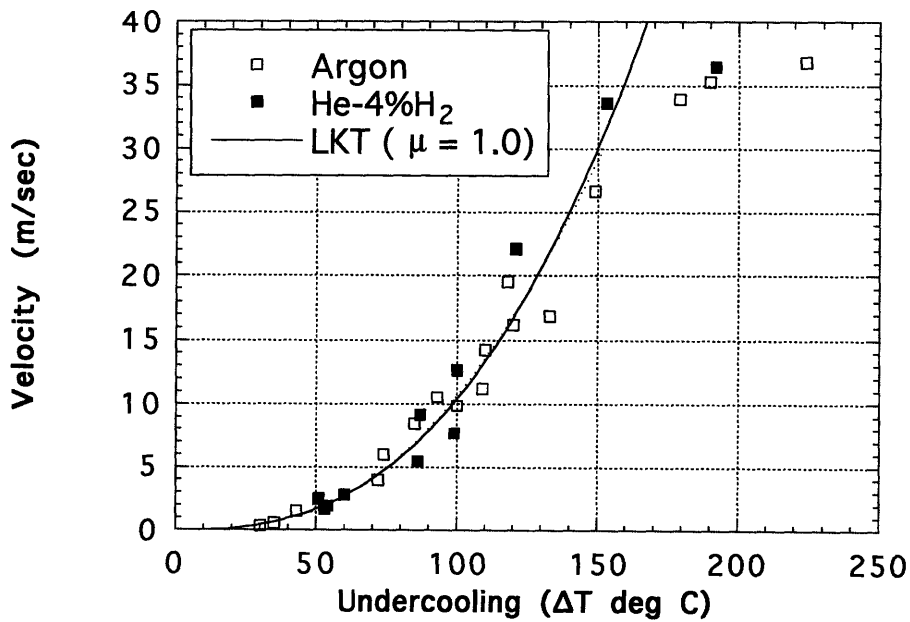


Figure 4.10 : Insensitivity to gas environment

Chapter 5 : Containerless Processing

Melt interactions with containment walls may result in a significant alteration of the physical, thermal, and chemical environment during processing. Walls may serve as heterogeneous nucleation sites and the contact characteristics can significantly affect the heat extraction rate in metals processing. By utilizing a containerless technique, chemical leaching of contaminants from the wall material into the melt is prevented. The absence of wall-related potential nucleation sites commonly promotes the attainment of higher undercoolings as well. Some alloy systems, for example the high chromium content steels, require application of a containerless technique to avoid chemical reactions between wall and melt and the subsequent degeneration of optically clear sample containment systems employed in solidification imaging investigations.

To develop a technique which is appropriate for study of the solidification velocity during recalescence under these conditions, nickel was chosen as a test material since it may be processed using both levitated and encased techniques. This chapter presents a discussion of the methodology developed for measuring the propagation of the front, and compares the containerless results to those obtained using conventional glass-encased methods to anchor the performance of this technique. Solidification imaging is then used to consider the effects of the addition of trace quantities of tin and carbon to the nickel melt in order to investigate how solute contamination alters the apparent recalescence behavior. By utilizing a containerless technique, the dilute solute concentration may be accurately controlled.

It was found that containerless processing is superior to a glass encased technique at high undercoolings due to an apparent reduction in the propagation velocity through interaction between the wall and the dendrite tip. At low undercoolings, for all sizes of levitated samples an apparent increase was observed in the front velocity as compared to glass-encased specimens. This is consistent with the consequences of melt convection, as

described by Ananth, and the magnitude of the shift was statistically significant. Experimental results are in agreement with LKT theory using a kinetic parameter of $\mu = 1.0$ for pure nickel and for nickel with solute concentrations of 1.0 at% tin and 0.6 at% carbon based on published literature values for the solute diffusivity in nickel.

Image analysis

The first technique chosen for analyzing levitated sample recalescence is similar to the previously described interface tracking protocol used to investigate glass-encased samples. In the case of the cylindrical samples, the surface was constrained by the optically clear containment vessel. In the case of levitated samples, growth was constrained by the free surface shape in response to the complex interaction between gravitational, electromagnetic, and inertial forces due to droplet motion. Gross sample translation, rotation and deformation due to surface oscillations must be accounted for.

The simplifying assumptions selected were twofold; the average velocity was assumed to be constant during recalescence and the droplet shape was assumed to be ellipsoidal in nature. Inherent in this treatment was the further assumption that surface and bulk velocities were isotropic and of the same magnitude. Note that instantaneous local velocity variation would be indicated through analysis of the standard deviation between frame velocities.

After a test was completed, the solidified product was measured to define the shape of the sample for comparison to that seen in the video record. The orientation of the major and minor axes was defined from a review of the full 0.4 seconds of digitized images (16,384 frames) available at the video rate of 40,500 frames per second. If droplet rotation is apparent, the axis and rate may be defined along with any translation of the center of mass. The centroid of the droplet was also determined in a key reference frame to allow application of matrix rotation operations on the observed surface elements.

Due to surface oscillations, the droplet shape was typically ellipsoidal in nature and by defining the set of rotations required to bring the droplet to a standard reference position, the free surface could be uniquely determined. In Figure 2.5(b), the sample appears skewed from the vertical by an angle of about 10 degrees. The digitized image represents the view as seen by the camera and was defined as “video space”. Here, the horizontal x and vertical y coordinates could be read using standard image processing programs, but no information is available on position in a direction perpendicular to the plane of the image. Thus, the z-component is unknown. What is known is that the surface is described by Equation 3.1 and using the technique described in Chapter 3, the fixed frame of reference, hereafter known as “droplet space”, could be uniquely determined. The technique is based on application of a series of rotation matrixes^[44] to the pixel record :

$$[S] = [R] \times [A] \quad (4.1)$$

where the matrix [S] represents the surface elements in the irrotational sample frame of reference following application of the translation vector, the matrix [A] corresponds to the original pixel record taken from the video screen, and the matrix [R] represents the rotation matrix.

$$[R] = R_x(\alpha_1) \ R_y(\alpha_2) \ R_z(\alpha_3) \quad (4.2)$$

$$R_x(\alpha_1) = \begin{matrix} 1 & 0 & 0 \\ 0 & \cos \alpha_1 & -\sin \alpha_1 \\ 0 & \sin \alpha_1 & \cos \alpha_1 \end{matrix} \quad (4.3)$$

$$R_y(\alpha_2) = \begin{matrix} \cos \alpha_2 & 0 & \sin \alpha_2 \\ 0 & 1 & 0 \\ -\sin \alpha_2 & 0 & \cos \alpha_2 \end{matrix} \quad (4.4)$$

$$R_z(\alpha_3) = \begin{matrix} \cos \alpha_3 & -\sin \alpha_3 & 0 \\ \sin \alpha_3 & \cos \alpha_3 & 0 \\ 0 & 0 & 1 \end{matrix} \quad (4.5)$$

where α_1 , α_2 , and α_3 are the rotation around the x, y, and z axes, respectively. An example of how this technique is applied is shown in Figure 4.1 where the orientation of the droplet shown in Figure 2.5(b) is brought to the primed reference state by applying 3 rotations. The first rotation is about the z-axis and of magnitude +110 degrees using the right-hand rule, and the second is a rotation of +20 degrees about the y-axis and the final about the x-axis -90 degrees. These manipulations, when carried out in the correct order, result in the standard droplet space frame of reference.

Thus, the video space and droplet space are mathematically related using transformation algorithms designed to remove the effects of original sample orientation and subsequent rotation and translation. Interface points are chosen from the segmented image as previously described using the IPLab script which identifies pixels with a nominal value of 25% above the background. Manual verification was desirable to prevent false positives from being included with true interface coordinates.

Pixel locations in video space were converted to a text summary file using the 2^N procedure described in the previous section. This information was subsequently exported for use in the UNIX C-coded analysis program. Here, the rotation/translation matrix was applied to digitized pixel record to obtain the surface coordinates in the standardized frame of reference and the standard deviation between frames used to determine a best fit by iteratively varying the nucleation position in space and time.

3-D Interface Tracking Method for Containerless Processing :

- (1) define sample dimensions from post-test measurement,
- (2) identify sample orientation from long-duration video record,
- (3) determine centroid position, rotation and translation from key reference frame,
- (4) obtain interface points (x, y) in video space using image segmentation technique with manual pixel verification,

- (5) perform matrix manipulation to obtain interface points in droplet space to define standard reference state (x', y', z') using the quadratic surface equation to obtain two possible solutions for z ,
- (6) invert matrix and apply to the droplet space solutions to define two possible solutions in video space, (x, y, z_1) or (x, y, z_2) ,
- (7) select the solution closest to the observer to uniquely define which solution is within the field of view of the camera,
- (8) perform recursive iteration to define nucleation position and time in the standard frame of reference and,
- (9) confirm predictions by comparison to known position (requires application of inverted matrix to convert from droplet to image space), if possible.

The advantages of using this method are that no assumptions must be made on motion - either rotation or translation - and issues of sample shape during recalescence and orientation to the sensor are readily addressed. The result is an bulk velocity averaged over the entire image record using the standard deviation between frames to statistically quantify the variability associated with the assumption of steady state growth. This allows estimation of the variation due to melt convection or droplet deformation. Most importantly, the method also allows direct comparison between predicted and observed nucleation events to anchor confidence in the velocity estimate. Under conditions of spontaneous nucleation, the method also can define if nucleation occurred on the surface or within the bulk volume of the sample.

The disadvantages include the cumbersome nature of the data collection and evaluation, the inherent difficulty associated with the assumption of constant velocity and the associated deviations due to the observed trapezoidal morphology at low undercoolings with pronounced non-isotropic growth characteristics. Unlike glass-encased samples with a long vertical dimension where steady state growth may proceed parallel to the surface,

levitated samples have no regions where sample surface curvature does not affect the growth front. At low undercoolings, the preferential growth directions are frustrated by intersection with the spherical surface and growth is severely constrained. Here, the dendritic array may start in a trapezoidal shape as seen in glass-encased samples, but the intersection of the surface with the preferred orientation occurs soon after nucleation and the sharp corners become blunted. Acute vertices become rapidly rounded or secondary array fronts become active to overcome surface frustration. It appears that even using a containerless technique, wall effects may dominate velocity measurement.

Convergence for this method is also dictated by the conditions of the specific test. Nucleation, either spontaneous or triggered, in locations not directly in the line of sight of the camera were subject to a wide range of acceptable nucleation times even when the location was well bracketed. The prerequisite to rapid convergence is a high degree of interface curvature to unambiguously define the initial nucleation site and allow rapid convergence in time. Nucleation from the back surface was difficult to analyze without forcing a solution based on a nucleation point diametrically opposite where the interface closed off at the end of recalescence. At low undercoolings with sample rotation, this was not feasible and many attempts were thus not analyzed.

The final source of error was due to the difficulty in identifying the rotation matrix, which takes surface elements and converts from video to droplet space, with sufficient accuracy to avoid removing edge pixels from consideration. To counteract this effect, the use of pixels near the sample edge is discouraged in that the error in position varies with the tangent of the angle between the surface normal and the observer and thus is greatest the farther from the droplet center the position is located; near the edge, small errors in the (x,y) coordinate correspond to large potential errors in surface position and these points should be excluded.

The second method is similar to the linear position method except that here the surface velocity is plotted across the curved free-surface of the droplet. The curvilinear

position method assumes a preferred direction of growth with the anisotropy of the interface of sufficient quantity to cause recognizable morphological features to be visible on the surface such that these features may be tracked with time. In the case of a growing angular surface, this would be one of the exposed vertices, herein referred to as a leading edge.

The object is to define the position where the apex intersects the surface such that the true tip velocity can be identified. As shown earlier, the apparent velocity is dependent on the angle of intersection with the surface and the tip angle such that after the apex contacts the surface a sudden change in apparent velocity is seen. This effect is seen in Figure 5.2 where the surface velocity is plotted as a function of frame number for the sample shown in Figure 2.5(a). The apparent surface rate increases with time as the surface curvature causes the angle of intersection to increase. Between frames -10977 and -10976 the apex strikes the surface and a discontinuous change in the apparent velocity is readily apparent. After this time, the velocity falls off as surface curvature is now creating the opposite effect. With knowledge of the apparent velocity as a function of time and the angle of intersection (based on where nucleation was initiated), analysis of the geometric relationship between the surface and the dendritic array allows calculation of the true tip angle and array shape, as well as a bulk tip velocity.

The method is based on an assumed nucleation point. This point is identified either through calculations based on the 3-D interface tracking method or through direct observation. Note that the preferred method is to calculate the position and verify this position from the video record. This provides a calculated fractional frame delay interval to be accurately identified to be used in the velocity calculation.

Curvilinear Position Method :

- (1) identify a nucleation event location and time,
- (2) define array feature location as a function of time on droplet surface,
- (3) remove the effects of surface translation and rotation through application of the matrix manipulation protocol and define coordinates in three dimensions,
- (4) evaluate the distance between the nucleation point and feature location,
- (5) if desired, evaluate apparent surface velocity as a function of time based on a calculated frame delay interval.

The advantage to utilizing this technique is that in most cases application of interface tracking protocol is required to fix the nucleation position and thus no additional calculation is required to identify the spatial manipulation matrix. The identification of interface feature location is readily accomplished while manually verifying the overall interface location. The disadvantage is that subsequent calculation of tip angles and surface intersection angles is tedious. The true value of this technique is that the location of the intersection of the apex with the surface can be confirmed.

The final technique builds on the results of the previous two three-dimensional analysis routines. The interface tracking method gives an estimate of the average velocity across the entire interface and recursively iterates to obtain the nucleation point in space and time, and the curvilinear position method locates the intersection between the apex and the surface in space and time, this method combines these results to obtain the actual tip velocity through the bulk. No surface interactions occur as the assumed path is the chord distance through the bulk along the preferred growth orientation.

Combined End-point Method for Velocity Calculation :

- (1) locate the nucleation initiation position in space and time,
- (2) locate the intersection between the dendrite tip and the surface in space and time,
- (3) calculate the tip velocity for the dendritic array.

Here, we evaluate the positions for the beginning and end of growth and make the assumption that the propagation rate is constant, as demonstrated in the previous chapter. The advantages for using this technique are that no assumptions are required for droplet orientation, motion, shape or relationship to the sensing element while utilizing all of the video record to obtain a true tip velocity. Surface induced effects are limited; anisotropy is exploited. The disadvantage is that the process does not allow for an estimate of the potential variability as it is based on phenomenon which occur beneath the surface of the melt and are not accessible except where they become visible on the surface.

Figure 5.3 shows a levitated sample of pure nickel which was nucleation triggered on the back surface by glancing contact with a nickel stimulation wire. The recalescence front progressed through the center of the droplet in the shape of a rectangular prism. Some surface features are readily apparent which allow tracking of the front progress. By applying the 3-D interface tracking protocol, the nucleation site was defined as being located on the back side with an estimated delay of 9.91 frames between when the event was visible on the front surface and when the trigger contact occurred. The tip of the array is first visible only one frames later which defines a propagation velocity of 26.1 m/sec based on the combined end-point technique. Note that the interface tracking method predicted a velocity of 12.6 m/sec for the bulk average velocity since it is based on the apparent surface velocity; due to the sharp angle of the dendrite array tip, the apex was visible before the leading edges had passed even halfway across the surface of the sample.

What then is the best technique for analyzing the growth velocity for containerless processing ? The decided anisotropy of the dendritic array results in preferred growth

orientations which must intersect the surface at some point during travel. When this occurs, further growth is halted at the liquid/gas interface in a process known as surface frustration. It is unclear how the surface frustration at low undercoolings affects the overall array tip velocity but an averaging technique is currently the best method available to define the beginning and end of bulk processes which become apparent only through interaction with the surface. A video technique is the only method which allows for accurate measurement of both the location for the nucleation initiation and where on the sample the apex first interacted with the surface. These interactions significantly alter bulk propagation for all sample configurations.

Enlarging sample dimensions to reduce surface curvature may also significantly reduce deleterious wall-equivalent effects before surface interactions become pronounced. The alternative techniques of photodiode and capacitance probe velocity measurement return results which are based on assumptions similar to those inherent in this method and, if the maximum path length is verified by measuring the droplet dimensions and assuming that the long axis was where trigger contact was most likely to occur, the accuracy of those results will rapidly approach the video technique results. Non-video methods suffer by not tracking where the surface interaction occurs and thus path length assumptions must be made.

At high undercoolings, all techniques using triggered nucleation initiation are equally valid but the use of a video technique allows for an estimation on the variability between frames and thus on the magnitude of unsteady-state behavior under particular experimental conditions.

Recalescence velocity measurements

Pure nickel samples

The results from the propagation velocity analyses are shown in Tables 5.1, 5.2 and 5.3 for levitation processed samples of pure nickel with diameter 5, 6 and 7 millimeters, respectively. These results are plotted in Figure 5.4 where the experimental values are compared to the theoretical predictions of LKT theory using a kinetic parameter of 1.0 as discussed in Chapter 2. Significant deviation occurs above the critical undercooling value of $\Delta T^* = 170^\circ \text{C}$ as described in the original paper by Walker.[22]

No apparent difference in array propagation velocity is seen as a function of levitated sample size. Calculations based on the method developed by Hyers[45], are shown in Figure 5.5 for a 6 millimeter diameter sample of nickel levitated in the coil configuration used for this test series. Flow is observed to occur in two loops with stagnant flow conditions at the sample poles and at the intersection point between the loops at an inclination of approximately 30 degrees from the sample bottom. This latter position was the location where triggering is initiated and thus growth typically started in a region characterized by lower turbulence but immediately expands out to the point where maximum flow velocity is directed perpendicular to the growing front. Note that the maximum flow velocity of 0.3 m/sec^[5] occurs along the surface within a channel depth of 0.5 millimeters - half the calculated value for the skin depth of 1.02 millimeters.

Figure 5.6 shows a comparison between the glass-encased and containerless samples as a function of undercooling. Additional glass-encased data^[32] for larger 8-gram samples is included in Figure 5.6 from Table 5.4 to show the significant difference between these sample types. At undercoolings above 190 degrees, the levitation processed material has a growth velocity approximately 15% higher than for comparable glass-encased samples. It is possible that the negative deviation for encased samples is due to an

interaction between the container wall and the growing dendrite tips but Eckler *et al.*^[21] showed that the presence of oxygen at moderate undercoolings could be responsible for an observed reduction in the growth velocity of pure nickel. Results given in the preceding chapter showed no difference between glass-encased samples tested in the beginning and end of a series but if a critical oxygen contamination level were either initially present in the alloy, exposure to hydrogen in a containerless environment could significantly reduce oxygen content. No theory currently accounts for the propagation behavior above the critical undercooling and thus the difference between a highly reducing free-surface gas environment for containerless samples and a silica flux wall for glass-encased samples remains unexplained.

At moderate undercoolings between 80 and 190 °C the two sample configurations return similar results but below this range divergent behavior may again be indicated, as seen in Figure 5.7. Comparison between LKT theory and the experimentally determined values shows an apparent positive deviation in velocity for the levitation processed material consistent with melt convection while no deviation is seen for glass-encased samples. Under levitated conditions, convection can cause a reduction in the thermal boundary layer and the corresponding increase in the thermal gradient results in a sharper dendrite tip and an increased propagation velocity from stability theory. The difference between the two sample types was statistically significant ^[46] ($t = 3.76 > t_{\alpha/2=0.0005}^{n=20,35=50} = 3.495$) and the experimental results are compared to theoretical predictions^[36, 37] for a flow velocity of $U_{\infty} = 0.5$ m/sec in Figure 5.7. Prediction of significant deviation is not apparent until below an undercooling of about 50 degrees, and since the observed deviation appears to occur at higher values, non-steady state convection may be significant in practice.

Surface recirculation was imaged by seeding oxide particles onto the molten liquid droplet and measuring the gross motion across the surface. Recirculation flow was observed to be between 0.05 and 0.2 m/sec which is of the same order of magnitude as calculated values.

Solute addition

In an effort to verify the predictive validity of LKT theory, the addition of dilute solute to further destabilize the dendrite tip was considered. By addition of a strongly partitioning element, the dendrite radius is significantly reduced due to the presence of a solute gradient and thus the velocity is enhanced at low undercoolings. At higher velocities, solute trapping decreases the solutal gradient, re-establishing a mechanism of thermal-diffusion controlled tip radius selection. These effects are shown in Figures 5.8 and 5.9 for predictions of the tip radius and propagation velocity based on LKT theory and the physical properties listed in Table 2.1 for pure nickel, Ni[1 at% Sn] and Ni[1 at% C]. Tin was selected as a solute since the diffusivity in nickel is $D_{Sn} = 5 \times 10^{-5} \text{ m}^2/\text{s}$ which is the same value as self-diffusion by nickel in the molten nickel solvent.^[17] The diffusivity of carbon in nickel^[20] is ten times faster and thus the transition from solute to thermal diffusion-control occurs at higher velocities since the solutal gradient is maintained over deeper undercoolings. In the case of addition of tin solute, the predicted radius is effectively the same as for pure nickel over the undercoolings accessed during this study; the resulting propagation velocities are thus similar. In contrast, the tip radius is significantly depressed by the addition of carbon and the difference becomes significant above an undercooling of 80 degrees.

Table 5.5 shows the propagation velocity measurements from Ni [1.0 at% Sn] experiments. The results are also plotted as a function of undercooling in Figure 5.10 and compared to theoretical predictions using LKT theory based on physical properties presented in Table 2.1. The predicted and observed values are in agreement except at undercoolings greater than 160 degrees where LKT theory fails to predict recalescence behavior, as observed for pure nickel samples.

Table 5.6 displays the results from Ni [0.6 at% C] which are compared to the data obtained by Eckler *et al.*^[21] and LKT theory in Figure 5.11. The values obtained using the

video and capacitance probe experimental techniques are in agreement with each other and with the theoretical results over the range investigated. The calculated velocity for the video-based method are slightly lower than for the capacitance probe method as the former relies on accurate measurement of the path length while the latter must assume a path based on axially aligned propagation. The video technique allows for skew between the orientation of the long axis of the droplet and the path of array to where the tip intersects the surface, and thus with an reduced path length over the same measured time interval the method returns a more conservative estimate of growth velocity.

Figure 5.12 shows a comparison between the data obtained using the combined video technique developed as part of this work and the historical data presented earlier in Figure 2.2. The new technique shows good agreement with Walker^[22] below $\Delta T^* = 170^\circ$ and then, above the critical undercooling, the results correspond to a lower limit of the data sets obtained by Piccone *et al.* ^[24] and Schleip *et al.* ^[25] These results are understandable in that Piccone did not utilize nucleation triggering and Schleip had to assume a path length. Bassler *et al.* ^[26] assumed that the front was convex through out recalescence and consequently multiple nucleation must occur to explain the existence of the various solidification lobes.

This chapter has shown that by combining the ability to predict the time and location of the nucleation event, especially when it was not directly visible from the video record, with an accurate measurement of where the apex of the array intersects the surface of the droplet, a more precise path length may be defined. This technique also provides a more accurate measurement of the propagation of the dendritic array through the bulk of the sample with limited influence due to walls or external surfaces. Measurements of the propagation velocity for nickel solutions with dilute solute addition are in agreement with predictions based on LKT theory using a value of $\alpha = 10^{-5} \text{ m}^2/\text{sec}$ and $\mu = 1.0$ for samples processed in a containerless fashion.

Table 5.1 : Velocity for helium (4% H_2) environment
Containerless 5-mm diameter levitated samples

Run Number	Undercooling (deg C)	Propagation Velocity (m/sec)	Standard deviation
0226.1	60	3.4	0.064
0226.3	73	6.7	0.107
0226.4	105	12.5	0.357
0226.5	125	14.1	0.082
0522.1	20	1.0	0.031

Table 5.2 : Velocity for helium (4% H_2) environment
Containerless 6-mm diameter levitated samples

Run Number	Undercooling (deg C)	Propagation Velocity (m/sec)	Standard deviation
0225.4	34	1.1	0.010
0225.5	124	21.6	0.972
0227.1	56	2.0	0.034
0227.2	143	28.2	0.227
0227.3	67	5.3	0.061
0227.4	88	8.0	0.098
0227.5	62	5.3	0.050
0227.6	55	4.4	0.014
0227.7	186	31.7	1.248
0227.8	153	25.1	0.359
0227.9	123	17.4	0.219
0228.1	164	29.8	0.199
0228.4	155	29.8	0.528
0228.7	194	43.4	0.320
0523.1	190	37.0	0.338
0523.2	250	46.8	0.158
0525.1	240	40.5	1.426
0525.2	220	43.3	0.065

Table 5.3 : Velocity for helium (4% H_2) environment
Containerless 7-mm diameter levitated samples

Run Number	Undercooling (deg C)	Propagation Velocity (m/sec)	Standard deviation
0522.2	69	5.1	0.098
0522.3	149	28.7	0.414
0522.4	67	4.6	0.050
0522.5	48	2.0	0.236

**Table 5.4 : Velocity for helium (4% H₂) environment
Glass-encased 8 gram samples^[32]**

Run Number	Undercooling (deg C)	Interface Velocity (m/sec)
T4/9	296	46
T4/80	262	41
T4/81	273	38
T5/58	74	4.6
T5/59	131	28
T5/60	101	10
T5/62	143	19
T5/63	110	12
T5/64	101	11
T5/65	128	20
T5/66	187	35
T5/68	113	11
T5/69	93	8.2
T5/70	119	16
T5/71	122	19
T6/27	287	47
T6/28	283	50
T6/29	285	46
T6/31	284	45
T6/32	280	46
T6/38	236	38
T6/39	203	32

Table 5.5 : Velocity for Levitated Ni[1.0% tin] samples

Run Number	Undercooling (deg C)	Propagation Velocity (m/sec)	Standard Deviation
0523.1X	102	12.3	0.318
0523.2X	113	12.4	0.536
0523.3X	104	11.4	0.302
0523.4X	61	3.7	0.055
0523.5X	72	3.2	0.021
0523.6X	79	4.5	0.036
0523.8X	141	19.7	0.177
0523.9X	176	28.7	0.417

Table 5.6 : Velocity for Levitated Ni[0.6% carbon] samples

Run Number	Undercooling (deg C)	Propagation Velocity (m/sec)	Standard Deviation
0617.1BX	95	6.8	0.207
0617.4BX	78	2.8	0.067
0617.7BX	85	2.7	0.085
0617.8BX	115	5.1	0.104
0617.9BX	110	5.8	0.099
0618.2BX	67	2.3	0.053
0618.3BX	137	14.9	0.158
0618.4BX	145	11.2	0.068
0618.6BX	50	1.8	0.066
0618.7BX	43	0.9	0.010
0618.8BX	60	2.0	0.082
0618.9BX	54	1.4	0.022

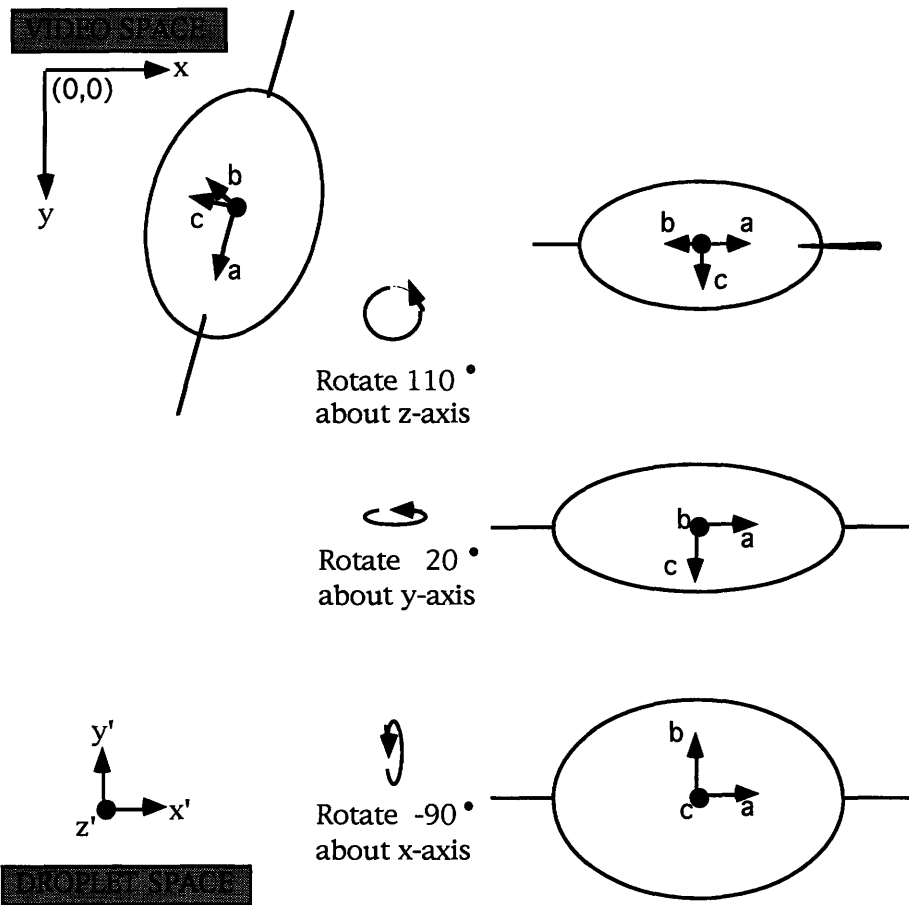


Figure 5.1 : Spatial relationship between reference frames for levitated droplets

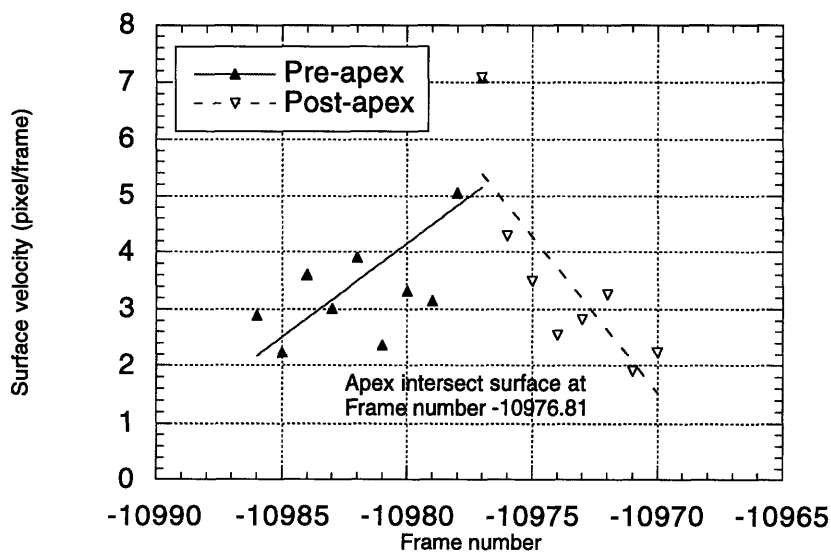
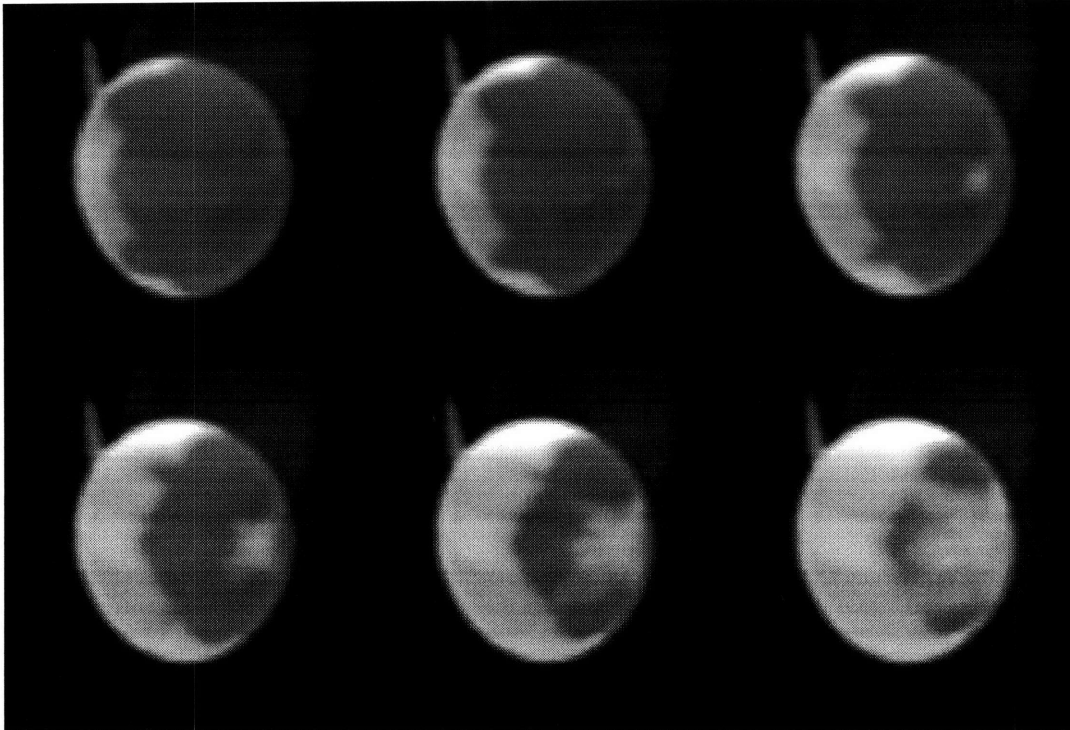
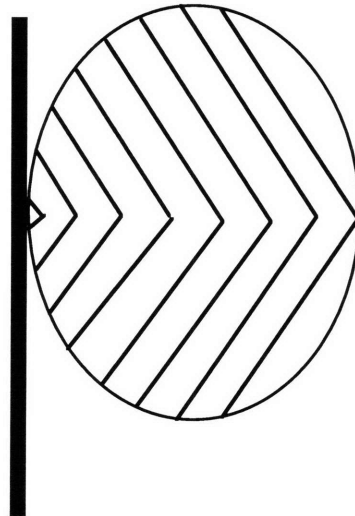


Figure 5.2 : Surface velocity during apex contact with the droplet sides at a highly skewed angle from the vertical



(a) $\Delta T = 143^\circ$ 50 $\mu\text{sec}/\text{frame}$



(b) droplet cross-section

Figure 5.3 : Analysis of bulk and surface propagation velocities
 (a) Image sequence for surface motion
 (b) Droplet cross-section to show how pattern evolved

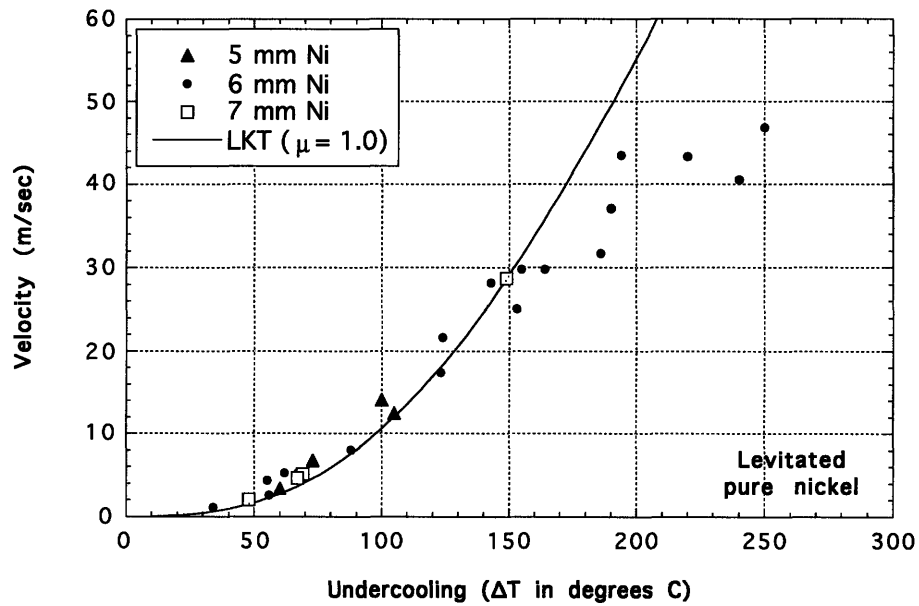


Figure 5.4 : Measured propagation velocity as a function of sample size and undercooling

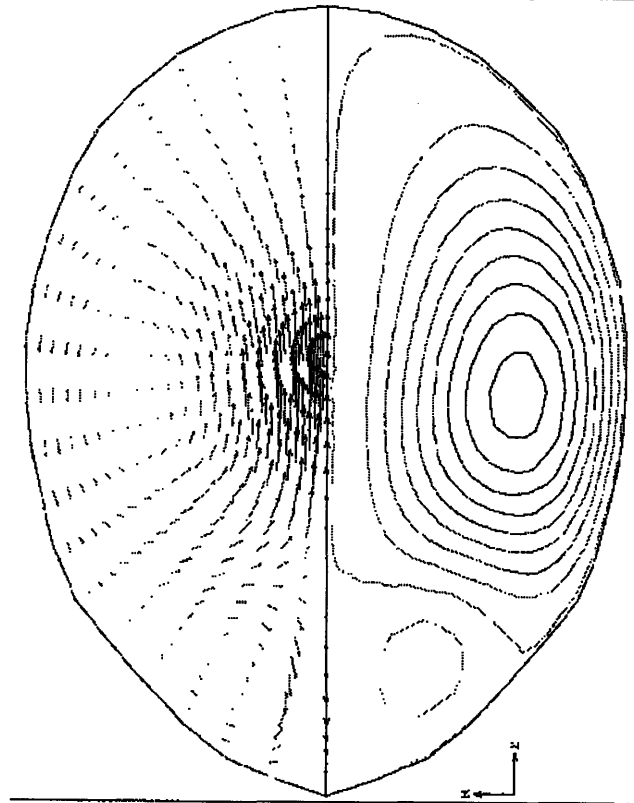


Figure 5.5 : Recirculation flow within droplet interior due to interaction with the levitation field

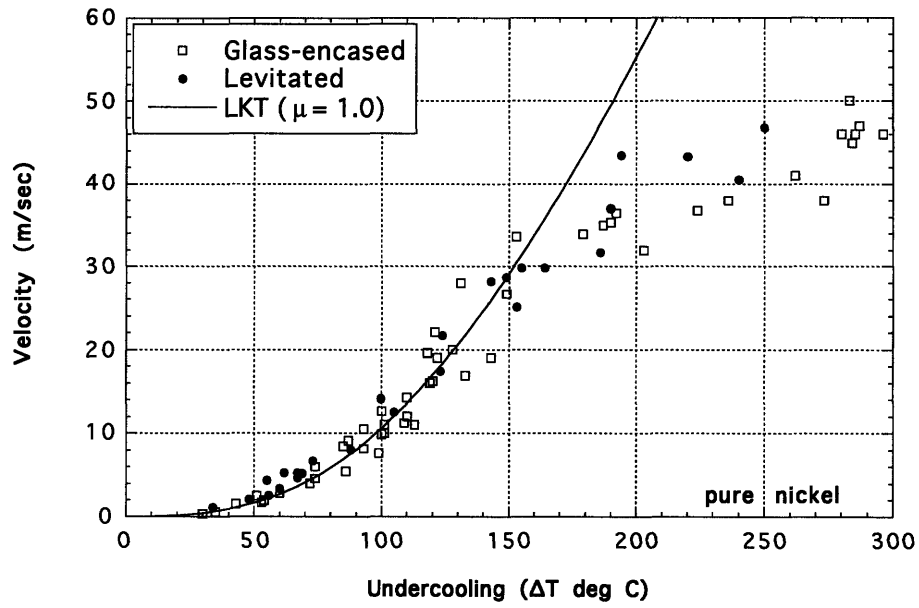


Figure 5.6 : Comparison between glass-encased and containerless processing technique for pure nickel samples

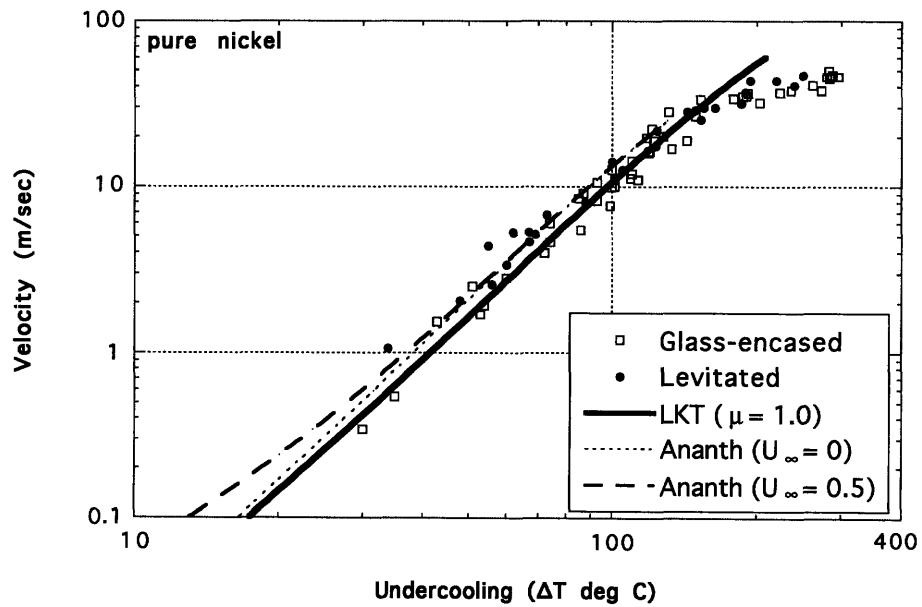


Figure 5.7 : Comparison between glass-encased and containerless processing technique for pure nickel samples

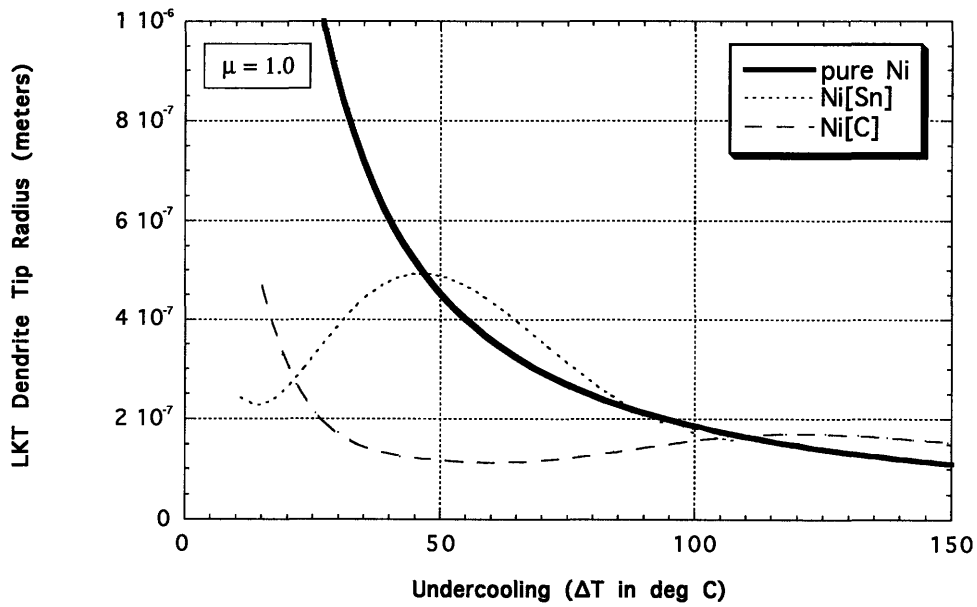


Figure 5.8 : Effect of solute addition on the predicted dendrite tip radius from LKT theory

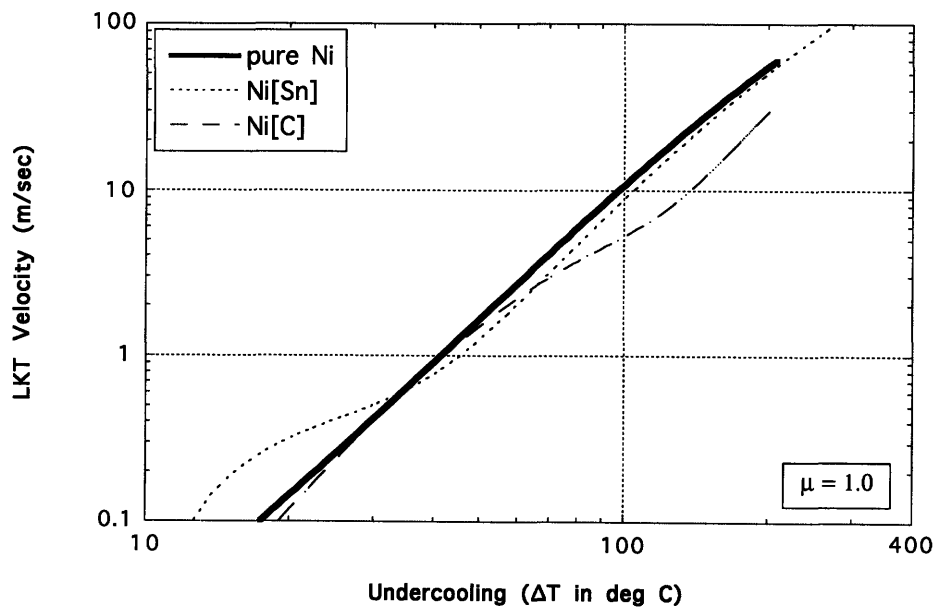


Figure 5.9 : Effect of solute addition on the predicted propagation velocity from LKT theory

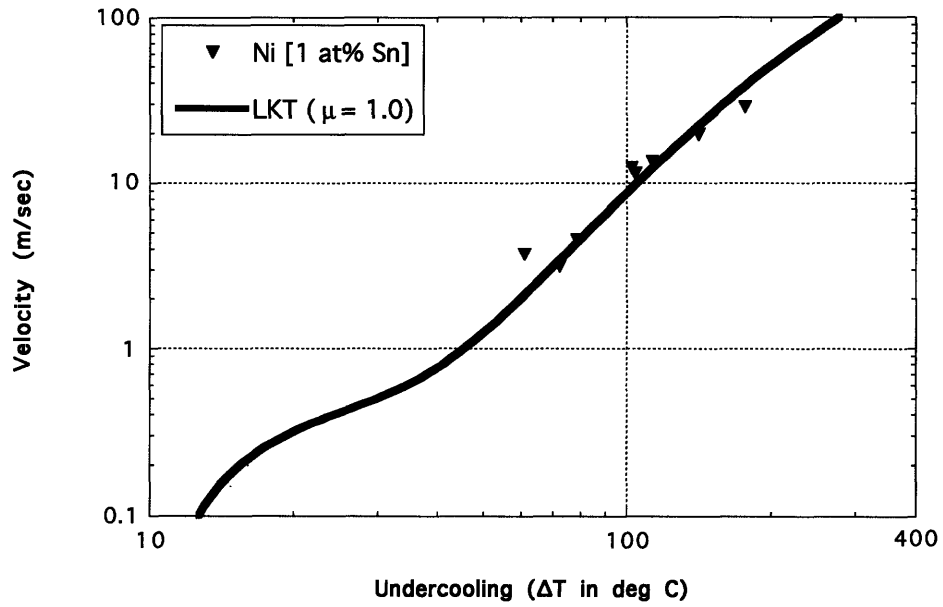


Figure 5.10 : Nickel with 1.0 atomic percent tin solute

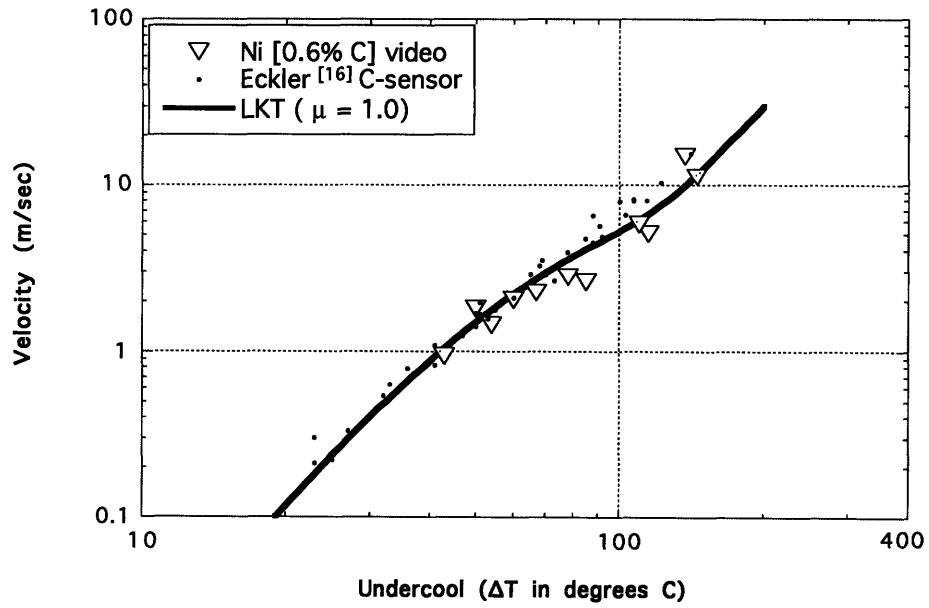


Figure 5.11 : Nickel with 0.6 atomic percent carbon

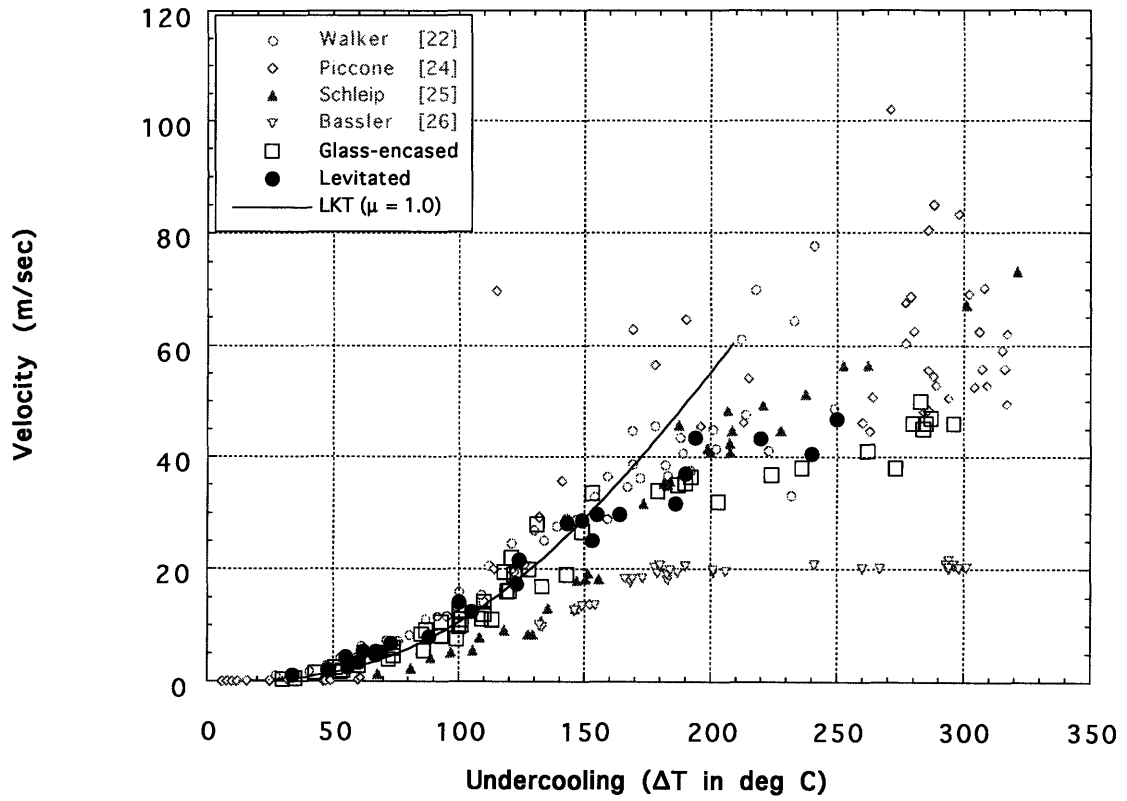


Figure 5.12 : Comparison between video technique results and historical data

Chapter 6 : Interface Morphology

In this final chapter, the morphology of the interface is investigated to determine how changes within the recalescence zone influence the gross characteristics of the front. Understanding the processes which are occurring on a microscale level are of significant relevance to optimizing industrial rapid solidification processes. In the original article, Colligan and Bayles^[41] defined two distinct interface morphologies with a sharp transition apparent at the critical undercooling. Glicksman^[16,39] has also been instrumental in forwarding the value of dendrite tip imaging in order to confirm tip radius predictions using LKT theory^[13] and the effect of convection by Ananth and Gill^[36, 37] for metallic-analog systems. Here, we have the first images taken with sufficient spatial and temporal resolution to begin to develop an understanding of the processes which occur in metallic systems at high recalescence velocities. The morphology transition is reconsidered and unique aspects of how the array structure develops are examined.

Tip splitting behavior

The following nomenclature is used to describe the array protostructure. The apex of the array is the tip of the group of dendrites which appear to move together with limited overall shape change. The array is seen to sweep forward in the form of an isosceles pyramid with the vertices commonly observed when they intersect with the melt surface. These vertices are called leading edges and can be distinguished from the apex only when severe surface frustration causes an apex to intersect the surface as discussed previously. The apparent velocity of a leading edge is commonly tracked on the surface and care must be taken to understand the underlying surface/array geometry when conducting solidification research. This is not possible with any technique other than a video-based system. Bifurcation, or symmetric splitting of the vertex, is commonly observed.

One of the most important questions raised by this research relates to how velocity measurement has been conducted in the past. Where is the dendrite tip when it is recorded by the observer in relation to the surface? For succinonitrile experiments, this is readily defined but for high speed metallic systems, the answer is not as clear. Figure 6.1 shows a series of images of a dendrite array tip as propagation proceeds from the top right to the lower center of the frame. The glass surface is pitted in this region, following many thermal cycles, and two entrapped gas bubbles can be seen in the center and center-left of each frame. As the tip progresses from where the nucleation trigger is visible in the upper right hand corner (seen as a cooler black line imbedded in the undercooled liquid) the tip travels parallel to the surface and intersects the raised bubble in the third frame. This obstacle causes the tip to split and two as seen in the sixth frame. By the eighth frame the array has reformed through some self-healing mechanism. It is important to realize that since the nucleation point was on the visible surface, these events relate to reaction by the tip to a surface feature and not from a reaction by a leading edge.

This set of images shows that the tip in fact travels slightly beneath the surface of the melt and we are not directly imaging the tip during propagation. This suggests that for true velocity measurement, some form of surface curvature is preferred in that the tip can propagate through the bulk without surface effects over much of the travel distance, and contact can then be re-established when intersection occurs. Destabilization of the tip also is an inherent aspect of propagation and the processes which set-up the stable array shape are seen to control the overall morphology of the array even when slightly perturbed. The shape also correlates with undercooling.

Tip splitting behavior is shown Figure 6.2 where the angle between adjacent tips is plotted as a function of undercooling. As the apex is the feature which is to be tracked, care must be taken to track the tip and not a set of leading edges. This effect for a glass-encased sample is shown in Figure 6.3 where the features visible are seen to propagate along lines which are separated by about 60 degrees. Bifurcation is clearly visible at all

three leading edges which indicates that the tip is propagating into the melt at a large angle. Bifurcation was also clearly evident in the levitated sample shown in Figure 5.3 where the tip intersected the surface from a nucleation point on the back side, and the leading edge contact points at each corner of the pyramid are seen to be forked.

The progression evident in Figure 6.2 is manifested on the samples by an increase in the jagged character of the front with increasing undercooling. The smooth front shown in Figure 4.1 evolves into a crown-like structure at around 100 degrees, as seen in Figure 6.4. As the critical undercooling value of around 170 is approached, the structure becomes finer, as shown in Figure 6.5, with multiple needle-like projections which seem to maintain their shape over time. The interface appears to jump forward discontinuously indicating subtle misalignment between adjacent array tips in that incidental surface contact occurs. Above the critical temperature, the front appears isotropic and expands in the spherical manner seen in Figure 6.6. Note that the angle between array tips decreases with undercooling in Figure 6.2 to zero at a temperature of around 170 degrees. An angle of near zero degrees between array tips would result in a structure which is indistinguishable from an expanding spherical shell, known as fractal seaweed,^[47] to the limits of existing spatial resolution.

The morphology transition is summarized in Figure 6.7 where the progression from angular to smooth is continuous up to the critical undercooling. Tip splitting may thus be responsible for the observed shift in behavior at ΔT^* . It also would indicate that processes which influence the tip can be expected to evolve over a continuum instead of as a discrete discontinuous shift in mechanism at the critical undercooling. This observation has profound implications on defining a mechanism for protostructural evolution and the shift in propagation behavior seen in the region around the critical undercooling.

How can we be sure that the observed tip splitting is not in fact multiple nucleation ahead of the growing front ? This can not be confirmed absolutely, but to the limits of spatial resolution, no multiple nucleation events were confirmed in this investigation. As

reported by Lum *et al.*^[32], apparent multiple nucleation in nickel-tin alloys could be traced to multiple array tips intersecting the surface from a common subsurface interconnection. This effect was also confirmed for levitated pure nickel. The interconnection is evident in that the orientation of the axes of the diamond shapes which intersect the surface over the duration of the recalescence event are commonly aligned with each other. It should be noted that if small proto-crystals could evolve ahead of the growing front, their formation at distances greater than 18 microns - the limits of spatial resolution using the QM-1 optical microscope - has not been observed. Since the thermal boundary layer and the radius of curvature for the dendrite tip are predicted to be on the order of tenths of microns, as seen in Figure 5.7, spontaneous processes would be expected to be of this length scale and hence this question has not been fully resolved.

Apex structure

Once the steady-state shape has been established, powerful scaling forces must operate to limit further randomization. Processes which occur on the microscale have macroscopic implications. Once a leading dendrite has been secured, the thermal wake which evolves tends to inhibit surrounding tips and a three-dimensional diamond pattern results. With significant anisotropy in surface energy, the tip dendrite will have side branches with defined orientation to serve as growth sites from which following dendrite tips spring. The entire array is interconnected during the initial rapid recalescence phase. Since nucleation is limited to the surface, the resulting octahedron in nickel is limited to an isosceles pyramid with a diamond-shaped surface pattern.

The diamond shape is clearly visible in Figure 6.8 where the array tip intersects the top of the droplet after nucleation on the bottom-back side. Figure 6.9 shows how this pattern can evolve long after nucleation triggering. The expanding pyramid proceeds from a nucleation point on the surface and the prism expands with its base tangent to the droplet

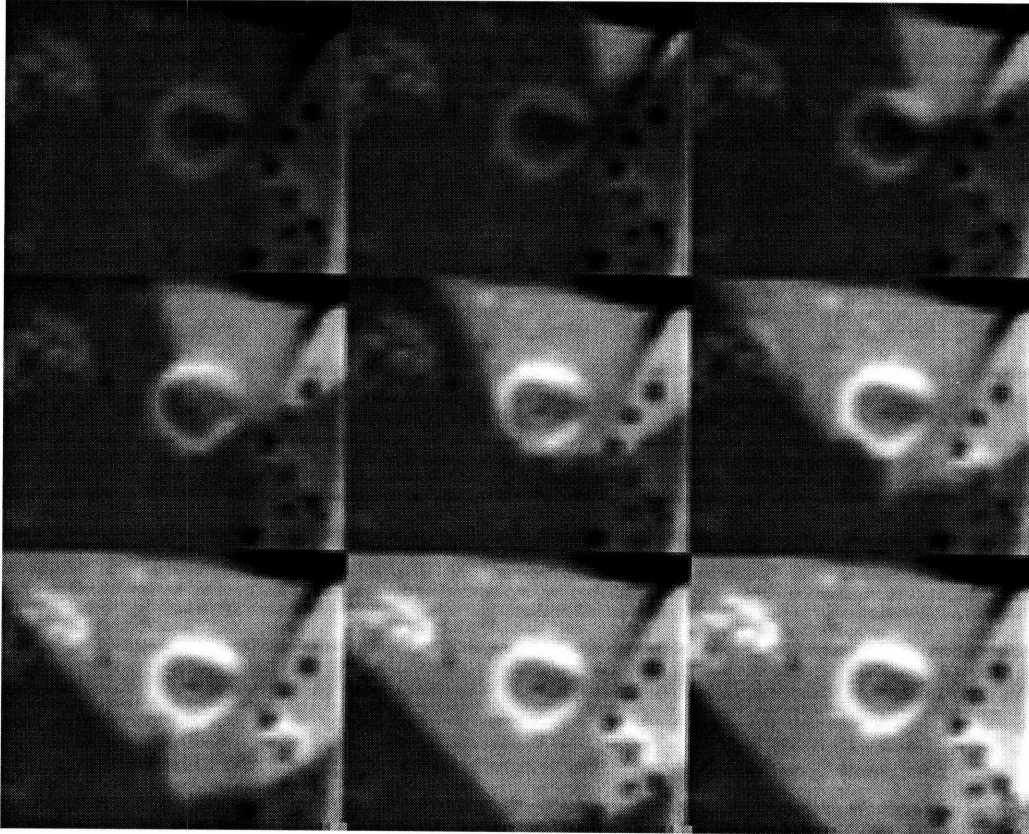
surface at this point. As the prism expands during recalescence, the growth of the solid phase is frustrated by the surface as seen in the third image in the progression. The corners become blunted and the angular character lessened. In the fourth image, the array tip is seen to intersect the droplet surface; this event could be erroneously interpreted to be spontaneous multiple nucleation but in fact is part of the subsurface structure. This event is seen in the third frame of Figure 6.8 and the third and fourth frames in Figure 5.3 discussed earlier. The leading edges intersect the surface in the fifth frames of Figure 6.8 and Figure 6.9 causing an apparent x-shape along the droplet surface. This closes off to form a fully recalesced semisolid droplet. A cross-section of this effect is seen in the second part of Figure 5.3.

What then is the subtended angle for the array apex ? Figure 6.10 shows the apex angle as a function of undercooling. The average value is nearly 90 degrees and appears independent of undercooling. The high scatter observed for glass-encased specimens is due to the disorientation of the alignment of the tip with the surface. For levitated samples, the tip angle was calculated by obtaining the surface coordinates of the nucleation point, the apex, and the location of any visible leading edges at the time when the apex first strikes the top of the droplet. By using the law of cosines from (x', y', z') coordinates, the tip angle was readily calculated. In this case, scatter is observed from the necessity of using edge pixel locations in the calculation of the leading edge location. As previously described, the error in spatial location becomes greater as the surface tangent becomes perpendicular to the (x, y) plane corresponding to the video screen. In the future, it is hoped that enough pixel locations may be identified to allow mapping of the surface of the array in three-dimensions by following the locus of points which correspond to surface intersections with time.

A remaining puzzle relates to the vertex bifurcation. As seen in Figures 6.11 and 6.12 for pure nickel and nickel [0.6 at% carbon], the forking occurs symmetrically along the length of each of the vertices. This points to either the existence of a controlling length scale or a common reaction to some internal perturbation which may cause the

initiation of the bifurcation at all points along the prism, simultaneously. Since there was no up-down or side-side variation, it is unlikely that melt convection is an important contribution to this effect. Karma^[48] has suggested that this effect may be due to a competition between surface anisotropy along $\langle 100 \rangle$ directions and kinetic anisotropy along $\langle 111 \rangle$ directions as presented by Ben-Jacob *et al.*^[49].

In summary, a morphology transition has been identified which is based on a growing octahedral structure with reaction to surface frustration imposed either by a container wall or by the free surface of the melt. Below 100 degrees, a right pyramid is observed with a gradual transition around 150 degrees to an isosceles pyramid with bifurcated vertices. Through out the transition, the apex angle is maintained by intermediary regions of concave angular solid surfaces with respect to the liquid. This destabilization results in a gradual increase in the distribution of array tip growth directions due to misalignment and adjustment of the relative angle between adjacent arrays. Between 150 and 170 degrees undercooling, massive tip splitting is proposed as a mechanism to explain how discrete array tips may be viewed as a continuous isotropic expanding surface. Above the critical temperature the fractal seaweed pattern evolves.



257 μ sec between images
 $\Delta T = 86^\circ\text{C}$

1 mm
 |-----|

Figure 6.1 : Interaction between surface discontinuity and array tip

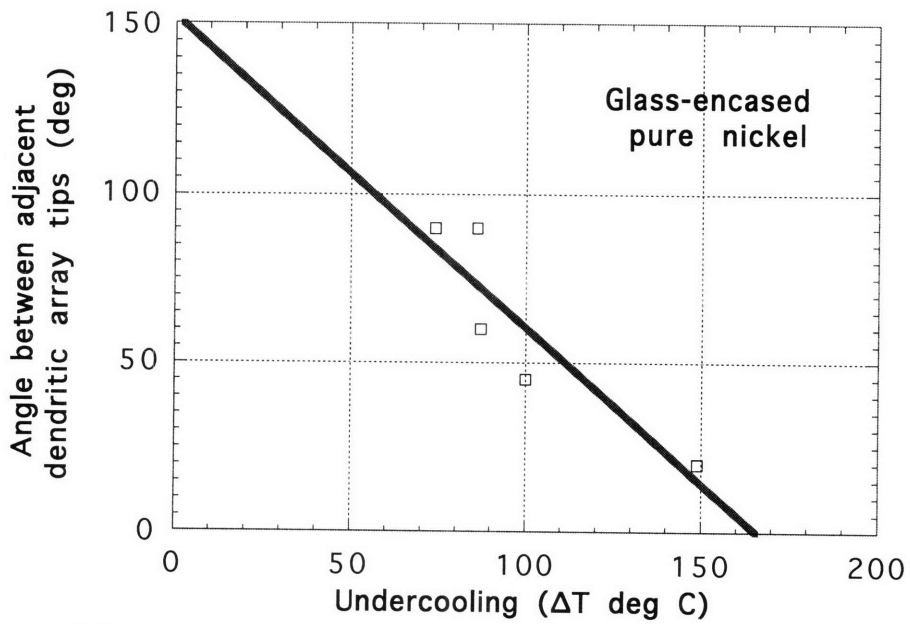
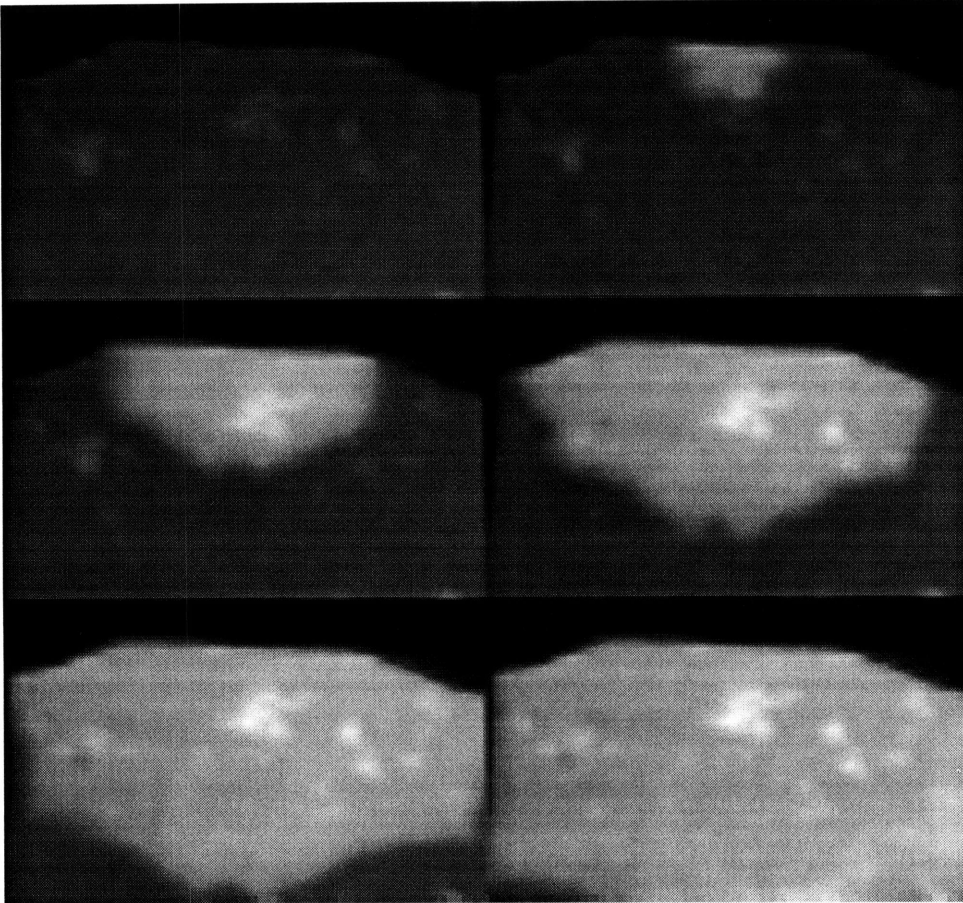


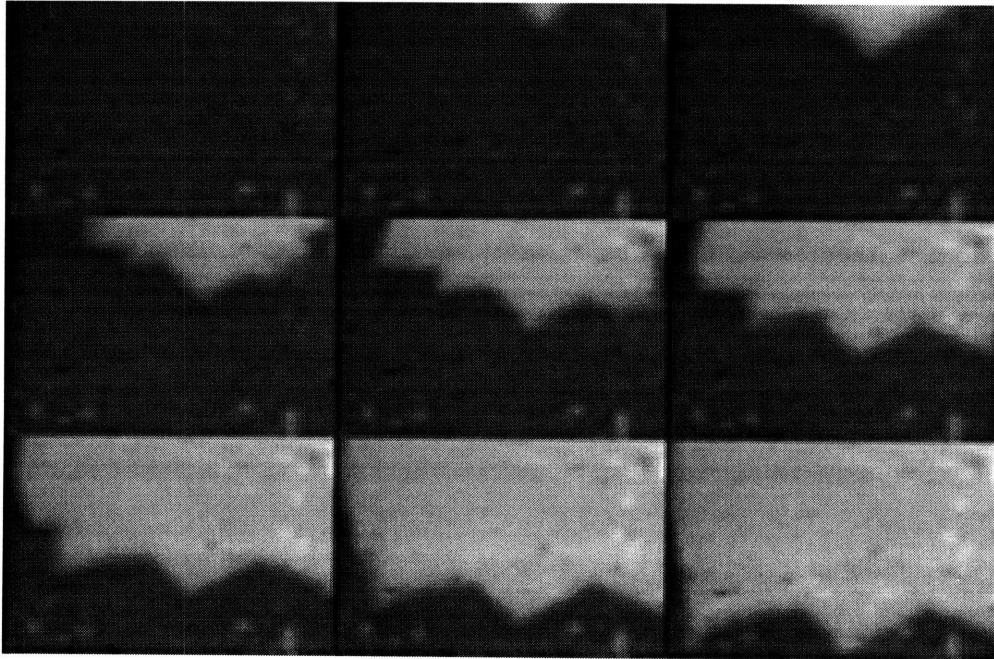
Figure 6.2 : Angle between adjacent dendritic array tips



123 μsec between images
 $\Delta T = 87^\circ\text{C}$

2 mm
|-----|

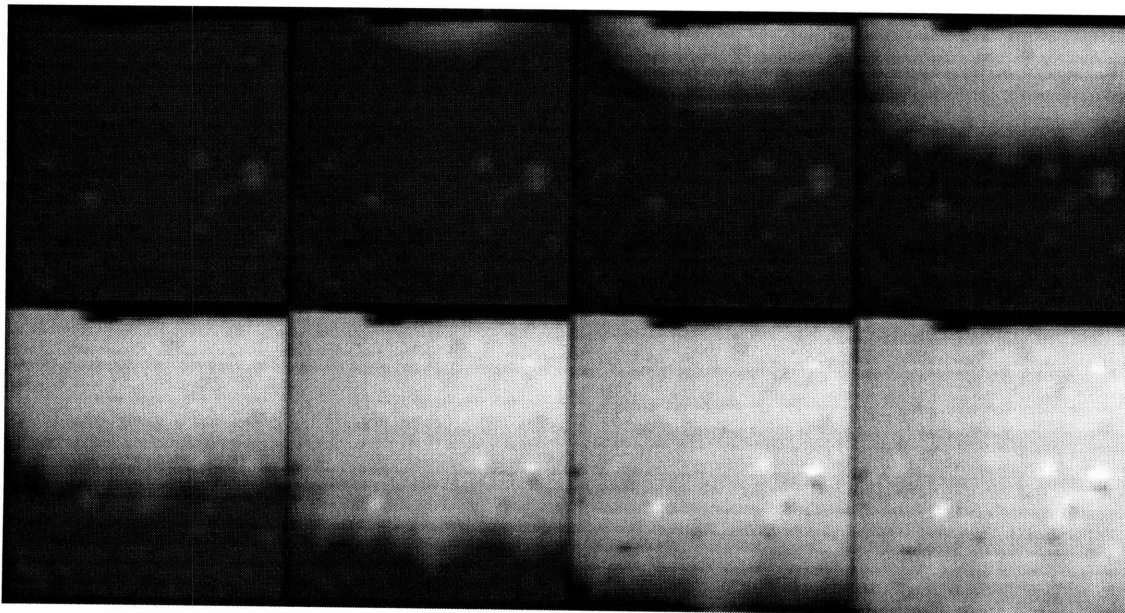
Figure 6.3 : Bifurcated vertices in glass-encased sample



74 μsec between images
 $\Delta T = 100^\circ\text{C}$

2 mm
|-----|

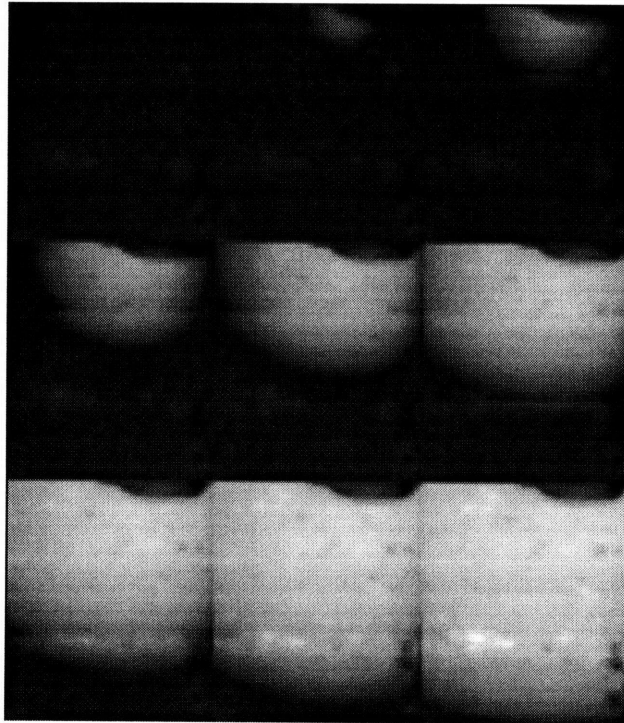
Figure 6.4 : Onset of tip-splitting behavior for glass-encased sample



49 μsec between images
 $\Delta T = 149^\circ\text{C}$

3 mm
|-----|

Figure 6.5 : Onset of isotropic behavior in glass-encased sample



25 μ sec between images
 $\Delta T = 190^\circ\text{C}$

3 mm
 |-----|

Figure 6.6 : Propagation morphology above the critical undercooling

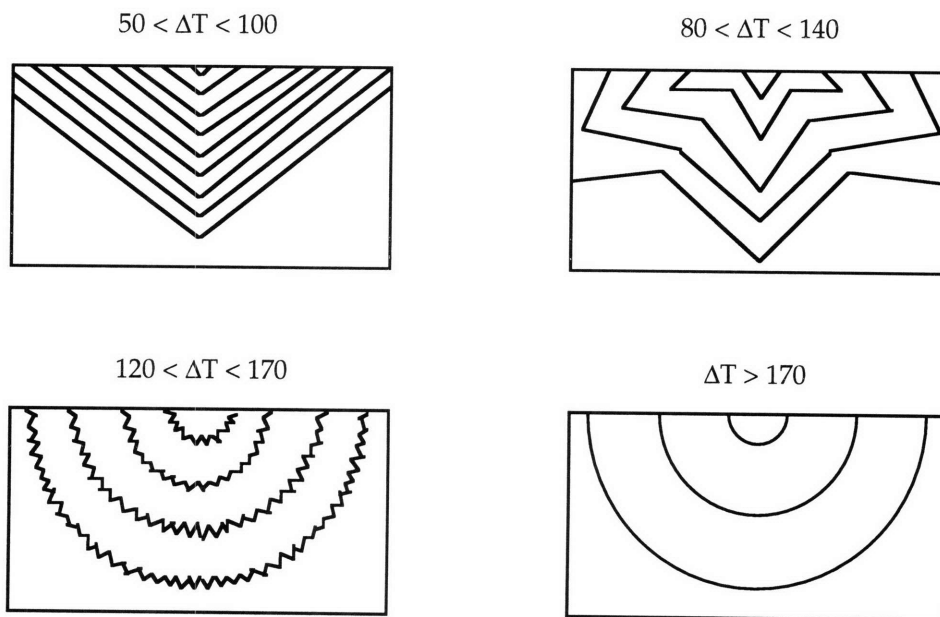
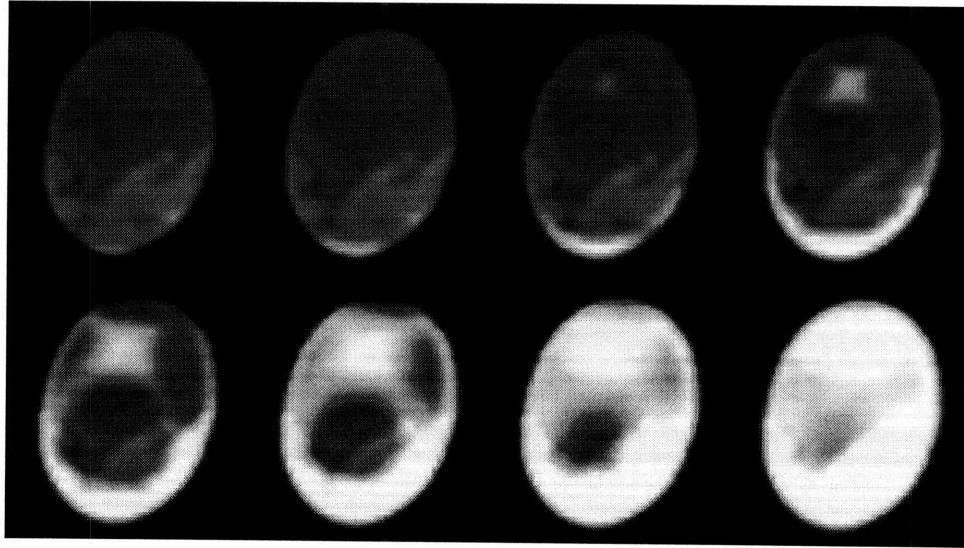


Figure 6.7 : Propagation morphology summary



25 μ sec between images
 $\Delta T = 125^\circ\text{C}$

3 mm
 |-----|

Figure 6.8 : Interaction between growing isocèles pyramid and the surface

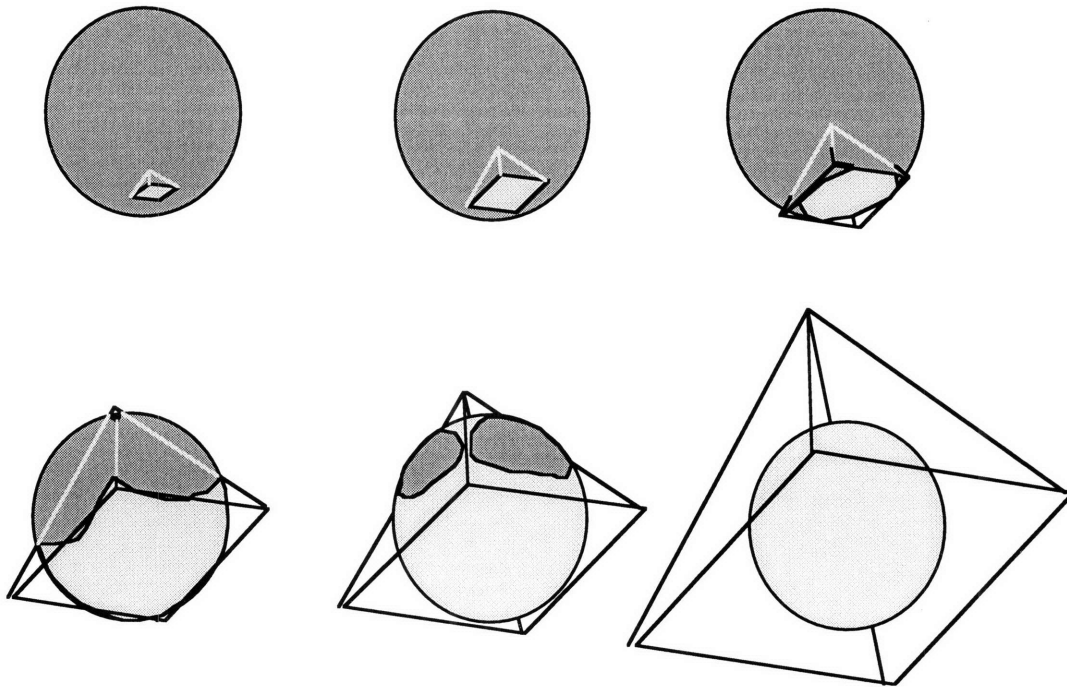


Figure 6.9 : Schematic of the intersection between a pyramidal array and the surface to obtain the observed interaction pattern

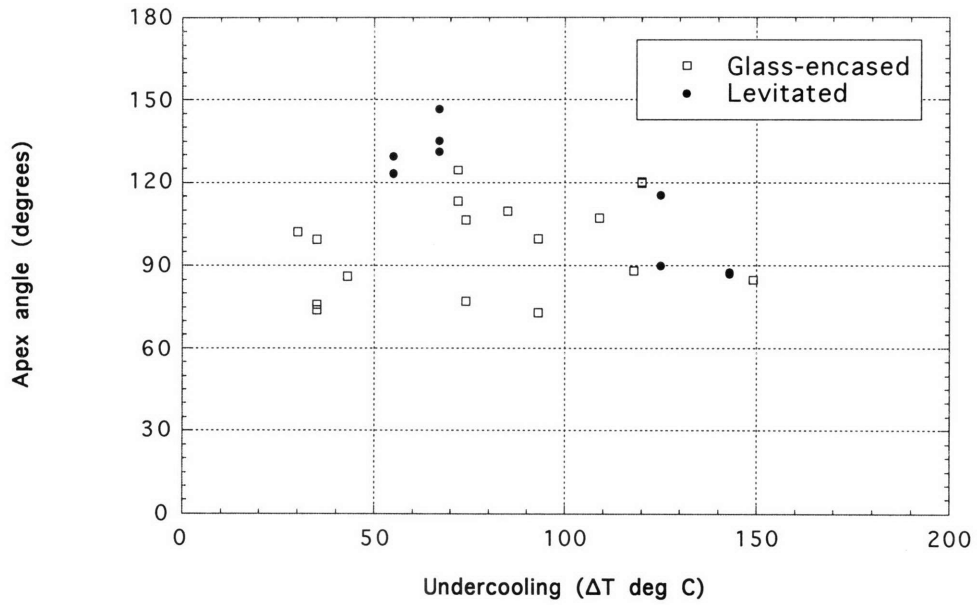
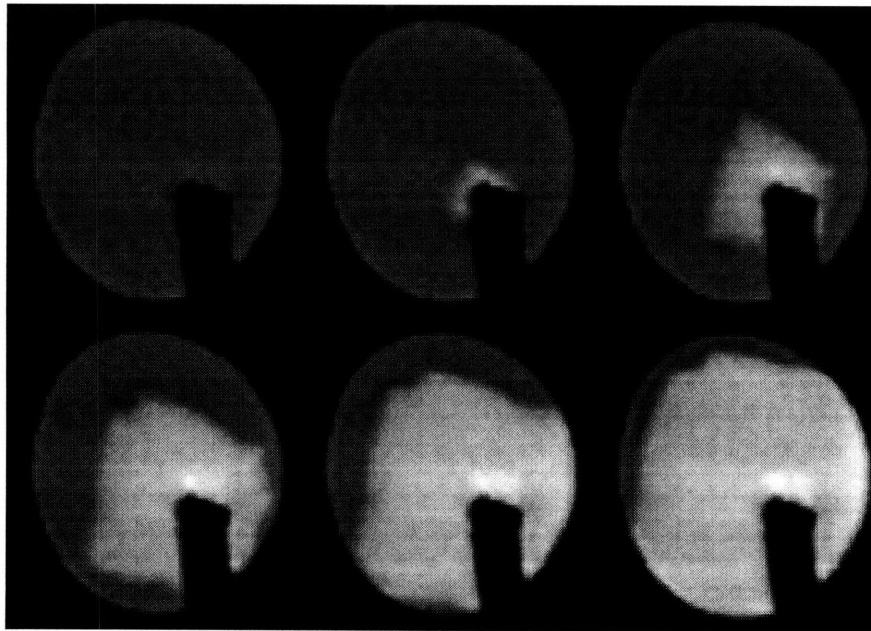


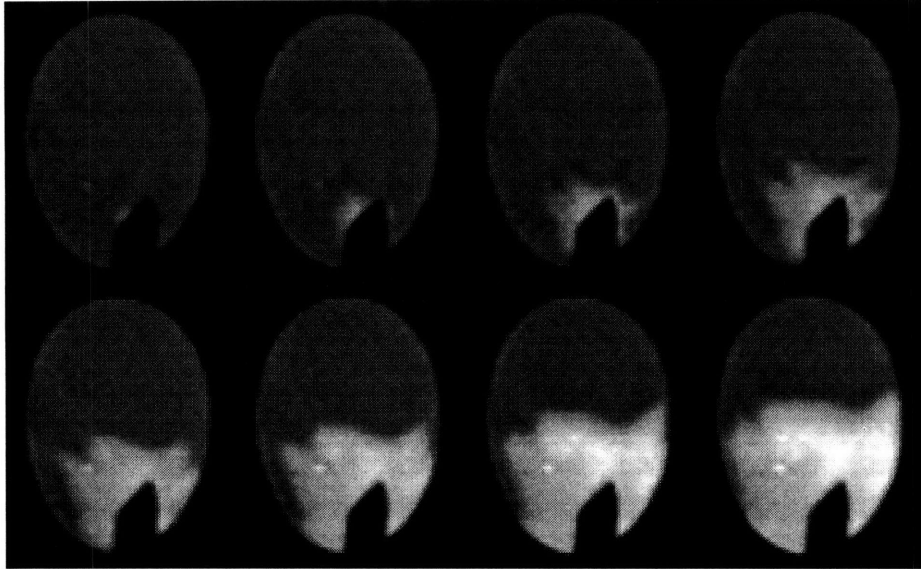
Figure 6.10 : Apex internal angle as a function of undercooling



74 μ sec between images
 $\Delta T = 117^\circ \text{C}$

3 mm
 |-----|

Figure 6.11: Bifurcated vertices in containerless processing of pure nickel



25 μ sec between images
 $\Delta T = 137^\circ\text{C}$

3 mm
|-----|

Figure 6.12: Bifurcated vertices in nickel [0.6 at% carbon]

Conclusions

Accomplishments in technique development

The conclusions which follow this brief summary are based on development of a digitized high speed imaging and analysis procedure for both glass-encased and containerless processed samples. The thermal front which accompanies solidification could be tracked by observing the difference in radiance between the cool liquid and the hot semi-solid following recalescence. Solidification from nickel melts undercooled between $30 < \Delta T < 300$ °C with recalescence velocities of $0.3 < V < 50$ m/sec were successfully imaged following spontaneous or triggered heterogeneous nucleation events.

Tracking of surface elements was accomplished by applying a matrix transformation on two-dimensional pixel positions to obtain unique three-dimensional location based on analysis of the extended video record. The effects of translation and rotation could be accounted for in order to trace microstructural evolution or identify key events during recalescence.

Under conditions where preferred growth directions were observed, the intersection with the surface of the apex of a dendritic array was used to evaluate the propagation velocity given a known nucleation position and time. An expanding spherical shell model was used to predict behavior when growth appeared isotropic at undercoolings above a critical value of $\Delta T = 170$ °C.

Solidification velocity measurement

- (1) Solidification velocity during recalescence is constant with time.
- (2) Results are independent of the purge gas environment selected for glass-encased sample testing - either inert or reducing.
- (3) Sample containment method affects the observed velocity, (a) at undercoolings of below 80 °C, levitated samples show positive deviation, (b) above 170 °C, glass-encased samples show negative deviation .
- (4) Confirmation of the predictions using LKT theory are obtained for pure nickel, nickel[1%Sn], and nickel[0.6%C] using a thermal diffusivity for the solvent nickel of $\alpha = 10^{-5} \text{ m}^2/\text{sec}$ and a kinetic parameter of $\mu = 1.0 \text{ m/sec K}$.

Interface morphology

- (1) A prismatic growth morphology was observed at undercoolings less than 80 °C with a stable front shape in the form of an expanding isosceles pyramid with an apex angle near 90 degrees.
- (2) Tip splitting was observed with a smooth transition from low temperature to high temperature behavior.
- (3) After splitting, array tips exhibited subsurface interconnection with a common preferred orientation; no simultaneous multiple nucleation events were confirmed. Bifurcation of the vertices of the growing pyramidal form was commonly observed.
- (4) At undercoolings above the critical value of $\Delta T = 170 \text{ °C}$ the front appears spherical with no clear anisotropy.

Suggestions for Future Work

The results obtained for nickel show promise for application to more complex systems. Experiments should be extended to other pure systems to prove the validity of the flow modeling results. Of particular interest would be an identification of the effects of the flow regime transition on convection by imaging surface oscillations in high viscosity alloy systems as envisioned by Professor Julian Szekely. Surface seeding of superheated melts could be used to image the free-surface flow velocity and these results could be used to anchor convection models used in this study to better understand transient and non-steady state behavior during recalescence for levitated samples. Flow modeling with systems showing a different temperature-density functional relationship would also be of merit. By modeling the flow pattern predicted for cylindrical samples under conditions of an applied magnetic field, the effects of controlled forced convection could be investigated using glass encased samples.

Extending the thermal profile analyses to complex multi-phase systems is also a fertile area for future research. The double recalescence behavior of Fe-Ni and ternary steels can be investigated to define the delay time for conversion of metastable bcc-ferritic to stable fcc-austenitic structure.

Phase selection from the melt using physical triggering and phase seeding is of interest to the steel industry for application to strip casting operations. High speed video velocity measurements will allow analysis of the effects of primary recalescence on the growth morphology of subsequent transformations and quenching experiments will be useful to identify the mechanisms which operate during post-recalescence coarsening and massive transformations. The role of solute segregation on non-steady state propagation velocity evolution may also be of interest. One of the most fascinating possibilities is tracking the growth of the stable phase into the semi-solid region following primary

recalescence. The effect of fraction solid and hold time on the velocity will yield information on the coarsening of the metastable structure between recalescence events.

In space, the role of forced and natural convection on recalescence behavior can be minimized due to the absence of gravitational effects. Here, density driven flow and Marangoni surface tension effects will dominate fluid motion. Velocity imaging tests on pure nickel and nickel 0.6 wt% carbon is planned in collaboration with the group headed by Dr. Dieter Herlach and microgravity solidification testing will be conducted during the upcoming MSL-1 shuttle mission. The method presented as part of this work will be used to provide ground-based support for understanding the effects of melt convection on samples triggered at low undercoolings. Velocity imaging is used to interpret the results obtained using conventional pyrometer-based velocity imaging techniques. Baseline testing on the effects of melt convection on the delay time for metastable phase transformation for steel alloys under terrestrial and microgravity conditions will be conducted as part of the same mission by the author.

Bibliography

- [1] M. C. Flemings, Solidification Processing, McGraw Hill, New York, NY, p. 294, (1974).
- [2] D. M. Herlach, R. F. Cochrane, I. Egry, H. J. Fecht, and A. L. Greer, "Containerless processing in the study of metallic melts and their solidification", *Int. Mat. Rev.*, **38**[6], pp. 237-347, (1993).
- [3] D. M. Herlach, "Non-equilibrium solidification of undercooled metallic melts", *Mat. Sci. Eng.Reports*, **R12**, pp. 177-272, (1994).
- [4] J. Szekely, E. Schwartz, and R. Hyers, "Electromagnetic levitation - a useful tool in microgravity research", *JOM*, **37**[5], pp. 50-53, (1995).
- [5] E. M. Schwartz, "Measurement of the surface tension of electromagnetically-levitated droplets in microgravity", MIT PhD thesis, p. 93, (1995).
- [6] G. P. Ivantsov, *Dohl. Akad. Nauk. SSSR*, **58**, pp. 567-569, (1947).
- [7] M. Azis, "Model for solute redistribution during rapid solidification", *J. Appl. Phys.*, **53**[2], pp. 1158-1168, (1982).
- [8] W. J. Boettinger, S. R. Coriell, and R. Trivedi, "Application of dendritic growth theory to the interpretation of rapid solidification microstructures", in Rapid Solidification Processing: Principles and Technologies IV, R. Mehrabian and P. A. Parrish, ed., Claitor's Pub. Div., Baton Rouge, LA, pp. 13-25, (1988).
- [9] D. Turnbull, "On the relation between crystallization rate and liquid structure", *J. Phys. Chem.*, **66**, pp. 609-613, (1962).
- [10] T. J. Piccone, "Solidification mechanisms in undercooled binary alloys", MIT PhD thesis, pp. 160, 199, (1990).
- [11] W. W. Mullins and R. F. Sekerka, "Stability of a planar interface during solidification of a dilute binary alloy", *J. App. Phys.*, **35**[2], pp. 444-451, (1964).
- [12] J. S. Langer and H. Muller-Krumbhaar, "Theory of dendritic growth I : Elements of a stability analysis", *Acta Metall.*, **26**, pp. 1681-1687, (1978).
- [13] J. Lipton, W. Kurz, and R. Trivedi, "Rapid dendrite growth in undercooled alloys", *Acta Metall.*, **35**[4], pp. 957-964, (1987).
- [14] J. Lipton, M. E. Glicksman, and W. Kurz, "Dendritic growth into undercooled alloy melts", *Mat. Sci. Eng.*, **65**, pp. 57-63, (1984).
- [15] W. J. Boettinger and S. Coriell, in Science and technology of the undercooled melt - rapid solidification materials and technologies, edited by P. R. Sahn, H. Jones, and C. M. Adam, Proc. of NATO ASI Series E Workshop No. 114, Castle of Theuren, FGR, pp. 81, (1985).

- [16] S. C. Huang and M. E. Glicksman, "Fundamentals of dendritic solidification - I : steady-state tip growth", *Acta Metall.*, **29**, pp. 701-715, (1981).
- [17] T. Iida and R. I. L. Guthrie, The Physical Properties of Liquid Metals, Oxford Science Publ., Oxford, UK, (1988).
- [18] V. Y. Zinov'yev, V. F. Plev, S. G. Taluts, G. P. Zinov'yeva, and S. A. Il'inykh, "Diffusivity and thermal conductivity of 3d-transition metals in solid and liquid states", *Phys. Met. Metall.*, **61**[6], pp. 85-92, (1986).
- [19] Y. Wu, T. J. Piccone, Y. Shiohara, and M. C. Flemings, "Dendritic growth of undercooled nickel-tin : Part I", *Met. Trans. A*, **18**, pp. 915-924, (1987).
- [20] J. Osugi, T. Arase, K. Hara, and F. Amita, "Diamond formation in molten nickel", *High Temperatures-High Pressures*, **16**, pp. 191-195, (1984).
- [21] K. Eckler, D. M. Herlach, R. G. Hamerton, and A. L. Greer, "Dendrite growth velocities in highly undercooled, dilute Ni-C melts", *Mat. Sci. Eng.*, **A133**, pp. 730-733, (1991).
- [22] J. L. Walker, in Principles of Solidification, edited by B. Chambers, Wiley, New York, NY, p. 114, (1964).
- [23] J. L. Walker, "The influence of large amounts of undercooling on the grain size of nickel", in Physical Chemistry of Process Metallurgy, part 2, edited by G. R. St. Pierre, Interscience Publishers, New York, NY, pp. 845-853, (1961).
- [24] T. J. Piccone, Y. Wu, Y. Shiohara, and M. C. Flemings, "Solidification of undercooled nickel and nickel-tin alloys", in Solidification Processing 1987, The Institute for Metals, London, UK, pp. 268-270, (1988).
- [25] E. Schleip, R. Willnecker, D. M. Herlach, and G. P. Görler, "Measurement of ultrarapid solidification rates in greatly undercooled bulk melts with a high speed photosensing device", *Mat. Sci. Eng.*, **98**, pp. 39-42, (1988).
- [26] B.T. Bassler, W. H. Hofmeister, G. Carro, and R. J. Bayuzick, "The velocity of solidification of highly undercooled nickel", *Met. Trans. A*, **25A**[6], pp. 1301-1308, (1994).
- [27] K. Ekler, M. Kratz, and I. Egry, "New technique of measuring dendrite growth velocities in undercooled metallic melts", *Rev. Sci. Instrum.*, **64**[9], pp. 2639-2642, (1993).
- [28] B. T. Bassler, W. H. Hofmeister, R. J. Bayuzick, R. Gorenflo, T. Bergman, and L. Stockum, "Observation of alloy solidification using high-speed video", *Rev. Sci. Instrum.*, **63**[6], pp. 3466-3471, (1992).
- [29] W. H. Hofmeister, "Solidification velocity studies of highly undercooled melts", invited talk at Advanced Materials and Technology for the 21st Century, JIM/TMS Fall meeting, 13-15 December, Honolulu, HA, (1995).

- [30] D. M. Matson, A. Shokuhfar, J. W. Lum, and M. C. Flemings, "Imaging the double recalescence behavior of Fe-Cr-Ni steel alloys", in Solidification Science and Processing, edited by I. Ohnaka and D. M. Stefanescu, TMS, Warrendale, PA, pp. 19-26, (1996).
- [31] J. Szekely, Fluid Flow Phenomena in Metals Processing, Academic Press, New York, NY, p. 175, 204, (1979).
- [32] J. W. Lum, D. M. Matson, and M. C. Flemings, "High speed imaging and analysis of the solidification of undercooled nickel melts", accepted for publication in *Met. Trans.*, October (1996).
- [33] G. B. McFadden and S. R. Coriell, "The effects of fluid flow due to crystal-melt density change on the growth of a parabolic isothermal dendrite", *J. Cryst. Growth*, **74**, pp. 507-512, (1986).
- [34] Zong, J., Szekely, J., and Schwartz, E., "An improved computational technique for calculating electromagnetic forces and power absorptions generated in spherical and deformed body in levitation melting devices", *IEEE Trans. on Mag.*, **28**[3], pp. 1833-1842, (1992).
- [35] Zong, J., Li, B., and Szekely, J., "The electrodynamic and hydrodynamic phenomena in magnetically-levitated molten droplets - I. Steady state behavior", *Acta Astronautica*, **26**[6], pp. 435-449, (1992).
- [36] R. Ananth and W. N. Gill, "Dendritic growth of an elliptical paraboloid with forced convection in the melt", *J. Fluid Mech.*, **208**, pp. 575-593, (1989).
- [37] R. Ananth and W. N. Gill, "Self-consistent theory of dendritic growth with convection", *J. Cryst. Growth*, **108**, pp. 173-189, (1991).
- [38] K. Koo, R. Ananth, and W. N. Gill, "Thermal convection, morphological stability and dendritic growth of crystals", *AIChE Journal*, **38**[6], pp. 945-954, (1992).
- [39] M. E. Glicksman, M. B. Koss, L. T. Bushnell, J. C. Lacombe, and E. A. Winsa, "Dendritic growth of succinonitrile in terrestrial and microgravity conditions as a test of theory", *ISIJ Int.*, **35**[6], pp. 604-610, (1995).
- [40] K. Eckler, and D. M. Herlach, "Measurements of dendritic growth velocities in undercooled pure Ni-melts - some new results", *Mat. Sci. Eng.*, **A178**, pp. 159-162, (1994).
- [41] G. A. Colligan and B. S. Bayles, "Dendrite growth velocity in undercooled nickel melts", *Acta Metall.*, **10**, pp. 895-897, (1962).
- [42] J. R. Taylor, An Introduction to Error Analysis, University Science Books, Mill Valley, CA, pp. 153-172, (1982).
- [43] R. Willnecker, D. M. Herlach, and B. Feuerbacher, "Evidence of nonequilibrium processes in rapid solidification of undercooled melts", *Phys. Rev. Letters*, **62**[23], pp. 2707-2710, (1989).

- [44] K. J. Bowman, "Materials concepts using Mathcad Part I : Euler angle rotations and stereographic projection", *JOM*, **47**[3], pp. 66-68, (1995).
- [45] R. W. Hyers, "Numerical and experimental modeling of the turbulent transition in a levitated liquid metal droplet", MIT PhD thesis, in progress (1996).
- [46] K. W. Smillie, An introduction to regression and correlation, Ryerson Press, New York, NY, pp. 22-26, (1966).
- [47] E. Brener, H. Müller-Krumbhaar, and D. Temkin, "Kinetic phase diagram and scaling relations for stationary diffusional growth", *Europhys. Lett.*, **17**[6], pp. 535-540, (1992).
- [48] A. Karma, personal communication (1996).
- [49] E. Ben-Jacob and P. Garik, "The formation of patterns in non-equilibrium growth", *Nature*, **343**, pp. 523-530, (1990).